EFFICIENT AND DURABLE AIR ELECTRODES FOR REVERSIBLE PROTONIC CERAMIC ELECTROCHEMICAL CELLS

CHEN XI

PhD

The Hong Kong Polytechnic University

2025

The Hong Kong Polytechnic University

Department of Building and Real Estate

Efficient And Durable Air Electrodes for Reversible Protonic Ceramic Electrochemical Cells

Chen Xi

A thesis submitted in partial fulfilment of the requirements for the degree of Doctor of Philosophy

May 2025

CERTIFICATE OF ORIGINALITY

I hereby declare that this thesis is my own work and that, to the best of my knowledge and belief, it reproduces no material previously published or written, nor material that has been accepted for the award of another degree or diploma, except where due acknowledgment has been made in the text.

(Signed)

CHEN Xi (Name of Student)

ABSTRACT

Reversible protonic ceramic electrochemical cells (R-PCECs) hold great potential as an energy conversion and storage device. However, its electrochemical performance at reduced operating temperatures is hindered by sluggish and unstable oxygen reduction/evolution reactions (ORR/OER) at conventional air electrodes. To overcome this limitation, this thesis identified multiple strategies integrating bulk anion substitution, surface nanoparticles design, and one-pot bulk-phase self-assembly to develop high-performance triple-conducting ($H^+/O^{2-}/e^-$) nanocomposite air electrodes with excellent stability.

First, anion engineering is applied to altering the oxygen sites of sublattice in $Ba_{0.5}Sr_{0.5}Co_{0.8}Fe_{0.2}O_{3-\delta}$ (BSCF). The results indicate that the electronegative fluorine substitution weakens metal-oxygen bonds and enhances proton uptake. Consequently, the optimized $Ba_{0.5}Sr_{0.5}Co_{0.8}Fe_{0.2}O_{2.9-\sigma}F_{0.1}$ air electrode demonstrates accelerated surface oxygen exchange and bulk H^+/O^{2-} transport, leading to a ~70% reduction in area-specific resistance compared to pristine BSCF.

Building on the first work's foundation, a dual bulk-surface modification strategy is successfully implemented through in situ growth of nanoscale catalysts on the surface of fluorine-engineered perovskite oxides. As a result, the $Ba(Co_{0.4}Fe_{0.4}Zr_{0.1}Y_{0.1})_{0.95}Ni_{0.05}F_{0.1}O_{2.9-\delta}$ nanocomposite air electrode exhibits a peak power density of 996 $mW \cdot cm^{-2}$ at 650 °C—60% higher than conventional electrodes—along with stable reversibility over 100 hours.

Moreover, to resolve persistent challenges in steam resistance and thermomechanical compatibly, a Co/Sr-free dual-phase perovskite oxide, $Ba(Zr_{0.1}Ce_{0.7}Y_{0.1}Yb_{0.1})_{0.4}Fe_{0.6}F_{0.1}O_{2.9-\delta}$ (BZCYYFF), is rational designed via one-pot self-assembly method. This design integrates a

proton-conductive Ce-rich phase (P-BZCYYFF) with triple-conducting Fe-rich domains (M-BZCYYFF), establishing continuous proton transport pathways while eliminating phase segregation risks. Additionally, fluorine anion doping further weakens metal-oxygen bonds in both phases, thus enhancing ionic mobility without catalytic compromise. The final BZCYYFF electrode achieves an ultra-low ASR of 0.33 $\Omega \cdot cm^2$ at 550 °C, coupled with a peak power density of 0.494 $W \cdot cm^{-2}$ in fuel cell mode and an exceptional electrolysis current density of 0.649 $A \cdot cm^{-2}$ (electrolysis voltage of 1.3 V) at 550 ℃. Long-term operation under 10% humidified air for over 160 hours and the 18 cycles spanning 180 hours demonstrates negligible degradation, further underscoring its unmatched durability.

In conclusion, by harmonizing triple conductivity, hydration resistance, and thermal compatibility, this work establishes a materials design paradigm for robust R-PCEC air electrodes, advancing their viability for energy storage and hydrogen economy applications.

PUBLICATIONS ARISING FROM THE THESIS

[1] **Chen, X.**, Y. Tan, Z. Li, T. Liu, Y. Song, S. Zhai, N. Yu, Z. Shao, M. Ni, Advanced Air Electrodes for Reversible Protonic Ceramic Electrochemical Cells: A Comprehensive Review. Advanced Materials. **2025**, 2418620.

[2] Yu, N., **Chen, X. (co-1st author)**, Liu, T., Zhai S., Yuan, J., Song Y., Ni M., Engineering Synergistic Oxygen-Proton Properties for High-Performance Reversible Protonic Ceramic Cell Air Electrodes, Small Science, **2025**, 2500256.

[3] **Chen, X**., Yu, N., Song, Y., Liu, T., Xu, H., Guan, D., ... & Ni, M. Synergistic Bulk and Surface Engineering for Expeditious and Durable Reversible Protonic Ceramic Electrochemical Cells Air Electrode. Advanced Materials, **2024**, 2403998.

[4] **Chen, X.**, Yu, N., Bello, I. T., Guan, D., Li, Z., Liu, T., ... & Ni, M. Facile anion engineering: A pathway to realizing enhanced triple conductivity in oxygen electrodes for reversible protonic ceramic electrochemical cells. Energy Storage Materials, **2023**, 63, 103056.

[5] **Chen, X.**, Yu, N., Bello, I. T., Zhang, D., Zhou, J., Wang, Y., ... & Liu, T. Understanding the oxygen reduction reaction in the hierarchically oriented composite cathode with open, straight pores. Separation and Purification Technology, **2023**, 325, 124713.

[6] **Chen, X.**, Wang, J., Yu, N., Wang, Y., Zhang, D., Ni, M., ... & Ding, M. A robust direct-propane solid oxide fuel cell with hierarchically oriented full ceramic anode consisting with in-situ exsolved metallic nano-catalysts. Journal of Membrane Science, **2023**, 677, 121637.

[7] Yu, N., Bello, I. T., **Chen, X**., Liu, T., Li, Z., Song, Y., & Ni, M. Rational Design of Ruddlesden–Popper Perovskite Ferrites as Air Electrode for Highly Active and Durable Reversible Protonic Ceramic Cells. Nano-Micro Letters, **2024**, 16(1), 177.

ACKNOWLEDGEMENTS

The completion of this PhD thesis could not be achieved without my hard work and great help from my supervisor and others. Here, I want to express my most sincere thanks and respect to everyone who has helped me.

First and foremost, I need to thank my supervisor, Prof. Meng Ni. From joining the research group as a research assistant to becoming a PhD student, Prof. Ni has given me careful guidance, which has had a significant positive impact on my research career. Throughout the whole research process, he spared no effort to help and guide me, including but not limited to actively discussing and analyzing various problems, proposing high-level ideas that suddenly enlightened me, and establishing close connections and promoting collaborations between our team and other high-level researchers. This significantly improved my research efficiency and confidence. After three years of professional study, with Prof. Ni's help, I believe my research level and academic vision have been greatly enhanced, laying a solid foundation for my future academic path. At the same time, Prof. Ni's humble personality, friendly attitude towards others, and scientific spirit of daring to face challenges and tackle hard problems have also benefited me deeply, making me more positive in facing challenges.

Then, I also want to thank the research group members of Prof. Ni and other researchers who have helped me. It is their help that made my research proceed smoothly. I thank them for their suggestions and corrections on my research topics during group meetings and conference presentations, which continuously improved my research capabilities. I also thank them for their meticulous help in my life and studies. Here, I especially thank Dr. Tong Liu for his funding support for my entire PhD thesis research.

Of course, I also want to thank the BRE staff for their full support in document acquisition, cleaning services, IT technology, sports activities, and safety education.

Additionally, I highly thank my family-my parents, sisters and brothers-in-law-for their life assistance and spiritual support. Whenever I encountered difficulties and anxieties, they always encouraged me and made me unafraid of failure. I thank my sisters and brothers-in-law for their warm hospitality, allowing me to enjoy family warmth and delicious food.

Finally, I want to especially thank my girlfriend, Dr. Na Yu, who is also a senior colleague. She has been my guiding force through the processes from Ph.D. application to degree completion. Specifically, she oriented me to both academic life at the university and cultural immersion in Hong Kong, facilitated my technical proficiency with laboratory instrumentation, and provided expert guidance in experimental design, data analysis, and misinterpretation correction. Thanks to her leadership and help, I could stand on the shoulders of giants to do more meaningful work.

The completion of this PhD thesis marks the end of my graduate studies and a new starting point in life. I hope to use the knowledge, skills, and experience gained during this PhD research career to maintain a continuous learning attitude and make greater contributions to the scientific community.

TABLE OF CONTENTS

LIST OF FIGURES

LIST OF ABBREVIATIONS

R-PCEC	Reversible protonic ceramic electrochemical cell
ORR	Oxygen reduction reaction
OER	Oxygen evolution reaction
ASR	Area specific resistance
BZCY	$BaZr_{0.7}Ce_{0.2}Y_{0.1}O_{3-\delta}$
BZCYYb	$BaZr_{0.1}Ce_{0.7}Y_{0.1}Yb_{0.1}O_{3-\delta}$
D_{chem}	Bulk diffusion coefficient
k_{chem}	Surface exchange coefficient
DFT	Density functional theory
DRT	Distribution of relaxation time
E_a	Activation energy
EC	Electrolysis cell
ECR	Electrical conductivity relaxation
EDTA	Ethylenediaminetetraacetic acid
EDX	Energy-dispersive X-ray spectroscopy
EIS	Electrochemical impedance spectrum
FC	Fuel cell
FT-IR	Fourier-transform infrared spectroscopy
HAADF-STEM	High-angle annular dark-field scanning transmission electron microscopy
MIEC	Mixed ionic and electronic conductor
BSCFF	$Ba_{0.5}Sr_{0.5}Co_{0.8}Fe_{0.2}O_{2.9-\Delta}F_{0.1}$
O_2-TPD	Oxygen temperature programming desorption
PCEC	Protonic ceramic electrolysis cell
PCFC	Protonic ceramic fuel cell
PPD	Peak power density
N-BCFZYNF	$Ba(Co_{0.4}Fe_{0.4}Zr_{0.1}Y_{0.1})_{0.95}Ni_{0.05}F_{0.1}O_{2.9-\delta}$
R_p	Polarization resistance
RP	Ruddlesden-Popper
SEM	Scanning electron microscope
R-SOC	Reversible solid oxide cells
SOEC	Solid oxide electrolysis cell
SOFC	Solid oxide fuel cell
TCO	$O^{2-}/H^{+}/e^{-}$ triple conductive oxide
TEC	Thermal expansion coefficient
TEM	Transmission electron microscopy
TG	Thermogravimetric analysis
F6	$Ba(Zr_{0.1}Ce_{0.7}Y_{0.1}Yb_{0.1})_{0.4}F_{0.6}F_{0.1}O_{2.9-\delta}$
XPS	X-ray photoelectron spectroscopy
XRD	X-ray diffraction

CHAPTER 1 Introduction

1.1 Background

With the rapid development of humanity, the issues of energy consumption and climate change have become increasingly prominent. The inherent non-renewability of fossil fuels, which constitute the primary energy sources, inevitably leads to energy crisis issues[1]. Furthermore, the utilization of these energy sources continually emits carbon dioxide into the atmosphere, exerting destructive impacts on the global climate and ecosystems[2]. To address these pressing challenges, countries worldwide have proposed a series of significant measures: China has set targets to achieve carbon peaking by 2035 and carbon neutrality by 2060 to achieve a balance between economic development and ecological sustainability[3]; the United Nations implemented the legally binding Paris Agreement in 2016, which requires 194 signatory countries and organizations to actively reduce carbon emissions[4]; the European Union announced the "RepowerEU" energy strategy to encourage energy savings and achieve energy supply diversification among EU member states[5]; in 2022, the U.S. Congress passed the “Inflation Reduction Act” to promote investment in renewable energy and accelerate the retirement of coal-fired power plants, aiming to achieve complete decarbonization of the power industry by 2035[6]. It is evident that reducing fossil energy consumption and carbon dioxide emissions to achieve sustainable development and carbon neutrality is increasingly crucial[7].

To accomplish this, reversible solid oxide cells (R-SOCs) technology has gained significant attention compared to other energy conversion and storage devices due to their low material costs, high electrochemical performance, exceptional conversion efficiency, and environmentally favorable properties. Specifically, when operating in electrolysis cell (EC)

mode, R-SOCs can convert surplus electricity generated by renewable sources into valuable chemicals, such as hydrogen. This presents two primary advantages: firstly, hydrogen energy's widespread application and low marginal cost over time make it highly promising for long-term, large-scale energy storage applications. Secondly, R-SOCs can be thermally integrated with downstream chemical syntheses, such as methanol, dimethyl ether, synthetic fuels, or ammonia production. Furthermore, when operating in fuel cell (FC) mode, R-SOCs can efficiently utilize stored chemical energy in fuels to produce electricity intensively and cleanly, without emitting exhaust fumes. This offers benefits including high energy conversion efficiency, fuel flexibility, environmental friendliness, and low material costs. More significantly, the reversible working mode in conjunction with other new energy devices can effectively mitigate the intermittency and variability issues associated with renewable energy electricity production. These outstanding characteristics render R-SOCs promising and attractive for sustainable energy utilization and achieving zero carbon emissions soon.

1.2 Advantages of R-PCECs

Currently, the conventional oxygen-ion conducting R-SOCs always operates at high temperatures (700-900 ^{o}C), which leads to increasing degradation and maintenance cost, intricating thermal management requirements and sluggish startup/shutdown. This limits its reliable large-scale and long-term applications. For this reason, utilizing proton-conducting materials instead of common oxygen-ion conductors to fabricate electrochemical cells is more promising since the lower activation energy required for protons conduction compared to oxygen-ions, ensuring the rapid ionic transport at reduced working temperatures[8]. Consequently, they can remain the high performance and efficiency at intermediate

temperatures (350 ºC-650 ºC), which relaxes the system design and control, enabling hybridization with a broader range of renewable energy and waste heat, and improving the cycling tolerance and reliability.

In this way, the reversible protonic ceramic fuel cells (R-PCECs) technology was proposed and has substantially increased interest in recent decades. Additionally, the R-PCECs can provide several unique advantages despite the lower operational temperature. Unlike the oxygen-conducting R-SOCs, they can utilize and produce pure and dry hydrogen directly, which results in enhancing fuel utilization and enabling electrochemical compression of hydrogen directly within the cell (without being diluted by vapor), thus reducing system complexity and operational costs.

Furthermore, based on the unique working mechanism of R-PCECs, utilizing its electrolysis mode (protonic ceramic electrolysis cell, PCEC) for synthesizing various high-quality chemicals such as ammonia, carbon monoxide, methane, low-carbon olefins, and aromatics has shown tremendous potential[9]. Currently, this electrochemical approach has been demonstrated to be economical, sustainable, and environmentally benign, as it efficiently harnesses renewable energy sources and abundant natural feedstocks such as nitrogen, water, and carbon dioxide. Moreover, the production of chemicals using PCECs paves an attractive pathway for large-scale chemical energy storage, enabling the stored chemical energy to be converted into electricity efficiently at any time, thus facilitating efficient energy conversion among different sources.

1.3 Fundamentals of R-PCECs

1.3.1 Working Mechanism

As previously mentioned, R-PCECs can seamlessly switch between two operational modes for reversible operation. Specifically, in FC mode, the device efficiently converts chemical energy from the fuel into electricity. As shown in **Figure 1.1**, taking H_2 as an example, it undergoes the hydrogen oxidation reaction (HOR) at the fuel electrode to produce protons (H^+), which then traverse the electrolyte membrane to reach the air electrode for oxygen reduction reaction (ORR), resulting in water as the final product. Conversely, in EC mode, the device can utilize electrical energy to produce high-quality chemicals. For instance, using H_2O as the electrolysis source, it is converted into oxygen and protons at the air electrode according to oxygen evolution reaction (OER). Then the generated protons pass through the electrolyte membrane to the fuel electrode side, where they undergo the hydrogen evolution reaction (HER) to produce dry and pure H_2. Detailed reactions are shown in **Equations 1.1-1.3**.

Fuel electrode (HOR/HER): $H_2(g) \rightleftharpoons 2H^+ + e^-$ (1.1)

Air electrode (ORR/OER): $\frac{1}{2}O_2(g) + 2H^+ + 2e^- \rightleftharpoons H_2O(g)$ (1.2)

Overall: $H_2(g) + \frac{1}{2}O_2(g) \rightleftharpoons H_2O(g)$ (1.3)

1.3.2 Functions and Requirements

In general, R-PCECs mainly consist of three key components in sandwich-like structures, as illustrated in **Figure 1.1**, which are the dense electrolyte layer sandwiched between the porous fuel electrode and air electrode on each side. Each component plays a crucial role during the operation modes.

The intermediate electrolyte layer primarily transports protons inside but isolates the

combustion reaction between fuel and air gases on both sides. Therefore, excellent proton conductivity and a pore-free structure are important indicators for the electrolyte layer. Additionally, the electrolyte layer must exhibit negligible electronic conductivity to prevent current leakage, which otherwise reduces fuel conversion efficiency and Faraday efficiency. Considering the relatively high ohmic resistance of electrolyte, fuel electrode-supported cells are generally adopted to achieve thin electrolyte film and reduce the overall ohmic resistance.

For the fuel electrode, it serves as the site for fuel oxidation/reduction, thus possessing excellent electrochemical catalytic activity for these reactions is crucial to deliver high performance. Furthermore, the electrochemical reactions conducted involve three phases which are electrons, protons, and gas. Therefore, the fuel electrode needs to have good electronic conductivity (e^- conductivity), the ability to generate protons and reduce protons (surface characteristics), proton transport capability (H^+ conductivity), as well as good gas diffusion capability (porous structure). Additionally, since the fuel electrode typically serves as the support layer of the whole cell, it also requires a certain level of sintering mechanical strength.

Like the fuel electrode, the air electrode also requires a porous structure and excellent electronic conductivity to facilitate the oxygen mass transport and electrons migration. However, the air electrode undergoes ORR/OER, thus good bifunctional catalytic activity for ORR/OER is essential to achieve high performance.

Meanwhile, to ensure excellent stability of R-PCECs, each component needs to maintain high thermal and chemical stability. Specifically, the fuel electrode needs to ensure stability in high temperature and reducing atmospheres, exhibit good carbon resistance when the feed gas

contains carbon fuels, and prevent the occurrence of sulfide poisoning. The air electrode should keep stable in oxidizing atmospheres and demonstrate certain resistance to CO_2 during long-term operation. The electrolyte layer also needs to ensure stability simultaneously in high-temperature oxidizing-reducing atmospheres. Furthermore, due to vaporized gaseous Cr species (e.g., CrO_3 and $CrO_2(OH)_2$) generated from the oxidation of chromium scale of the metallic interconnect in the stack system, the electrodes and electrolyte need to resistant these Cr species[10]. Additionally, the stability between components is also important, including the adapted thermal expansion coefficient to ensure a robust interface state, avoiding adverse thermal chemical and electrochemical reactions between components (e.g., phase separation, cation diffusion), and ensuring sufficient mechanical strength of the assembled cells.

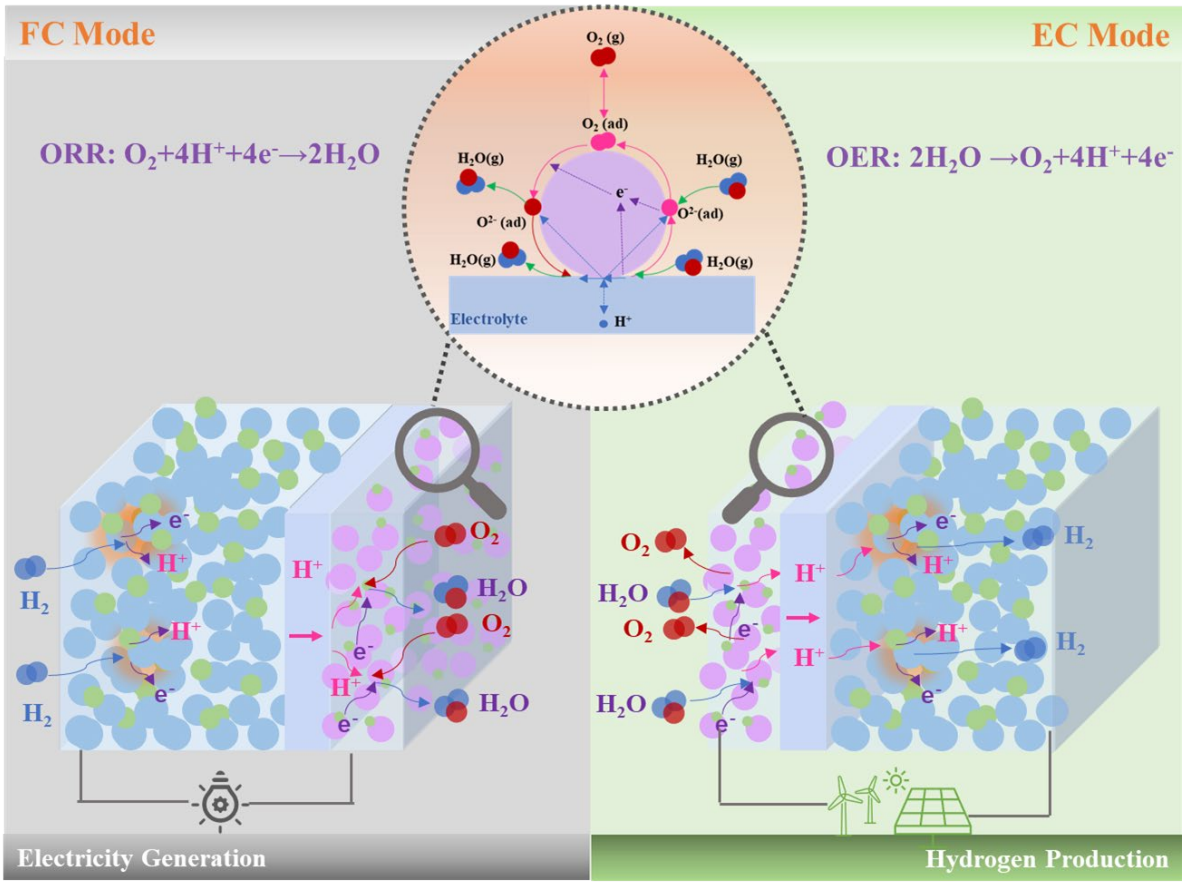

Figure 1.1 Schematic diagram of R-PCECs in fuel cell and electrolysis operation modes.

1.4 Research Objectives

To achieve stable and efficient energy conversion and storage in R-PCECs, the construction of air electrodes with high ORR/OER catalytic activity and stability is of paramount importance. Building on the fundamental physicochemical properties required, this research seeks to address the critical deficiencies inherent in current air electrode materials by employing simple yet effective strategies, which are proposed in this thesis.

Firstly, a practical approach of strategic anion engineering is proposed on the oxygen site of air electrode materials. By introducing different electronegative elements (F/Cl) to weaken metal-oxygen bonds (M-O), the oxygen chemical environment of the electrode material is altered, thereby promoting surface oxygen exchange and O^{2-}/H^{+} bulk migration. The resulting $Ba_{0.5}Sr_{0.5}Co_{0.8}Fe_{0.2}O_{2.9-\sigma}F_{0.1}$ electrode exhibits enhanced proton uptake/mobility and catalytic activity for ORR and OER, with improved stability.

In addition to the bulk triple-conducting capability, the surface of the electrode material is also of critical importance, as it serves as the active reaction site for gas conversion and product desorption during the electrode reactions. Therefore, building on the first research indicating that fluoride ions, due to their relatively large electronegativity, significantly weaken metal-oxygen bonds within the lattice, another strategy of simultaneous bulk and surface modification is identified to improve R-PCEC's electrochemical performance. Specifically, this strategy is designed to expedite the ORR/OER electrocatalytic activity of air electrodes exhibiting triple (O^{2-}, H^{+}, e^{-}) conductivity. In this way, the designed air electrode nanocomposite-$Ba(Co_{0.4}Fe_{0.4}Zr_{0.1}Y_{0.1})_{0.95}Ni_{0.05}F_{0.1}O_{2.9-\delta}$ demonstrates remarkable ORR/OER catalytic activity and exceptional durability in R-PCECs.

Moreover, achieving optimal electrochemical performance necessitates a well-defined interface between air electrode and electrolyte, which not only mitigates interfacial impedance but also ensures thermodynamic stability over extended operational durations and varying testing conditions. Meanwhile, the catalytic stability of materials under elevated vapor pressure conditions is also essential, as it substantially improves the electrolysis efficiency of R-PCEC in EC mode, thereby facilitating the production of a greater yield of green hydrogen. Therefore, by applying the strategy of integrating one-pot in situ bulk-phase self-assembly and anion engineering, another novel Co/Sr free air electrode bifunctional catalysts, $Ba(Zr_{0.1}Ce_{0.7}Y_{0.1}Yb_{0.1})_{0.4}Fe_{0.6}O_{2.9-\delta}F_{0.1}$, is well designed with reduced coefficients of thermal expansion, superior triple-conducting properties and enhanced resistance to steam.

By continuously optimizing multiple modification strategies, we have step by step synthesized a nearly ideal nanocomposite air electrode, thereby realizing a gradual and sustained improvement from electrocatalytic activity to long-term stability.

1.5 Outline of This Thesis

This thesis presents straightforward yet effective strategies for designing highly active and stable air electrodes for R-PCEC technology. It is structured into seven chapters, each addressing specific aspects of the research, as outlined below:

Chapter 1: Introduction. This chapter provides an overview of the background, advantages, and fundamental principles of R-PCECs, highlighting the significance of this technology in the context of sustainable energy solutions. It also delineates the research objectives, outlining the aims, scope, and innovative contributions of this thesis.

Chapter 2: Literature Review. This chapter comprehensively reviews the development of

air electrodes for R-PCECs, focusing on their underlying mechanisms, material compositions, and fabrication techniques. By categorizing materials based on their reaction mechanisms and ion migration pathways, coupled with various fabrication methods, this chapter critically analyzes the current state of R-PCEC technology and identifies key challenges associated with air electrodes.

Chapter 3: Methodology. This chapter details the experimental methods employed for the preparation and performance characterization of air electrodes and their integration into R-PCECs. It encompasses materials synthesis, cell fabrication, bar sample preparation, characterization techniques and electrochemical measurements, providing a robust foundation for the subsequent research chapters.

Chapter 4: Unlocking Triple Conductivity in Air Electrodes via Anion Engineering. This chapter explores the impact of anion engineering on the performance of air electrodes. Specifically, it demonstrates how tuning the M-O bonds in $Ba_{0.5}Sr_{0.5}Co_{0.8}Fe_{0.2}O_{3-\delta}$ (BSCF) perovskite oxides through the doping of electronegative anions (F^-, Cl^-), creating a more active oxygen chemical atmosphere, thereby enhancing its triple conductivity.

Chapter 5: Dual-Anion Engineering Coupled with In Situ Exsolution for Simultaneous Bulk and Surface Modification. Building on the findings of Chapter 4, this chapter introduces a dual modification strategy involving synergistic bulk and surface modifications. By simultaneously regulating bulk-phase M-O bonds and facilitating the in-situ formation of surface metal oxide (MO) nanocatalysts, a novel bifunctional air electrode material, $Ba(Co_{0.4}Fe_{0.4}Zr_{0.1}Y_{0.1})_{0.95}Ni_{0.05}F_{0.1}O_{2.9-\delta}$ (N-BCFZYNF), is synthesized. This material exhibits exceptional electrochemical performance in both FC and EC modes.

Chapter 6: Concomitant Activity-Stability Enhancement via Anionic Control and Multiphase Bulk Self-Assembly. This chapter focuses on the development of a series of nanocomposite materials by integrating one-pot in situ bulk-phase self-assembly and anion engineering to improve vapor tolerance and thermal compatibility. Additionally, the synergistic effects of attenuated M-O bonds through anion engineering and improved triple conductivity via bulk self-assembled dual nanophases structure are shown to significantly enhance the electrochemical performance and stability of these nanocomposite electrodes.

Chapter 7: Conclusions and Perspectives. The final chapter summarizes the key findings of the thesis, emphasizing the advancements made in the design and optimization of air electrodes for R-PCECs. It also proposes future research directions to address remaining challenges and further improve the performance and durability of R-PCEC air electrodes.

CHAPTER 2 Literature Review- Air Electrode

To elucidate the current challenges and progress of air electrodes used for R-PCECs, this literature review provides a comprehensive summary of recent studies. Overall, this chapter systematically elucidates the evolution of air electrodes through a rigorous examination of their theoretical foundations, material selection strategies, and advanced modification techniques. By integrating these dimensions, the discussion aims to uncover their potential applications and provide insightful projections for future research trajectories in this field.

2.1 Mechanism

2.1.1 Reactions Mechanism

The different ORR paths for the typical air electrodes with mixed O^{2-}/e^- conductivity (MIEC) and triple oxygen ion-proton-electron ($O^{2-}/H^+/e^-$) conductivity (TIEC) are summarized[11-13], as shown in **Figure 2.1**, and the following detailed elementary sub-steps displayed in **Equations 2.1-2.15**.

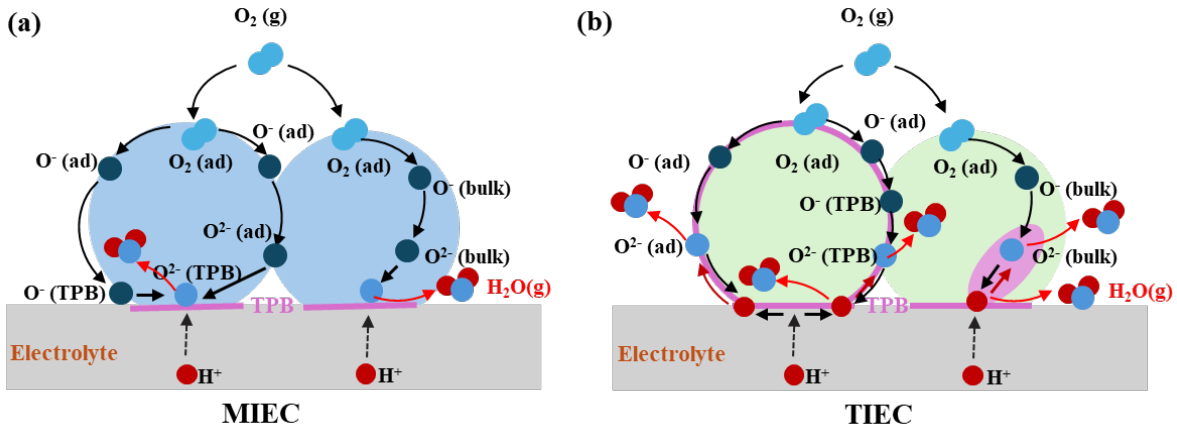

Figure 2.1 The detailed elementary ORR steps for (a) MIEC and (b) TIEC conductors applied as R-PCECs' air electrode.

Initial steps:

$O_2(g) \rightarrow O_{2,\,ad}$ (surface) (2.1)

$O_{2,\,ad}$ (surface) → $2O_{ad}$ (surface) (2.2)

Surface path (MIEC):

O_{ad}(surface) + e^-→ O^-_{ad} (surface) (2.3)

{ O^-_{ad} (surface) → O^-_{ad} (TPB), O^-_{ad} (TPB) + e^-→ O^{2-} (TPB) } (2.4)

{ O^-_{ad} (surface) + e^-→ O^{2-}_{ad}(surface), O^{2-}_{ad}(surface) → O^{2-} (TPB) } (2.5)

Bulk path (MIEC):

O_{ad}(surface) + e^-→ O^-_{ad} (bulk) (2.6)

O^-_{ad} (bulk) + e^-→ O^{2-}_{ad}(bulk) (2.7)

O^{2-}_{ad}(bulk) → O^{2-} (TPB) (2.8)

TPB (MIEC):

H^+ (TPB) + O^{2-} (TPB) → OH^- (TPB) (2.9)

Surface path-TPB (TIEC):

O_{ad}(surface) + e^-→ O^-_{ad} (surface) (2.3)

{ O^-_{ad} (surface) → O^-_{ad} (TPB), O^-_{ad} (TPB) + e^-→ O^{2-} (TPB), O^{2-} (TPB) + H^+ (surface) → OH^- (TPB) } (2.10)

{ O^-_{ad} (surface) + e^-→ O^{2-}_{ad}(surface), H^+ (surface) → H^+ (TPB), O^{2-}_{ad}(surface)+ H^+ (TPB) → OH^- (TPB) } (2.11)

Bulk path-TPB (TIEC):

O_{ad}(surface) + e^-→ O^-_{ad} (bulk) (2.6)

O^-_{ad} (bulk) + e^-→ O^{2-}_{ad}(bulk) (2.7)

H^+ (surface) → H^+ (bulk, TPB) (2.12)

O^{2-}_{ad}(bulk)+ H^+ (bulk, TPB) → OH^- (TPB) (2.13)

Final steps:

H^+ (TPB) + OH^- (TPB) → H_2O (TPB) (2.14)

H_2O (TPB) → H_2O (g) (2.15)

For MIEC-type air electrodes, the ORR processes primarily encompass oxygen adsorption and dissociation (**2.1, 2.2**), the subsequent generation and diffusion of active oxygen ions (**2.3-2.8**), and the concurrent generation of water at the TPBs coupled with surface dissociation (**2.9, 2.14, 2.15**). Similarly, the OER processes can be regarded as the reverse of these elementary sub-steps. These active oxygen ions, once generated, can traverse to the active reaction site via both surface (**2.3-2.5**) and bulk (**2.6-2.8**) transport pathways. As illustrated in **Figure 2.1a**, the TPBs are conspicuously confined to the interface between the air electrode and the electrolyte. Conversely, TIEC-type air electrodes introduce additional complexity to the electrochemical reaction due to their augmented proton transport capacity (**Figure 2.1b**). Specifically, the active oxygen ions possess the capability to selectively partake in electrode reactions with protons traversing the membrane, leading to the direct generation of water either at the electrode surface or within the bulk phase, followed by subsequent dissociation processes. Leveraging these expanded reaction sites, the TPBs of TIEC-type air electrodes extend across the entirety of the electrode surface and bulk phase, thereby significantly enhancing electrode ORR/OER kinetics. Accordingly, it is imperative to integrate proton conductivity into R-PCECs air electrodes in accordance with the elucidated reaction mechanism[14].

2.1.2 Proton Conduction Mechanism

As previously mentioned, the proton conductivity exhibited by TIEC air electrodes is pivotal in attaining elevated catalytic activity for ORR/OER. Hence, a thorough comprehension

of the proton conduction mechanism is imperative for the rational design of optimal air electrodes. Fundamentally, protons are incapable of occupying discrete sites within the crystal structure of perovskite oxides; instead, they tend to form bonds with other anions, primarily in the form of hydroxide defects ($OH^{\cdot}_{O}$)[15, 16]. Moreover, the high proton conductivity necessitates meticulous consideration of both the generation and migration of these hydroxide defects.

To date, three possible mechanisms for proton uptake in perovskite oxide at wet atmosphere have been proposed[17], as shown in in **Equations 2.16-18** and **Figure 2.2**.

(1) Hydration: $O_O^{\times} + V_{\ddot{O}} + H_2O \leftrightharpoons 2OH_O^{\cdot}$ (2.16)

(2) Hydrogenation: $H_2O + 2O_O^{\times} + 2h^{\cdot} \rightleftharpoons 2OH_O^{\cdot} + \frac{1}{2}O_2$ (2.17)

(3) New hydration: $Mn(III)_{Mn}^{\times} + V_{\ddot{O}} + O_O^{\cdot} + H_2O \leftrightharpoons Mn(IV)_{Mn}^{\cdot} + 2OH_O^{\cdot}$ (2.18)

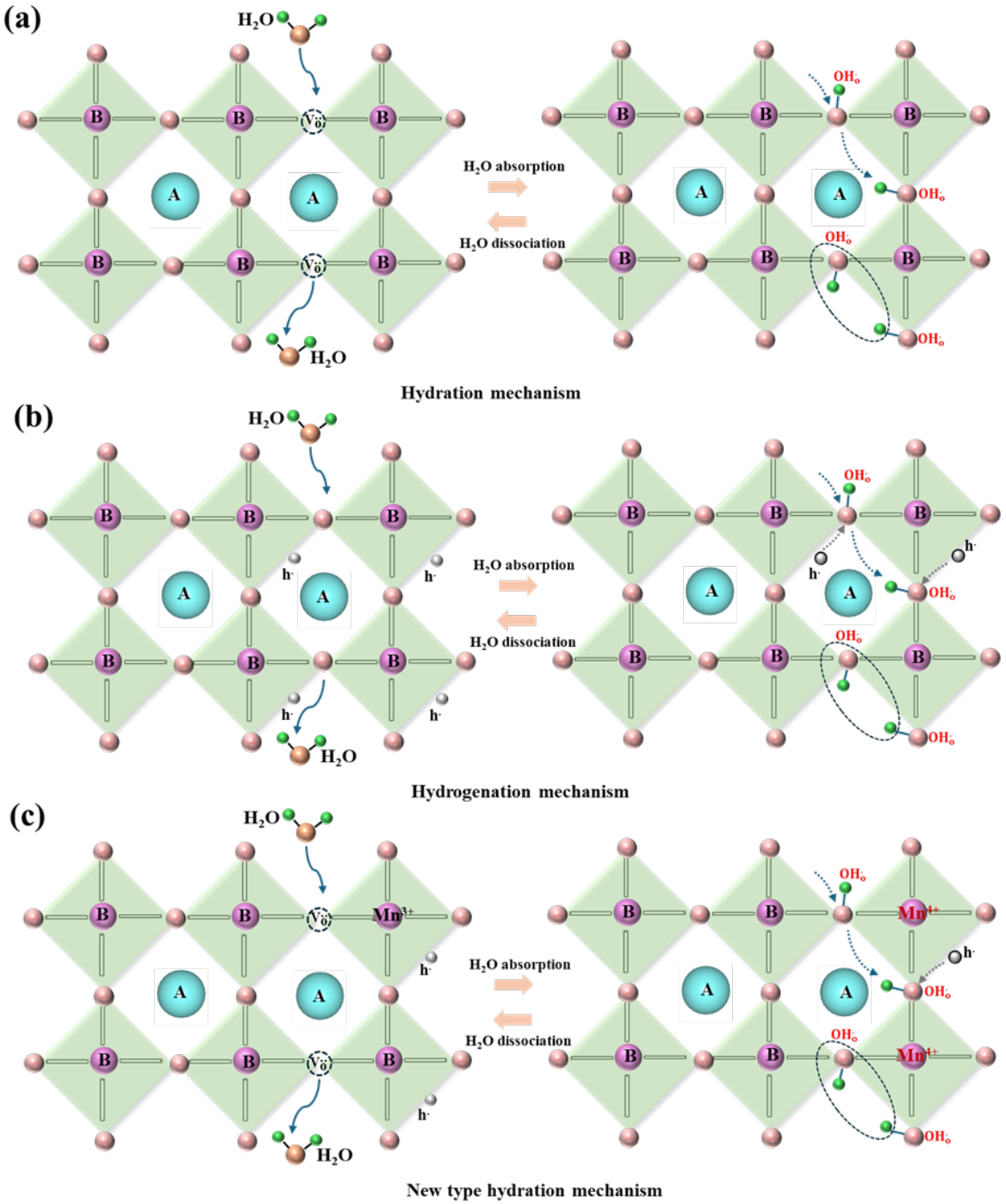

Figure 2.2 Three mechanisms for proton uptake[17]: (a) hydration mechanism; (b) hydrogenation mechanism; (c) new hydration mechanism.

The hydration reaction (**Equation 2.16** and **Figure 2.2a**) delineates the proton uptake process by which a water molecule decomposes into a proton (H^+) and a separate hydroxide ion (OH^-). Subsequently, the generated H^+ will combine with surrounded lattice oxygen ($O_O^\times$) to form the $OH^\cdot$ at the corresponding lattice oxide ion site, while the OH^- will occupy the

oxygen vacancy ($V_{\ddot{O}}$) site. This mechanism emphasizes the crucial role of lattice oxygen and oxygen vacancies in perovskite oxides in proton absorption. The rate of the hydration process, crucial for absorbing vapor from the surrounding environment, profoundly reflects the concentration of protons (expressed as C_H) incorporated into the material.

Another conceivable pathway for proton uptake, as described by **Equation 2.17** and depicted in **Figure 2.2b**, involves the hydrogeneration reaction. In this process, protons are assimilated while releasing oxygen through the interaction between two lattice oxygen atoms and steam, resulting in the depletion of holes within the oxides. This phenomenon is inherently favorable for perovskite oxide air electrodes possessing ample holes. Furthermore, this mechanism suggests that the concentration of lattice oxygen and holes may substantially influence the C_H within the material, whereas the concentration of oxygen vacancies may not play a significant role.

A recent proposal elucidated a third plausible pathway for proton uptake, which emerged from studies conducted on the air electrode material $La_{0.7}Sr_{0.3}MnO_{2.95}$ (LSM) oxide. As articulated by **Equation 2.18** and **Figure 2.2c**, this novel hydration reaction is propelled by the coupling of the attraction between $V_{\ddot{O}}$ and H_2O molecules, alongside carrier exchange involving oxygen holes ($O_O^{\cdot}$) and metal ions. Specifically, the OH^- produced from H_2O decomposition will occupy the $V_{\ddot{O}}$ site, thereby inducing the oxidation of adjacent Mn cations within the LSM oxide lattice. Simultaneously, the $O_O^{\cdot}$ site is substituted by the single H^+ to maintain electrical neutrality. This reaction presents heightened complexity due to the involvement of redox-active metal ions in conjunction with a substantial quantity of both $V_{\ddot{O}}$ and $O_O^{\cdot}$.

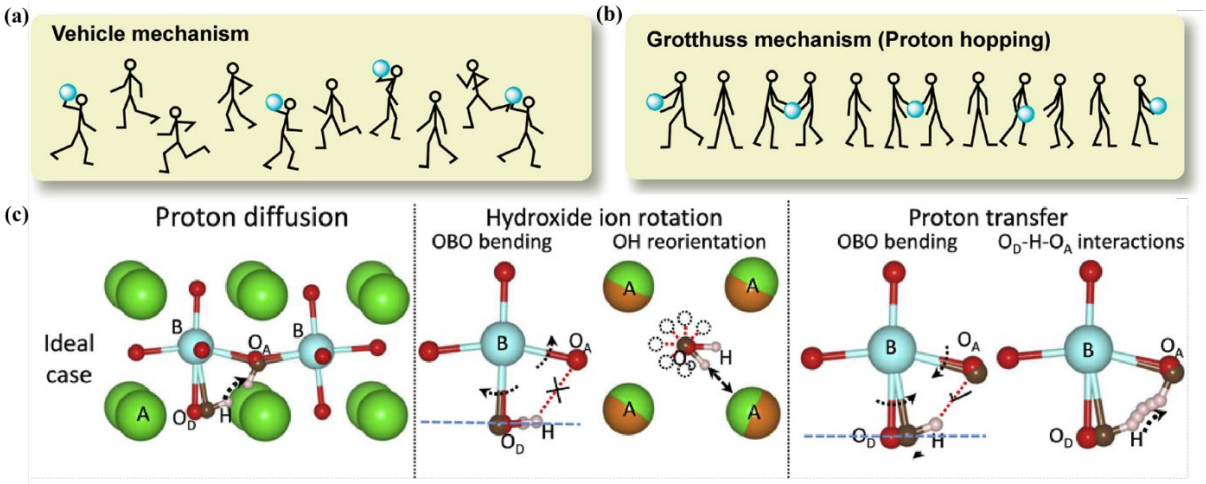

Figure 2.3 The mechanism for protons conduction: (a) Vehicle mechanism and (b) Grotthuss mechanism. Reproduced with permission[18]. Copyright (2008), American Chemical Society. (c) the sub-steps for Grotthuss mechanism. Reproduced with permission[19]. Copy right (2020), Elsevier.

In addition to proton generation, the mechanisms governing proton transport are also imperative. Currently, the ehicle and Grotthuss mechanisms, as proposed by Kreuer et al.[20], are widely accepted to describe the proton migration process. In the vehicle mechanism (**Figure 2.3a**), oxygen ions serve as carriers to facilitate proton transport by forming OH^- species within the perovskite oxide lattice. This mechanism implies that the migration rate of protons is contingent upon the diffusion rate of oxygen ion carriers. Consequently, proton conduction via this mechanism necessitates a relatively high activation energy (Ea, exceeding 0.4 eV) due to the limited mobility of carriers resulting from their larger size.

On the other hand, the Grotthuss mechanism (**Figure 2. 3b**) entails the migration of protons or proton defects from one oxygen ion to another through the formation and cleavage of O-H chemical bonds, resulting in a lower Ea value (< 0.4 eV). Thus, owing to the reduced energy required for proton conduction, the Grotthuss mechanism is generally favored in proton-conducting oxides. This mechanism entails two sub-steps for proton migration (**Figure 2.3c**) [19, 21]: (1) rotation, where the formed O-H bonds are oriented towards neighboring oxygen ions,

and (2) hopping, where the rotated O-H bond is broken, allowing the proton to hop from the parent site to another oxygen ion site via the presence of protonic defects. Numerous DFT studies have reported proton migration barriers, revealing that the reorientation of protons around the oxide ion to which they are bound typically exhibits a lower energy barrier than proton transfer to a neighboring oxide ion, both in perovskite electrolytes and electrode oxides. The calculated proton transfer barriers generally fall within the range of 0.25 to 0.5 eV[22-26].

2.1.3 Oxygen Conduction Mechanism

The remarkable oxygen ion transport capacity holds significant importance for air electrodes. Owing to the larger dimensions of oxygen ions, their transport barriers are inherently higher compared to those of protons. Thus, a profound comprehension of oxygen ion transport mechanisms is imperative to selectively optimize diffusion pathways, thereby macroscopically accelerating electrode reaction kinetics.

Presently, three widely acknowledged oxygen ion transport mechanisms exist for oxides, all determined by the nature of point defects within the systems: the interstitial, interstitialcy, and vacancy mechanisms. In the interstitial mechanism (**Figure 2.4a**), oxygen ions located at interstitial sites within the oxide lattice undergo thermal activation-induced jumps from one interstitial site to an adjacent one, thus facilitating oxygen ion migration. Consequently, the distance and pathway of interstitial ion jumps directly impact the rate of oxygen ion migration, without the necessity for other lattice defects to partake in this process. Additionally, upon completion of a single jump, there is no permanent displacement of other lattice ions from their equilibrium positions. Conversely, the interstitialcy mechanism (**Figure 2.4b**) posits that interstitial ions displace lattice ions from their equilibrium positions, prompting lattice ions to

jump to adjacent interstitial sites. Both mechanisms underscore the pivotal role of interstitial oxygen ions, which represent point defects in the lattice.

On the other hand, in the vacancy mechanism (**Figure 2.4c**), oxygen ions transport by jumping to a neighboring oxygen vacancy site within the lattice. Consequently, the existence of vacancies is imperative for oxygen diffusion, and their concentration within the lattice profoundly influences kinetics. Furthermore, it has been documented that oxygen ion transport adheres to the vacancy diffusion mechanism in single-structure perovskites due to the close structural arrangement of lattice sites, while oxygen interstitial diffusion mechanism occurs in certain layered perovskites with a Ruddleson–Popper (R-P) structure due to the surplus oxygen at the rock layer[27, 28].

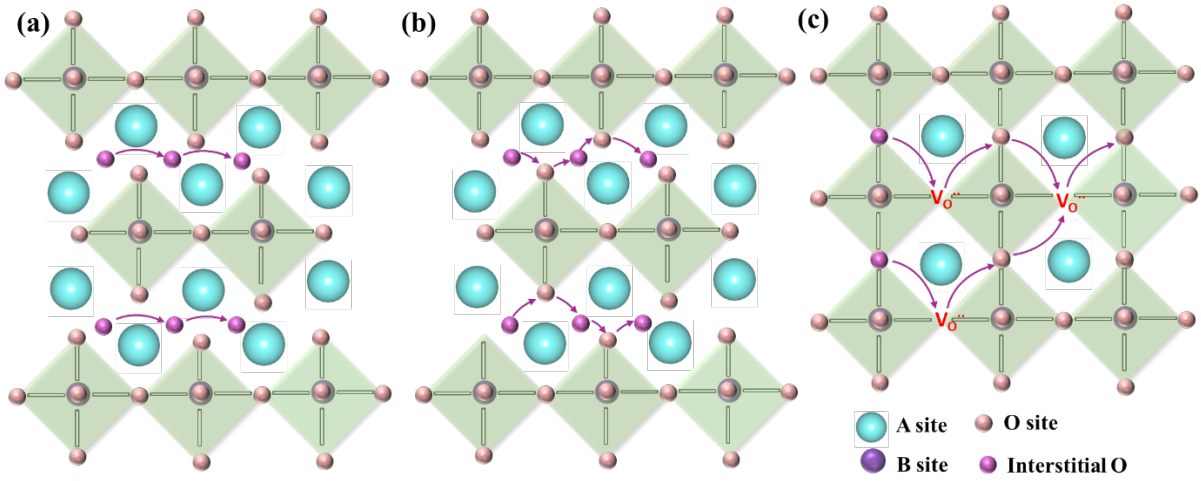

Figure 2.4 The Schematic diagrams of oxygen conduction mechanisms: (a) the interstitial and (b) interstitialcy in R-P perovskite; and (c) vacancy diffusion mechanism in single perovskite.

2.1.4 Electronic Conduction Mechanism

The electronic conductivity in perovskite oxide stems from the polaron hopping mechanism instigated by transition metal ions with variable valence anchored in the B-site. This mechanism entails electron defects traversing between B-site cations and oxygen ions, aligning with the Zerner double exchange process. Consequently, a heightened concentration

of redox couples (variable valence metal ions in the B-site) theoretically increased electrical conductivity, but it also depends on the specific lattice structure. For instance, the emergence of oxygen vacancies or heterointerfaces in multiphase may serve as electron traps, precipitating a decline in conductivity. The distinct conductivity profiles of various perovskite oxides can be dissected using band theory, which delineates the distribution of electronic states or the density of states (DOS), serving as pivotal descriptors for regulating diverse physical and chemical properties both at the surface and within the bulk. Presently, the conductivity range of most perovskite materials utilized in air electrode materials spans from 1 to 100 S cm^{-1} at temperatures ranging between 300 and 700 ºC, which notably surpasses that of protons and oxygen ions, particularly at lower temperatures.

2.2 Materials

2.2.1 Single Phase Air Electrode

The perovskite oxides have been widely used as promising air electrodes due to their outstanding catalytic activity, fine adjusted compositions and structure, and compatible thermal behavior. According to the composition of the specific perovskite oxide materials with high oxygen ion and electron conductivity (partly with proton conductivity), the phase structure includes three types: single ($ABO_{3-\sigma}$), double ($AA'BB'O_{6-\sigma}$) and R-P perovskite($A_{n+1}B_nO_{3n+1+\sigma}$), the detailed structures are shown in **Figure 2.5** and following part.

(1) $ABO_{3-\sigma}$: In the context of air electrode materials based on single perovskite structure, the A-site within their lattice typically accommodates alkaline earth or rare earth metal ions in a 12-fold coordination and a valence of either +2 or +3, exemplified by Ba, Sr, Pr, La, and Ca. Conversely, the B-site is commonly occupied by transition metal ions featuring a

coordination number of 6 and a valence of either +3 or +4, including Co, Fe, Ni, Zr, and Y. It is noteworthy that certain metal ions may exhibit higher valence states, such as Mo (+5 or +6), Nb (+5), and Ta (+4 and +5). Illustrated in **Figure 2.5a**, the schematic depiction of the unit cell structure portrays a simple cubic arrangement. Oxygen atoms reside in the face-centered positions of the cube, forming octahedral coordination with the B-site metal ions. This structural configuration exhibits pronounced symmetry, thereby facilitating expedited electron and ion transport within the bulk phase. Conversely, a reduction in the symmetry of the lattice structure, as observed in orthorhombic or tetragonal perovskite phases, engenders increased transmission distances, consequently impeding the efficient transmission of ions and electrons[13].

(2) $AA'BB'O_{6-\sigma}$: The general composition of double perovskite structure is alternately stacked layers along the c-axis direction in the form of …|AO|BO2|A'O|BO2|…, with its unit cell structure depicted in **Figure 2.5b**. Typically, the A-sites typically accommodate trivalent lanthanide metal ions such as Pr, Nd, Sm, and Gd, whereas the A'-sites commonly host divalent alkaline earth metal ions like Ba and Sr. Transition metal ions, like those found in simple perovskites, predominantly occupy the B-sites within the lattice. Notably, in ordered A-site double perovskite oxides, the larger ionic radius of A' ions tends to stabilize structures with a coordination number of 12, while A-site lanthanide ions (or Y ions) tend toward lower coordination numbers. Consequently, oxygen vacancies are primarily concentrated within the AO layers, and upon heating, a transition from ordered to disordered for oxygen vacancy occurs[29], thereby accelerating the rapid anisotropic migration of oxygen ions across the ab plane. Furthermore, recent investigations suggest

that the ordered arrangement of A-site cations in double perovskites can preserve higher concentrations of oxygen vacancies while enhancing their basicity[30], thereby positively impacting the hydration of protons in electrode reactions.

(3) $A_{n+1}B_nO_{3n+1+\sigma}$: For R-P-type perovskite oxides, it was first synthesized and named by S.N. Ruddlesden and P. Popper in 1957. Specifically, the types of metal ions occupying the A and B sites of this structure are like those in single perovskite-type oxides. It can be conceptualized as comprising alternating layers of perovskite structure layers (ABO_3) and rock salt layers (AO) along the c-axis with the general formula of it is $A_{n+1}B_nO_{3n+1-\sigma}$, where 'n' represents the number of octahedral layers in the perovskite-like stack. Notably, the simplest structure is $A_2BO_{4+\sigma}$, as depicted in **Figure 2.5c**, wherein the lattice is constructed using ABO_3 perovskite layers sandwiched between AO rock salt layers. Besides, the mixed ion-electron conductivity primarily mainly arises from the migration of interstitial oxygen ions in the AO layer and the p-type electronic conduction of the ABO_3 layer[31, 32]. Furthermore, higher-order R-P perovskites contain more NiO_6 corner-sharing octahedra, providing additional conduction pathways and potentially exhibiting higher electronic conductivity compared to low-order R-P materials[33].

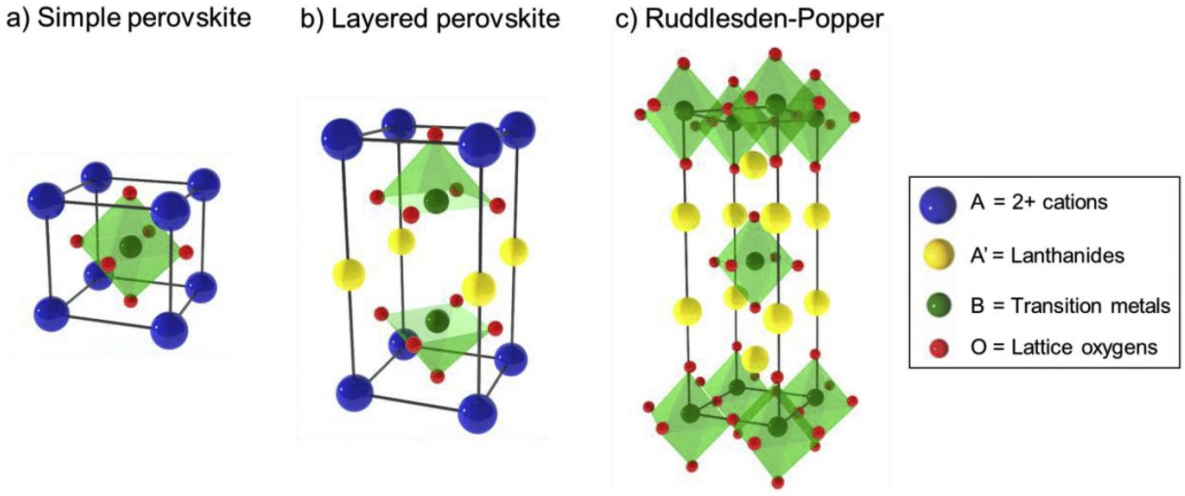

Figure 2.5 Typic perovskite oxides phase structures of air electrodes: (a) simple perovskite; (b) double perovskite; (c) Ruddlesden-popper perovskite. Reproduced with permission.[21] Copyright (2019), Elsevier.

2.2.2 Single Perovskite Phase

In the nascent development of R-PCECs technology, the traditional R-SOCs air electrode materials, including $La_{0.8}Sr_{0.2}CoO_{3-\delta}$ (LSC), $Sm_{0.5}Sr_{0.5}CoO_{3-\delta}$ (SSC), $La_{0.6}Sr_{0.4}Co_{0.2}Fe_{0.8}O_{3-\delta}$ (LSCF), and $Ba_{0.5}Sr_{0.5}Co_{0.8}Fe_{0.2}O_{3-\delta}$ (BSCF), were investigated as the initial air electrode candidates due to the commendable oxygen ion and electron conductivity characteristics. However, Han et al. confirmed that the systems of $La_{1-x}Sr_xCo_{1-y}Fe_yO_{3-\delta}$ (x = 0.1-0.7, y = 0-1) and $Ba_{0.5}Sr_{0.5}Co_{1-y}Fe_yO_{3-\delta}$ (y = 0.2-0.8) were difficult to be hydrated, and the C_H value was not higher than 0.002 mol unit^{-1} at 600 °C[34, 35]. This intrinsic limitation in proton conductivity hampers the kinetics of electrode reactions, thus resulting in suboptimal overall electrochemical performance of R-PCECs. Consequently, extensive endeavors have been directed towards augmenting the proton conductivity of the conventional air electrodes to foster hydration/protonation.

In 2014, Poetzsch et al. found that $Ba_{0.5}Sr_{0.5}Fe_{0.8}Zn_{0.2}O_{3-\delta}$ (BSFZ), which can be construed as a strategic substitution of Zn for Co within the BSCF material system, was a mixed triple-hole, O^{2-}, and H^+ conductor[36]. The hydration propensity of this electrode material was experimentally corroborated through characteristic mass relaxation signals observed upon reversible alterations in pH_2O levels within the testing environment maintained at 400 °C (**Figure 2.6a**). However, despite these advancements, under identical testing conditions, the concentration of protonic charge carriers remained notably lower by 1-2 orders of magnitude compared to the concentrations of oxygen vacancies and hole charge carriers, as depicted in **Figure 2.6b**. Subsequently, the augmentative effect of zinc ions on proton conductivity was

confirmed within the perovskite family (Ba,Sr,La)(Fe,Co,Zn,Y)$O_{3-\delta}$[37]. This enhancement primarily arises from the significant elevation of oxygen vacancy concentration, the presence of a redox-inactive cation, potential local lattice distortions, and the reduced electronegativity associated with Zn^{2+}. Conversely, the incorporation of Co ions at the B-site is observed to detrimentally influence proton absorption due to the diminished basicity of oxygen ions resulting from the strong covalent nature of Co-O chemical bonds, as shown in **Figure 2.6c**. Moreover, this study also suggests that A-site Ba ions are more conducive to proton absorption compared to other ions (Sr, La), owing to the lower electronegativity (**Figure 2.6d**). Ultimately, the $Ba_{0.95}La_{0.05}Fe_{0.8}Zn_{0.2}O_{3-\delta}$ material exhibits the highest proton concentration, measured at 0.1 mol $unit^{-1}$ at 250 °C.

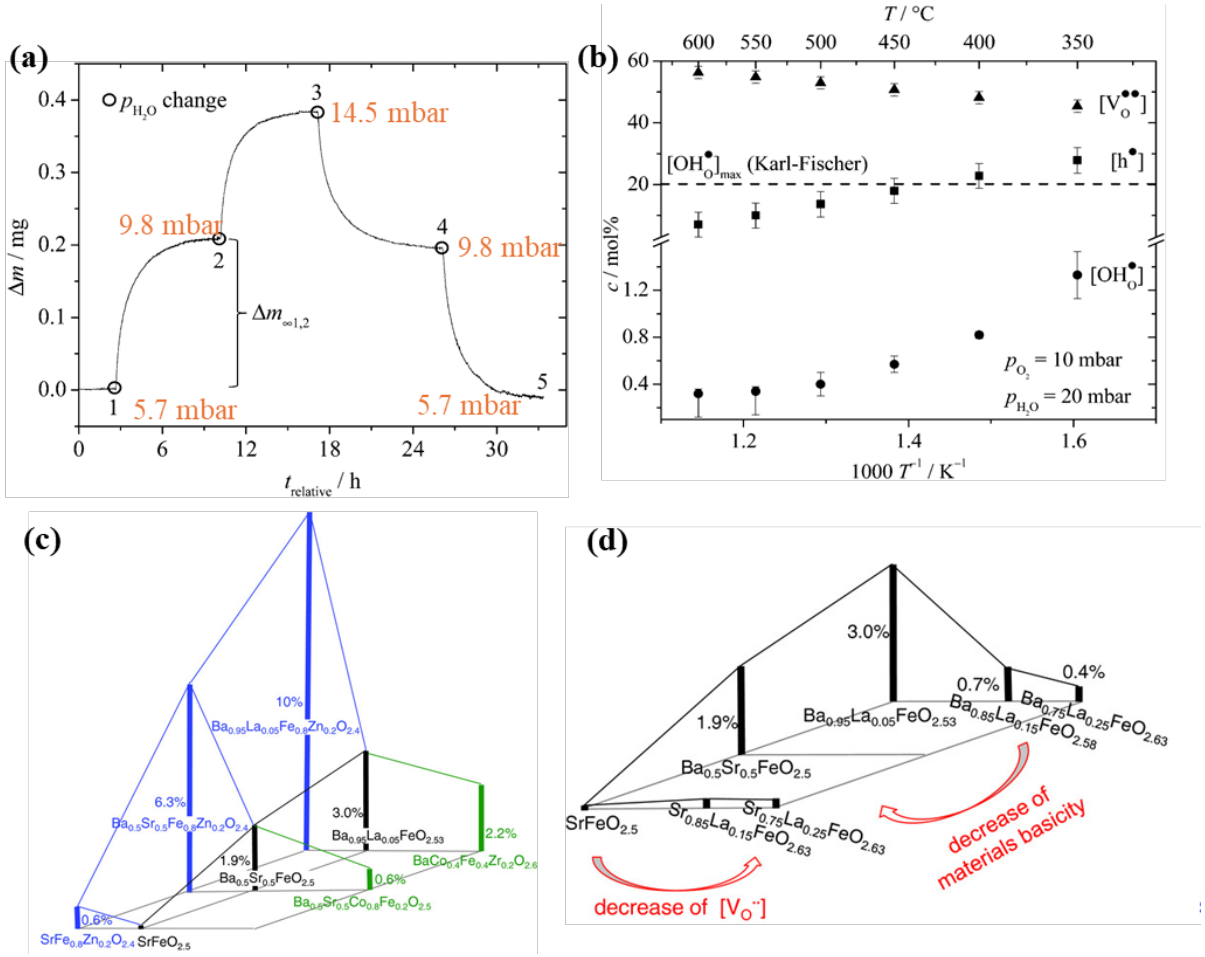

Figure 2.6 (a) Exemplary mass relaxation curves at 400 °C; (b) Defect concentrations (% per

BSFZ formula unit); Reproduced from Ref.[38] with permission from the Royal Chemical Society. (c) Effect of Zn and Co substitution on the B-site; (d) Variation of La and Sr content on the perovskite's A-site. Reproduced with permission.[37] Copyright (2018), Wiley.

Furthermore, Tong et al. discovered that Zr-doped $BaCo_{0.4}Fe_{0.6}O_{3-\delta}$ perovskite oxide ($BaCo_{0.4}Fe_{0.4}Zr_{0.2}O_{3-\delta}$, BCFZ) serve as highly stable and active oxygen permeation membranes due to their elevated mixed oxygen ion and electron conductivity, coupled with outstanding chemical and structural stability[39]. More importantly, this material exhibits stronger hydration capabilities compared to traditional LSCF, as evidenced by the reduced ASR values upon introducing water vapor[40]. Consequently, when directly employed as air electrodes in proton-conducting fuel cells, BCFZ yielded significantly enhanced electrochemical performance compared to traditional MIEC electrodes. Subsequently, aiming to further enhance its proton conductivity, considering the lower valence state of Y^{3+} compared to Zr^{4+}, Duan et al. partially substituted Y^{3+} for Zr^{4+} in BCFZ and designed a new class of air electrode, $BaCo_{0.4}Fe_{0.4}Zr_{0.2-x}Y_xO_{3-\delta}$ ($BCFZY_x$). Among the compositions investigated, $BaCo_{0.4}Fe_{0.4}Zr_{0.1}Y_{0.1}O_{3-\delta}$ (BCFZY) exhibited the lowest ASR values and activation energy when the temperature down to 500 ºC, as well as an exceptional durability over 1100 hours[41]. The 10% Y-doped BCFZY oxide exhibited the highest proton conductivity (0.0032 S cm at 600 ºC) approximately four times that of the parent material BCFZ, while further incorporation of Y slightly decreases its conductivity[42]. Furthermore, its proton surface kinetics were significantly accelerated, as evidenced by the $k_{OH\text{-}OD,chem}$ values obtained from a conductivity relaxation experiment by switching atmospheric conditions from H_2O to D_2O. Since then, BCFZY is regarded as a representative single perovskite phase air electrode with triple conductivity capabilities, and extensive research based on it has been conducted.

To further fine-tune the triple-conducting properties, an A-site deficiency strategy was

employed to fabricate new perovskite oxides, $Ba_xCo_{0.4}Fe_{0.4}Zr_{0.1}Y_{0.1}O_{3-\delta}$ (x = 1, 0.95, 0.9)[43]. As a result of the higher concentration of oxygen vacancies and the enhanced oxygen-ion bulk diffusion and proton hydration kinetics, obtained $Ba_{0.9}Co_{0.4}Fe_{0.4}Zr_{0.1}Y_{0.1}O_{3-\delta}$ exhibited the lowest ASR value (0.52 Ω cm^2) at 500°C. Furthermore, Shao et al. employed B-site doping to enhance the triple conductivity performance of BCFZY, synthesizing a series of air electrode materials, $Ba(Co_{0.4}Fe_{0.4}Zr_{0.1}Y_{0.1})_{0.95}M_{0.05}O_{3-\delta}$ (M = Ni, Mn, Zn, Cu)[44]. Based on conductivity relaxation experiments and oxygen and hydrogen permeation tests, it was demonstrated that Ni-doped BCFZY ($Ba(Co_{0.4}Fe_{0.4}Zr_{0.1}Y_{0.1})_{0.95}Ni_{0.05}O_{3-\delta}$) air electrodes exhibited enhanced oxygen ion and proton transport characteristics and surface exchange kinetics, thereby displaying enhanced ORR activity, with the ASR value decreased from 1.75 to 1.50 Ω cm^2 at 550 °C. Additionally, partial doping of the BCFZY parent lattice with lower valence state Mg^{2+} ($Ba(Co_{0.4}Fe_{0.4}Zr_{0.1}Y_{0.1})_{0.95}Mg_{0.05}\ O_{3-\delta}$) and Zn^{2+} ($BaCo_{0.4}Fe_{0.4}Zr_{0.1}Y_{0.1-x}Zn_xO_{3-\delta}$) were also demonstrated effectively to improve its triple conductivity characteristics[45, 46]. Interestingly, despite the lower electron conductivity of BCFZY and its modified samples, which varies from 1 to 2 S cm^{-1} at 600 °C, their electrochemical performance remains stratified. This implies that air electrodes may do not necessarily require a very high hole conductivity, but rather, achieving a balance between ion and hole conductivity and catalytic activity is more meaningful.

2.2.3 Double Perovskite Phase

The cation-ordered double-perovskite structures have garnered significant attention owing to their facilitated oxygen ion diffusion, accelerated surface oxygen exchange, and heightened electrical conductivity at lower temperatures[47]. Additionally, as indicated by Grimaud et al.[48],

these layered perovskite materials demonstrate improved proton-conducting properties to some extent. Therefore, layered perovskites are considered promising candidate materials for air electrodes in R-PCECs.

Currently, the most commonly used double-perovskite phase for R-PCECs is $PrBa_{0.5}Sr_{0.5}Co_{1.5}Fe_{0.5}O_{5+\delta}$ (PBSCF), originating from $NdBa_{0.5}Sr_{0.5}Co_{1.5}Fe_{0.5}O_{5+\delta}$ (NdBCSF) oxide reported by Kim in 2014[49]. The PBSCF air electrode was developed as an air electrode since the Pr analog offers higher electronic conductivity than Nd in the layer perovskite structure[29]. Moreover, PBSCF exhibited excellent ORR/OER catalytic performance when it was exposed to steam atmosphere. As shown in **Figure 2.7a** [50], the C_H values determined by the difference H_2O uptake thermogravimetric profiles on cooling in dry and wet air ranges from 3.5 mol % at 200 °C to 1.7 mol % at 600 °C, which is much higher than that of BCFZ (0.5 mol% at 400 ºC) and BCFZn (1.5 mol% at 350 ºC). The higher proton concentration observed in PBSCF can be ascribed to its lower hydration entropy of -63 J mol^{-1} K^{-1} compared to -103 ± 5 J mol^{-1} K^{-1} in BCFZ and -140 ± 30 J mol^{-1} K^{-1}, respectively (**Figure 2.7b**), enabling PBSCF to maintain elevated proton levels under high-temperature conditions. Specifically, the proton solubility for the PBSCF was directly observed through dynamic secondary ion mass spectrometry and time-of-flight secondary ion mass spectrometry[51]. The depth profile (~3.5 μm) and 3D map (50 × 50 × 1 μm3) of ^2D element for PBSCF bulk in D_2O-humidified air confirmed that the protons were spatially uniform distributed without any segregating in a specific region (**Figure 2.7c**) [51]. From the returned relativity precise values of α determined by the conductivity change, it is confirmed that the proton uptake in PBSCF mostly occurred by the hydration reaction at 400–700 ºC. Despite the proton uptake mechanism, the migration

kinetics of these protonic defects during hydration/dehydration is also investigated by employing the isotope exchange diffusion profile (IEDP) method, in which deuterium was used as a tracking indicator of proton diffusion via time-of-flight secondary ion mass spectrometry (ToF-SIMS), as shown in **Figure 2.7d**[52]. The surface exchange coefficient (k^*_H) and diffusion coefficient (D^*_H) of protons were determined in the value of 2.60×10^{-7} cm s^{-1} and 1.04×10^{-6} cm^2 s^{-1} at 550 ºC, respectively, which much higher than most reported air electrodes (**Figure 2.7e**). These results robust confirmed the excellent triple-conducting prosperities of PBSCF family materials, which offers a great promising candidate to applied as the air electrode for R-PCECs device. Surely, it is more beneficial for its actual application if the high TEC was reduced and the undesired elements segregation and heterophane generation conducted in CO_2 or H_2O containing atmosphere.

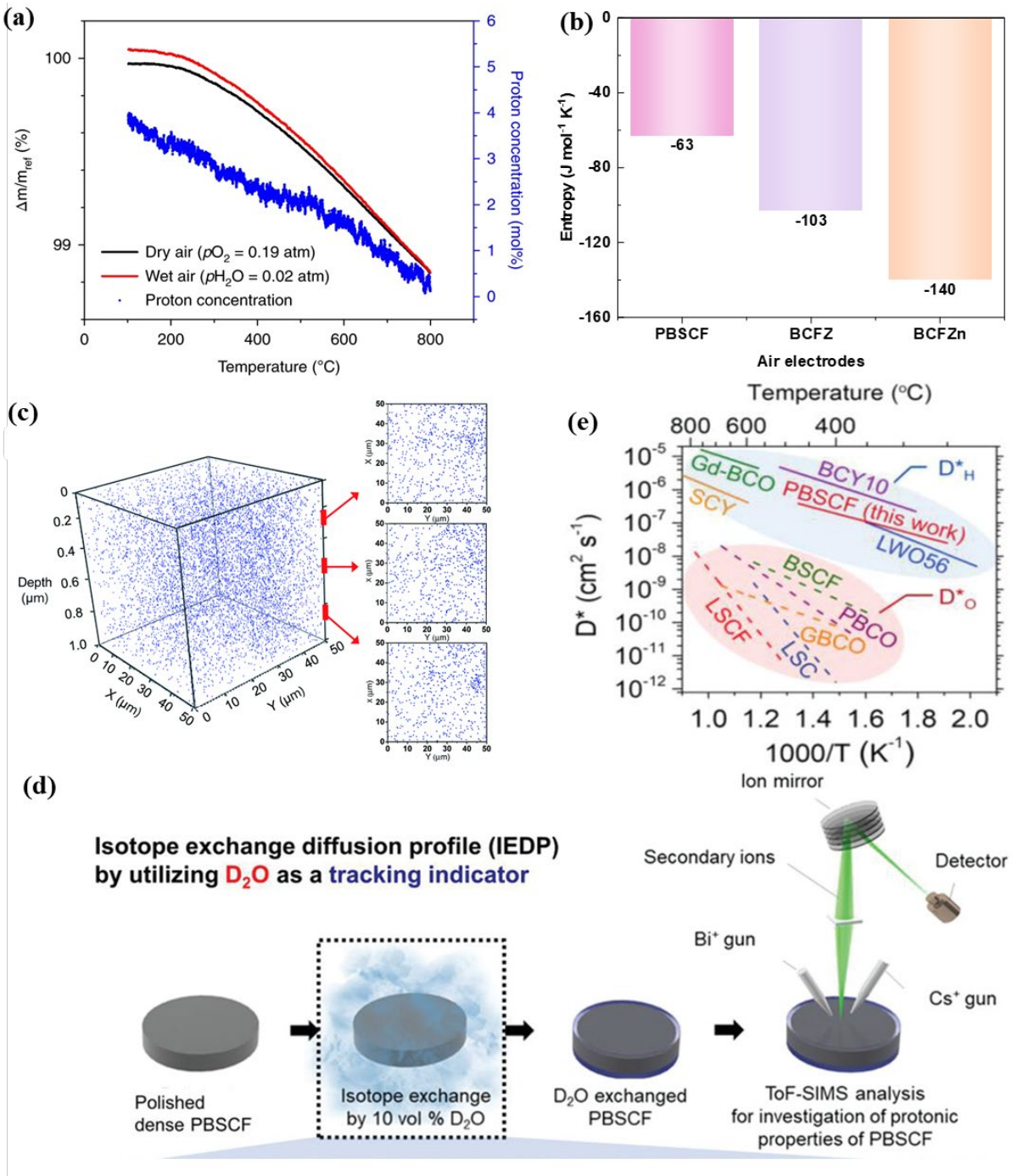

Figure 2.7 (a) thermogravimetric profiles on cooling in dry and wet air and implied proton concentration; (b) summarized entropy values for different air electrodes; Reproduced with permission.[50] Copyright (2018), Springer Nature. (c) 3D map of ^{2}D distribution; Reproduced from Ref.[51] with permission from the Royal Chemical Society. (d) Schematic illustration of preparation and incorporation of D_2O for the ToF-SIMS measurement; (e) Comparison of D^*_H of the PBSCF with other representative MIEC materials. Reproduced with permission.[52] Copyright (2021), Wiley.

2.2.4 R-P Perovskite Phase

The perovskite and rock-salt slab arrangement in R-P oxides facilitates anisotropic

transport of charge carriers, including O^{2-} and proton defects[53-56], which different from the migration mechanism observed in conventional perovskite oxides, wherein oxide ions traverse pathways connect oxygen vacancies. In R-P perovskite oxides, particularly those featuring an excess of oxygen (as commonly encountered in the n=1 referred as K_2NiF_4 structure), interstitial oxide ions are accommodated within the rock-salt layers[31, 33]. This arrangement facilitates rapid and anisotropic conduction of oxide ions through a push-pull mechanism within the rock-salt layers, holding the potential to accelerate kinetically limited ORR/OER electrochemical processes, particularly at lower operating temperatures. Consequently, R-P type perovskite oxides emerge as highly promising candidates for application as air electrodes in R-PCECs.

Initially, the excellent hydration and protonic defects transports ability were demonstrated in the $Pr_{2-x}Sr_xNiO_{4+\delta}$ ($x \leq 0.50$) oxides with the K_2NiF_4 structure (**Figure 2. 8a-b**)[57]. Considering the potential detrimental effects of Sr^{2+} incorporation on hydratable characteristics and the overall stability of the material, $Pr_2NiO_{4+\delta}$ has been selected for actual utilization, showcasing commendable chemical stability and outstanding electrochemical performance(0.06 $\Omega \cdot cm^2$ and 0.82 $W \cdot cm^{-2}$ at 650°C) [58]. Furthermore, in the $Ln_{1.2}Sr_{0.8}NiO_{4+\delta}$ (Ln = La, Pr) system, different A-site cations also exert an influence on the catalytic activity of the air electrode reaction. Specifically, compared to $Pr_{1.2}Sr_{0.8}NiO_{4+\delta}$, $La_{1.2}Sr_{0.8}NiO_{4+\delta}$ exhibits higher electrochemical performance in both FC and EC modes[59]. This disparity is likely attributed to the lower electronegativity of La^{3+} compared to Pr^{3+} and the different oxygen chemical environment due to the different for La bad Pr-based R-P oxides, which may adversely affect proton/oxygen absorption and transport capabilities[58]. Besides, the

introduction of Fe ions into the B-site of this oxide can further enhance its catalytic performance, as evidenced by $La_{1.2}Sr_{0.8}Ni_{0.6}Fe_{0.4}O_{4+\delta}$[60].

Furthermore, the layered architecture inherent to R-P type oxides imparts unique cation coordination environments and distinct manifestations of anion defects[61, 62]. Modulating the number of layers, denoted as 'n', imparts changes to the dimensional characteristics of the layered structure, thereby expanding the chemical diversity within the realm of R-P perovskites. Consequently, variations in stoichiometry are observed; for instance, low n-value R-P oxides tend to exhibit a prevalence of interstitial oxygen over oxygen vacancies, while high-order R-P oxides typically manifest oxygen-deficient configurations. Experimental investigations and theoretical analyses corroborate the notion that higher-order R-P oxides exhibit enhanced facilitation of oxygen ion and proton transport within the lattice structure[63]. Moreover, they demonstrate heightened chemical and thermal stability, attributes conducive to augmenting catalytic performance of air electrodes[63-65].

A novel double-layer R-P oxides with the composition of $Pr_2BaNiMnO_{7-\delta}$ (PBNM) was reported as a preeminent highly active low-temperature air electrode[64]. In the selected $Pr_3Ni_2O_7$ system, simultaneous introduction of Ba^{2+} into the A-site and Mn^{3+}/Mn^{4+} into the B-site serves to augment both stability and catalytic performance. Moreover, significant water intercalation, alongside potential proton defects, has also been identified in the double-layered R-P oxide $Sr_3Fe_2O_{7-\delta}$ (R-P-SF), resulting in the formation of hydrated derivatives under humid conditions[66]. In response, Lu et al. pioneered its utilization as an air electrode, substantiating its proficiency as an effective oxygen ion-electronic conductor in dry atmospheres through EIS results. Furthermore, employing first-principal calculations based on DFT methods, R-P-SF

was found to possess a low proton formation energy (~-0.23 eV) and a low proton migration energy (~0.62 eV) in humid atmospheres[67]. However, R-P-SF exhibits chemical instability in atmospheres involving Lewis acids (steam/CO_2) due to the high basicity of Sr. Consequently, the introduction of the lanthanide element Eu in partial replacement of Sr in the A-site of R-P-SFO was proposed to mitigate this basicity at the cost of oxygen vacancies. To address this vacancy, Co was partially substituted for Fe, yielding $SrEu_2Fe_{1.8}Co_{0.2}O_{7-\delta}$ (SEFC), as illustrated in **Figure 2. 8c-d**[68]. By employing the SEFC air electrode, the R-PCEC button demonstrated smooth transitioning between FC and EC modes without no discernible degradation over a 135-hour long-term test.

Recently, Ni et al. devised a method involving the concurrent introduction of A-site deficiency and partial Nb-substitution to synthesize $Sr_{2.8}Fe_{1.8}Nb_{0.2}O_{7-\delta}$ (D-SFN)[69]. This approach effectively restrained the formation of the secondary phase $Sr_3Fe_2(OH)_{12}$, thus stabilizing the lattice structure. Additionally, partial Sr defects were intentionally introduced to elevate the concentration of oxygen vacancies. The resulting D-SFN air electrode exhibited markedly heightened electrocatalytic activity and stability (Figure 2. 8e), demonstrating remarkable resilience under both FC and EC modes, including their switching mode. Moreover, three-layered RP oxides also serve as promising candidates for R-PCEC air electrodes. For instance, a novel single-phase air electrode, $Sr_3EuFe_{3-x}Co_xO_{10-\delta}$ (3-SEFCx, x = 0.0, 0.5, 1.0, 1.5), was synthesized through a co-doping approach involving Eu and Co (similar to the SEFC air electrode)[70]. This electrode demonstrated elevated oxygen non-stoichiometry and favorable structural thermal stability.

The tunability afforded by the composition and structure of R-P perovskites engenders

unique electronic configurations and an array of captivating physicochemical properties unattainable by traditional perovskite compounds or many other crystalline metal compounds. Thus, this presents promising avenues for the strategic design of electrocatalysts based on the distinct chemical, structural, and electronic attributes inherent to R-P perovskites.

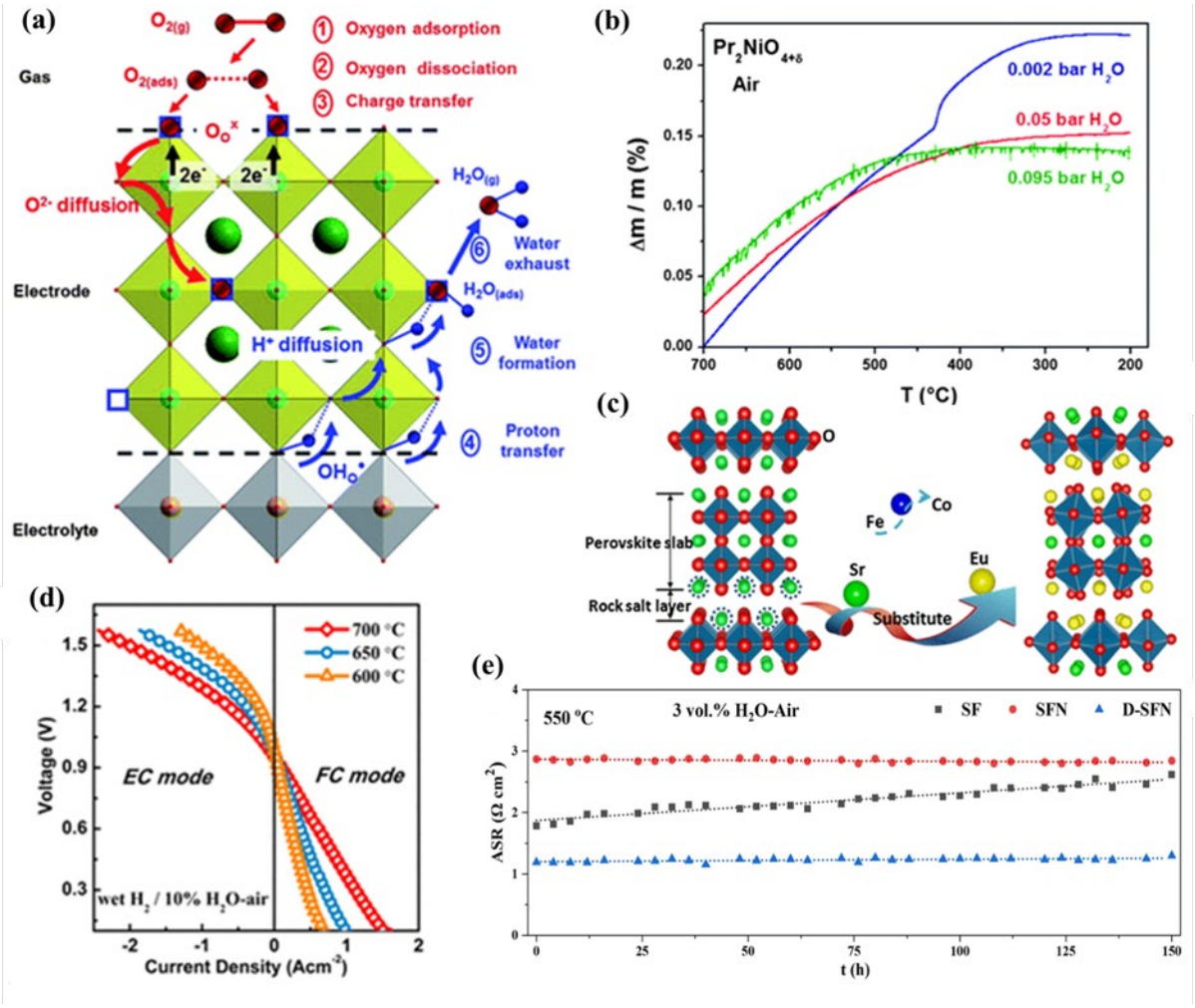

Figure 2.8 (a) Schematic representation of the oxygen reduction and formation of water for TCO; (b) weight change measured at decreasing temperature for $Pr_2NiO_{4+\delta}$ under air containing 0.002 up to 0.095 bar H_2O; Reproduced from Ref.[57] with permission from the Royal Chemical Society. (c) the design sketch from R-P-SF to SEFC; (d) the performance for SEFC air electrode; Reproduced with permission.[68] Copyright (2018) American Chemical Society. (e) the ASR values for SF, SFN and D-SFN air electrodes. Reproduced with permission.[69] Copyright (2024), Springer Nature.

2.3 Modification Strategies

Due to the challenges posed by homogeneous oxides, achieving a balance in triple-

conducting, stability, and catalytical performance can be difficult. For instance, most high-performance MIECs often exhibit proton blocking and limited proton absorption and transport capabilities, some excellent proton conductor electrolyte phases may lack sufficient electronic/oxygen ion transport capabilities, and some triple conducting oxides exhibit unsatisfied catalytical activity. Consequently, there is a need to fabricate composite electrodes with coexisting phases possessing different functionalities to simultaneously achieve optimized properties.

2.3.1 Mechanical Mixing

Mechanical mixing is a physical treatment technique that is commonly employed for composite electrodes due to its cost-effectiveness and simplicity. This method involves minimal alteration to the sample composition while allowing for particle size reduction to the nanoscale (**Figure 2.9a**). This reduction is achieved by controlling parameters such as milling speed, dwell time, ball-to-powder ratio, and milling media, ensuring thorough grinding of bulk samples.

In the early stage, the composite air electrode was commonly fabricated by mixing a MIEC and a protonic conductor via mechanical milling since the limited proton conductivity. One of the earlies electrodes reported was $Sm_{0.5}Sr_{0.5}CoO_{3-\delta}$ (SSC) mixed with a proton conductor of $BaCe_{0.8}Sm_{0.2}O_{3-\delta}$ (BCS20)[71]. The highest performance was achieved when the content of SSC reached approximately 60 wt%. In addition, SSC was also used to mix with some other proton-conducting phases, such as $BaCe_{0.5}Zr_{0.3}Y_{0.16}Zn_{0.04}O_{3-\delta}$[72], $BaZr_{0.8}Y_{0.2}O_{3-\delta}$ (BZY20)[73] and $Ba(Zr_{0.1}Ce_{0.7}Y_{0.2})O_{3-\delta}$[74]. Similar trend was observed in $Ca_{0.3}Y_{0.7}Fe_{0.5}Co_{0.5}O_{3-\delta}$-$BaZr_{0.1}Ce_{0.7}Y_{0.2}O_3$ (CFYC-BZCY)[75] composite air electrode (**Figure 2.9b, c**). The

electrochemical performance varies from 277 to 445 mW cm^{-2} at 600 °C due to the different proton conductors and mixing ratio. As another classic MIEC material, $La_xSr_{1-x}Co_yFe_{1-y}O_{3-\delta}$ family oxides has also been widely utilized as the primary phase of proton-conducting composite air electrode, such as $La_{0.6}Sr_{0.4}Co_{0.2}Fe_{0.8}O_{3-\delta}$ (LSCF) - $BaCe_{0.9}Yb_{0.1}O_{3-\delta}$ (10YbBC) [76], LSCF – $BaCe_{0.9}Y_{0.1}O_{3-\delta}$ [77], LSCF-$Ba(Zr_{0.1}Ce_{0.7}Y_{0.2})O_{3-\delta}$ (BZCY)[78], and $La_{0.6}Sr_{0.4}Co_xFe_{1-x}O_{3-\delta}$ - $BaZr_{0.8}Yb_{0.2}O_{3-\delta}$ (BZYb)[79]. These air electrodes exhibit enhanced electrode catalytic performance compared to single-phase MIEC electrodes due to the additional proton conductor. Besides, the most popular MIEC air electrode, $Ba_{0.5}Sr_{0.5}Co_{0.8}Fe_{0.2}O_{3-\delta}$ (BSCF), is often applied to fabricate composite air electrode. Similar to SSC and LSCF oxides, BSCF was used to mix with the proton conductor to enhance the hydration and proton mobility ability to extend the TPBs of the electrodes, which can be evidenced in BSCF-$BaZr_{0.1}Ce_{0.7}Y_{0.2}O_{3-\delta}$[80], BSCF-$BaZr_{0.1}Ce_{0.7}Y_{0.1}Yb_{0.1}O_{3-\delta}$ (BZCYYb)[81], BSCF-$BaZr_{0.65}Ce_{0.20}Y_{0.15}O_3$[82]. In addition to the typic single perovskite oxides, the double and R-P type perovskite oxides and their novel derivative were also used to fabricated composite air electrode via ball mixing, like $PrBa_{0.9}Ca_{0.1}Co_{2-x}Zn_xO_{5+\delta}$ ($x\leq0.2$) – BZCYYb[83], $Nd(Ba_{0.4}Sr_{0.4}Ca_{0.2})Co_{1.6}Fe_{0.4}O_{5+\delta}$ - BZCYYb[84], $Sr_2Fe_{1.5}Mo_{0.5}O_{6-\delta}$ - $BaZr_{0.1}Ce_{0.7}Y_{0.2}O_{3-\delta}$[85], $Pr_2NiO_{4+\delta}$- $BaZr_{0.2}Ce_{0.6}Y_{0.2}O_{3-\delta}$[86], $La_2Ni_{1-x}Cu_xO_{4+\delta}$($x\leq0.4$) - $BaCe_{0.5}Zr_{0.3}Dy_{0.2}O_{3-\delta}$[87].

Furthermore, triple-conducting air electrodes can also be synthesized by combining other different perovskite oxides. For example, a composite oxide formed by mechanically mixing SSC and $SmBaCo_2O_{5+\delta}$ (SBC) has demonstrated enhanced oxygen reduction capabilities and structural robustness[88]. Additionally, inspired by the observation that isolated boron species in borosilicate form a -B[OH...O(H)-Si]$_2$ structure, which efficiently activates molecular

oxygen and propane to promote dehydrogenation, the surface of the air electrode can be modified with boron species to enhance surface proton acidity[89]. By mechanically ball-milling a trace amount of boric acid (0.5 at.%) with $Pr_4Ni_3O_{10+\delta}$ (PN), a 0.5B-PN composite air electrode was successfully prepared[90]. DFT calculations indicated that boron effectively reduces the formation energy of oxygen vacancies. Furthermore, the introduction of boron on the surface significantly enhances the CO_2 resistance, surface hydration capacity, and Brønsted acid site (BAS, -OH) content of the PN material, thereby boosting the surface ORR kinetics and stability (**Figure 2.9d, e**). At 600 °C, the maximum power density of a cell using the 0.5B-PN air electrode was 149.5% higher than that of a cell using the PN air electrode.

These findings underscore the efficacy of mechanical mixing as a straightforward and efficient approach for fabricating triple-conducting composite electrodes. However, the thermodynamic and electrochemical attributes of the resulting composite electrodes are markedly contingent upon the specific physicochemical properties of the constituent phases chosen and their synergistic blending effects. This is corroborated by the varied electrochemical performances and thermal expansion observed across diverse composite electrode formulations. Thus, meticulous selection of phase compositions and proportions, coupled with judicious control of milling parameters such as rates and durations, is imperative to engineer composite electrodes via mechanical mixing, as these critical parameters exert significant influence on the ultimate performance of the composite electrode.

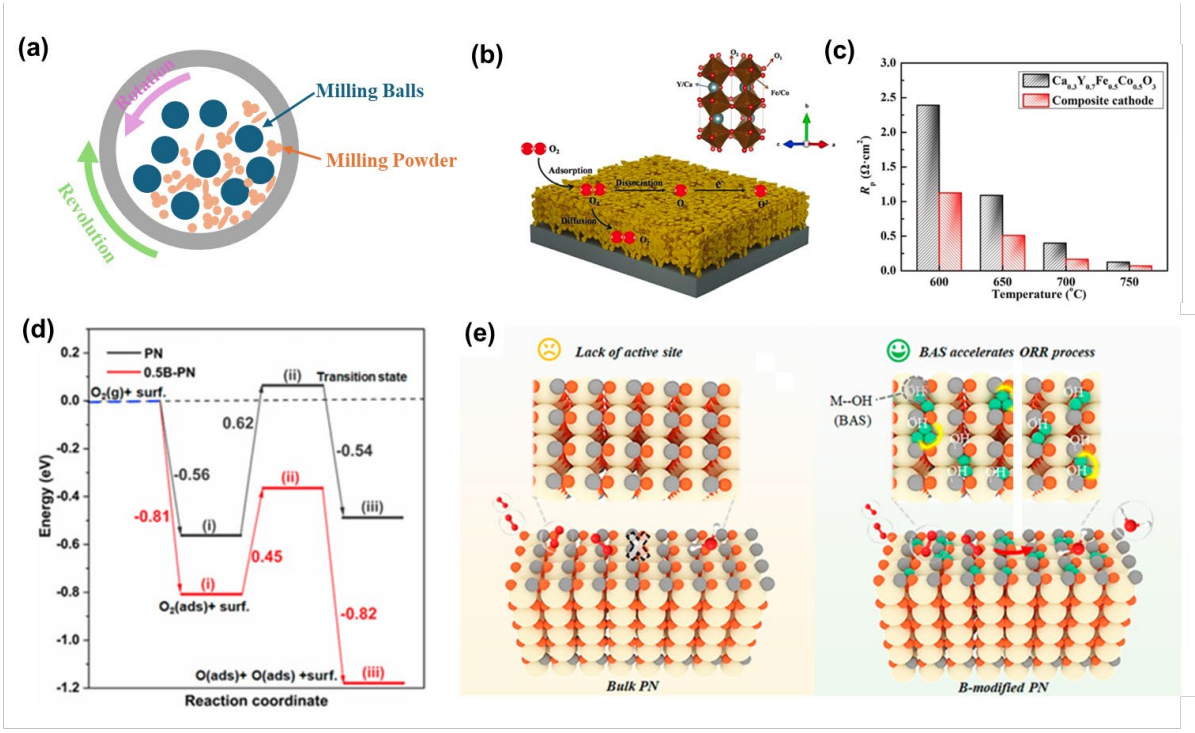

Figure 2.9 (a) A schematic sketch of high energy ball-milling treatment; (b) the schematic diagram of the oxygen diffusion and transfer on CYFC air electrode and (c) ASR values for CYFC and CYFC-BZCY; Reproduced with permission.[75] Copyright (2019), Elsevier. (d) Gibbs free energy required for the ORR process on PN and 0.5B-PN surfaces; (e) Schematic diagram of activation of the PN surface by B. Reproduced with permission.[90] Copyright (2023), American Chemical Society.

2.3.2 Impregnation Modification

In contrast to conventional mechanical mixing approaches, impregnation entails dispersing nano-catalysts onto a pre-prepared scaffold to create composite electrodes. Specifically, the process involves infiltrating a porous framework with a precursor solution, succeeded by thermal treatment to convert the precursor into the corresponding phase or composition on the surface. Simultaneously, the morphology of the impregnated coating can be tailored by the interplay of metal ion adhesion within the precursor solution and the capillary forces of the substrate[91]. These surface nanoparticle coatings exhibit efficient catalytic activity and stability, thereby significantly enhancing the surface microstructure of the porous framework through the nano-size effect, thereby augmenting its surface area to expand the

triple-phase boundary and enhance surface exchange kinetics[92, 93]. Moreover, impregnation coatings can introduce additional nanophases, significantly amplifying the conductivity of porous frameworks. For instance, impregnating a nano-mixed oxygen ion/electron phase into a porous proton-conducting phase electrolyte scaffold or impregnating a proton-conducting phase onto a mixed oxygen ion/electron conducting phase scaffold effectively constructs highly efficient and stable triple-conducting composite air electrodes[94]. Lastly, impregnation can introduce stable materials into the electrode, enhancing its long-term stability and resistance to performance degradation[95, 96].

Infiltrating traditional mixed oxygen ion/electron conductor materials into proton-conducting phases stands as a prevalent methodology for crafting triple-conducting air electrode. For instance, when $Ba_{0.95}La_{0.05}Fe_{0.8}Zn_{0.2}O_{3-\delta}$ is infiltrated onto a BZCYYb scaffold[97], the resulting nano-structured active layer, endowed with commendable proton conductivity and electrocatalytic prowess, effectively enlarges the proton-accessible area at the electrode/electrolyte interface, thereby showcasing augmented ORR kinetics. Another composite air electrode, which is prepared by impregnating BCFZY into a porous $BaCe_{0.6}Zr_{0.3}Y_{0.1}O_{3-\delta}$ proton conductor carrier (**Figure 2.10a, b**), also exhibited superior electrochemical performance compared to the single-phase BCFZY electrode, evidenced by the lower ASR value of the assembled symmetrical cell[41].Considering the superior oxygen ion transport capability of R-P-type perovskites, $(Pr_{0.9}La_{0.1})_2(Ni_{0.74}Cu_{0.21}Nb_{0.05})O_{4+\delta}$ (PLNCN)-infiltrated $BaZr_{0.1}Ce_{0.7}Y_{0.2}O_{3-\delta}$ air electrode has been developed. Benefiting from the enhanced oxygen surface exchange process, the overall electrode reaction kinetics were accelerated with optimized loading (46.1 wt%)[98]. Similarly, the composite electrode fashioned by infiltrating

sub-100 nm $Ba_{0.5}Gd_{0.8}La_{0.7}Co_2O_{6-\delta}$ (BGLC) nano catalysts onto a porous $BaZr_{0.8}Y_{0.2}O_{3-\delta}$ backbone manifests robust OER electrocatalytic activity[99], registering an ASR value of merely 2.87 Ω cm^2 at 500°C. Moreover, upon transforming the surface impregnation layer into $LaCoO_3$[100], the electrocatalytic performance undergoes further enhancement, yielding an ASR value of only 2.18 Ω cm^2 at 500°C, and ensuring sustained operation for 900 hours under a 10% humidity air.

Moreover, recent findings have demonstrated that depositing perovskite nanoparticles onto the surface of mixed oxygen/electron ion conductor frameworks can effectively enhance catalytic activity. By impregnating $BaCoO_{3-\delta}$ (BCO) nanoparticles onto conventional LSCF air electrode surfaces[101], the kinetics of the surface oxygen exchange process catalyzed enabled by BCO are further augmented, leading to notable improvements in the electrochemical performance and durability of BCO-LSCF. DFT calculations have revealed that BCO nanoparticles preferentially deposit by binding with Fe ions on the surface of LSCF (lattice plane: 001), thus utilizing Co ions as active oxygen adsorption centers on LSCF with an energy barrier of -0.81 eV. Furthermore, impregnating $Pr_{0.5}Ba_{0.5}CoO_{3-\delta}$ (decomposes into $Pr_{1-x}Ba_xCoO_{3-\delta}$ and BCO phases) onto the surface of LSCF has also significantly enhanced its ORR/OER catalytic performance[102].

Additionally, perovskite nanoparticle coating can also be sued to suppress segregation trend of the A-site elements in the perovskite oxide backbones. For instance, given the fact that the PBC oxides with favorable ORR/OER catalytic activity often suffer from Ba-enriched surface segregation, leading to faster degradation under high steam containing atmosphere. A fluorite structure nano catalyst of $Pr_{0.1}Ce_{0.9}O_{2+\delta}$ is coated on a PBC surface to fabricate a

composite air electrode[103], resulting an enhanced the ORR/OER catalytic activity and durability due to the coating layer provided more active reaction sites and prevent the segregation of Ba. Moreover, due to the Cr-containing metallic interconnects can degrade the performance of Ba/Sr-containing electrodes by forming $SrCrO_4$, $BaCrO_4$, or $BaCr_2O_4$ on the electrode surface[104], a Ba/Sr-free catalyst coating-$Pr_{0.9}Fe_{0.7}Co_{0.3}O_3$ (PFC) was applied to the surface of the PBSCF electrode to enhance ORR activity and Cr-poisoning tolerance (**Figure 2.10c- e**)[10]. Similarly, to enhance the surface oxygen exchange process and tolerance against steam and CO_2 of the $BaCe_{0.5}Pr_{0.3}Y_{0.2}O_{3-\delta}$ (BCPY) support, the catalyst $PrNi_{0.5}Co_{0.5}O_3$ (PNC) was coated by infiltration (**Figure 2.10f- i**)[105]. PNC exhibited superior catalytic performance and excellent tolerance against steam and CO_2 due to its high ionic-electronic ($H^+/O^{2-}/e^-$) conductivity and absence of alkaline earth metals. CO_2-TPD and EIS results indicated that the PNC-BCPY showed the lowest CO_2 absorption and a slight increase in ASR value in a CO_2-H_2O-containing atmosphere, mainly due to the effective coverage of the alkaline earth metal (Ba) in BCPY by PNC.

It is worth noting that the impregnation process cannot control the size and uniform distribution of nanoparticles on the scaffold. Additionally, the adhesion between the impregnated layer and the scaffold may be compromised by differences in TEC and electrochemical reactions, leading to delamination. These issues inevitably result in reduced electrode performance and limited long-term stability. Furthermore, the high-temperature re-sintering after impregnation and the multiple impregnation steps needed to achieve the desired loading significantly increase both economic and time costs, while also introducing defects and damage to the material's structure and composition. In conclusion, while the impregnation

method can enhance electrode performance, it still presents significant challenges and shortcomings that need to be addressed.

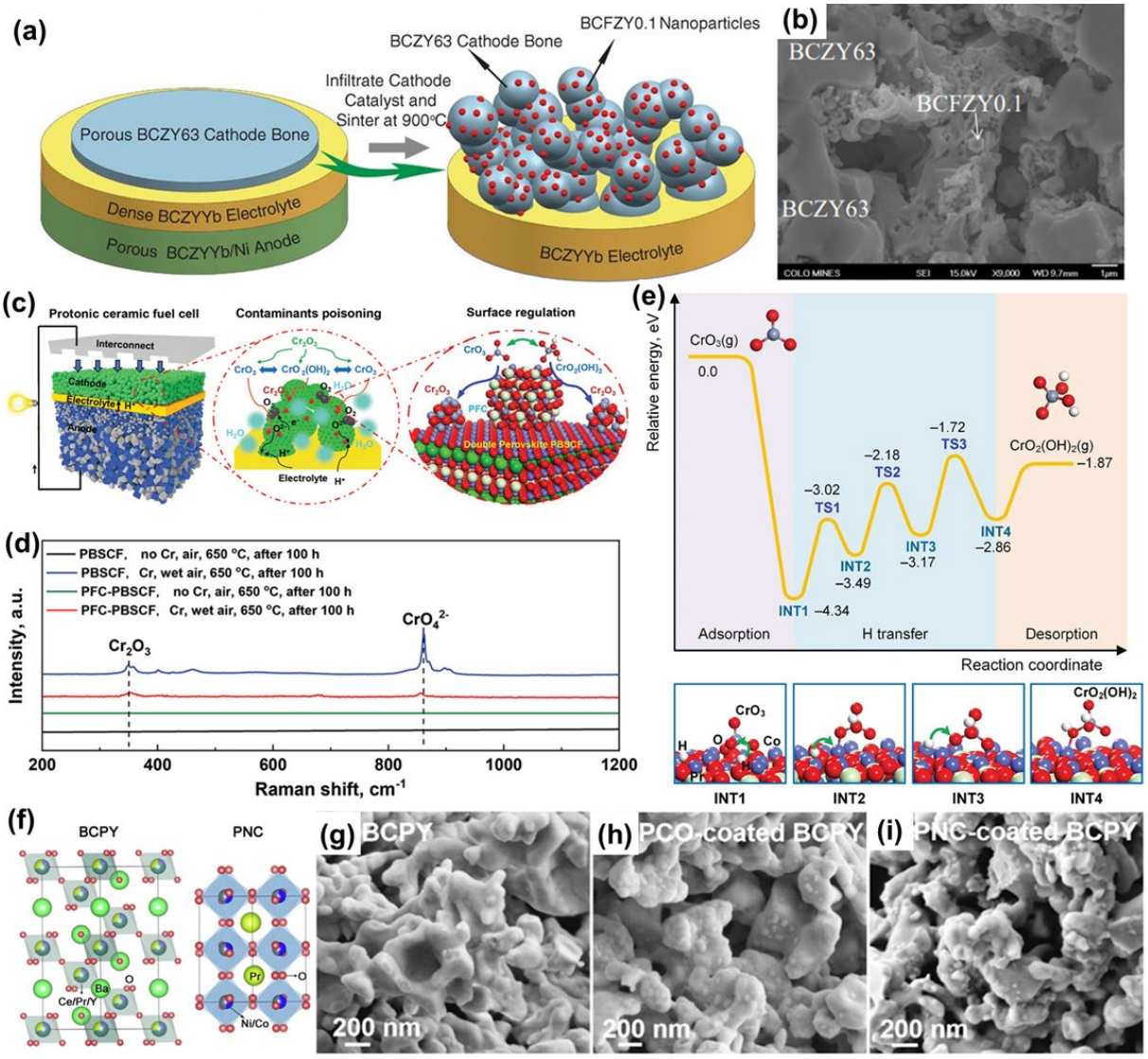

Figure 2.10 (a) Fabrication process of infiltrated air electrode; (b) corresponding SEM images of infiltrated composite air electrode; Reproduced with permission.[41] Copyright (2015), The American Association for the Advancement of Science. (c) schematic illustration of the fuel cell and air electrode in the presence of contaminants (Cr and steam); (d) Raman spectra of bare PBSCF and infiltrated PBSCF electrodes after exposure to wet air with direct Cr alloy contact; (e) minimum energy pathways of the transformation of CrO_3 to $CrO_2(OH)_2$; Reproduced with permission.[10] Copyright (2022), Wiley. (f) Crystal structures of parent BCPY and infiltrated PNC; (g-i) SEM images of bare and infiltrated electrodes. Reproduced with permission.[105] Copyright (2023), Elsevier.

2.3.3 Core-shell Microstructure

The Core-shell architecture, which means incorporating additional phases as the shell to

cover the core material, also plays an important role in fabricating composite electrodes via modifying the surface properties. By incorporating a shell structure on the electrode surface, which functions as a nano catalyst or protective layer, the reactive surface area of porous microstructure air electrode materials (core) can be significantly enhanced, leading to improved stability against H_2O, CO_2, and Cr[106]. Furthermore, when an adequate amount of shell nanoparticles with superior mixed ionic/electronic conductivity forms a continuous charge transport pathway, the electronic and ionic conductivity of the nanocomposite electrode is markedly increased. This heterojunction structure also facilitates grain refinement, preventing excessive agglomeration of internal nanometal particles during high-temperature sintering[107]. These beneficial effects contribute to the development of nanocomposite air electrodes with exceptional electrocatalytic activity and stability.

Many studies have demonstrated that the synergistic effects of core-shell heterostructure exhibit a higher electrochemical performance than the bare air electrode material[108-110]. For instance, shaped coatings are used to inhibit the thermal expansion of grains and the chemical reaction between pollutants to improve the stability of electrodes[111]. Based on these conclusions, a triplet conductive air electrode material with a core-shell structure by impregnating Co onto $BaZr_{0.4}Ce_{0.4}Y_{0.2}O_{3-\delta}$ (BZCY) supports was prepared. The core is BZCY framework, and the outer shell layer contains cubic phase $Ba(Zr_{0.4}Ce_{0.4}Y_{0.2})_{1-x}Co_xO_{3-\delta}$, cubic spinel phase Co_3O_4 and cubic fluorite phase (Ce, Zr, Y)O_2[109]. This electrode displayed a good match with the electrolyte and exhibits stable and efficient ORR catalytic performance in an aqueous atmosphere. In addition, the LSCF (surface layer)-LSM (core) composite electrode with core-shell structure was also synthesized[108]. In addition, Li et al.[110] studied a composite

electrode with a modified $La_2NiO_{4+\delta}$ shell structure on a PBSCF support (core layer) and found that the surface of this core-shell structure is rougher, which provides more activity for the cathode surface reaction. At the same time, the alkaline-earth element-free nature of the LaNi layer alleviates the performance degradation of the electrode due to pollutants.

Moreover, considering that perovskite $SrFeO_{3-\delta}$ has higher oxygen ionic and electronic conductivity, while the R-P type $Sr_3Fe_2O_{7-\delta}$ shows potential for proton conducting ability due to its unique layered structure, a strategy was proposed to create a heterostructure junction by partially converting $SrFe_{0.9}Nb_{0.1}O_{3-\delta}$ (SFN113) to $Sr_3Fe_{1.8}Nb_{0.2}O_{7-\delta}$ (SFN327) on its surface to fabricate a core-shell microstructure (**Figure 2.11a**)[112]. Specifically, the prepared SFN113 powder was mixed with $Sr(NO_3)_2$ at a mass ratio of 1:0.4 in a solution using urea as a chelating agent, Triton X-100 as a dispersant, and deionized water as the solvent. The Sr-species on the SFN113 surface can react with its bulk to in-situ generate R-P type SFN327, forming a heterostructure triple-conducting air electrode with an SFN113 core and a tetragonal SFN327 shell through sintering at different temperatures. Similarly, the core-shell was also observed in the $Ba(Co_{0.4}Fe_{0.4}Zr_{0.1}Y_{0.1})_{0.9}Al_{0.1}O_{3-\delta}$ (BCFZYA) (10%Al doped BCFZY) air electrode due to the rearrangement of atoms in the several nanometer depth surface regions (**Figure 2.11b, c**)[113]. Interestingly, perovskite oxide electrode materials can develop in situ double-shell structures, enhancing electrocatalytic performance beyond the typical single-shell configurations. For instance, the K_2NiF_4-type $La_{1.2}Sr_{0.8}Ni_{0.5}Mn_{0.5}O_{4+\delta}$ (LSNM) air electrode, when annealed in air at 1200°C, forms a dual-layer shell structure featuring a B-site deficient LSNM and a new perovskite phase on its surface[114]. This distinctive tri-layer architecture (core-shell B-shell A) arises from concurrent atom rearrangement and dopant segregation during calcination (**Figure**

2.11d), driven by the elastic and electrostatic interactions of the dopant with the surrounding lattice in the perovskite-related R-P phase oxide LSNM[115-117]. Cation segregation occurs within a 4.5 nm depth surface region (**Figure 2.11e**), while segregated atoms (La, Sr) accumulate within a 2 nm depth surface region, resulting in a bi-shell microstructure. Simultaneously, the B-site deficient perovskite LSNM-B in the B-shell offers substantial capacity for accommodating oxygen species and electron mobility, promoting efficient oxygen charge transfer (**Figure 2.11f, g**). These attributes are highly advantageous for oxygen related reactions.

Although two-phase air electrode materials with a core-shell structure have the above-mentioned advantages due to the protective layer on the surface, it cannot be ignored that the rate-controlling step of the ORR/OER is still mainly limited by the gap of charge transfer sub-step between the electrode bulk phase and the core-shell layer. How to effectively reduce the interphase charge transport resistance is still a key issue in the modification of air electrode materials using core-shell structures. At present, researchers mainly improve the charge transfer step by reducing the thickness of the core-shell layer, such as combining multi-step penetration methods to control the thickness of the core-shell layer[111].

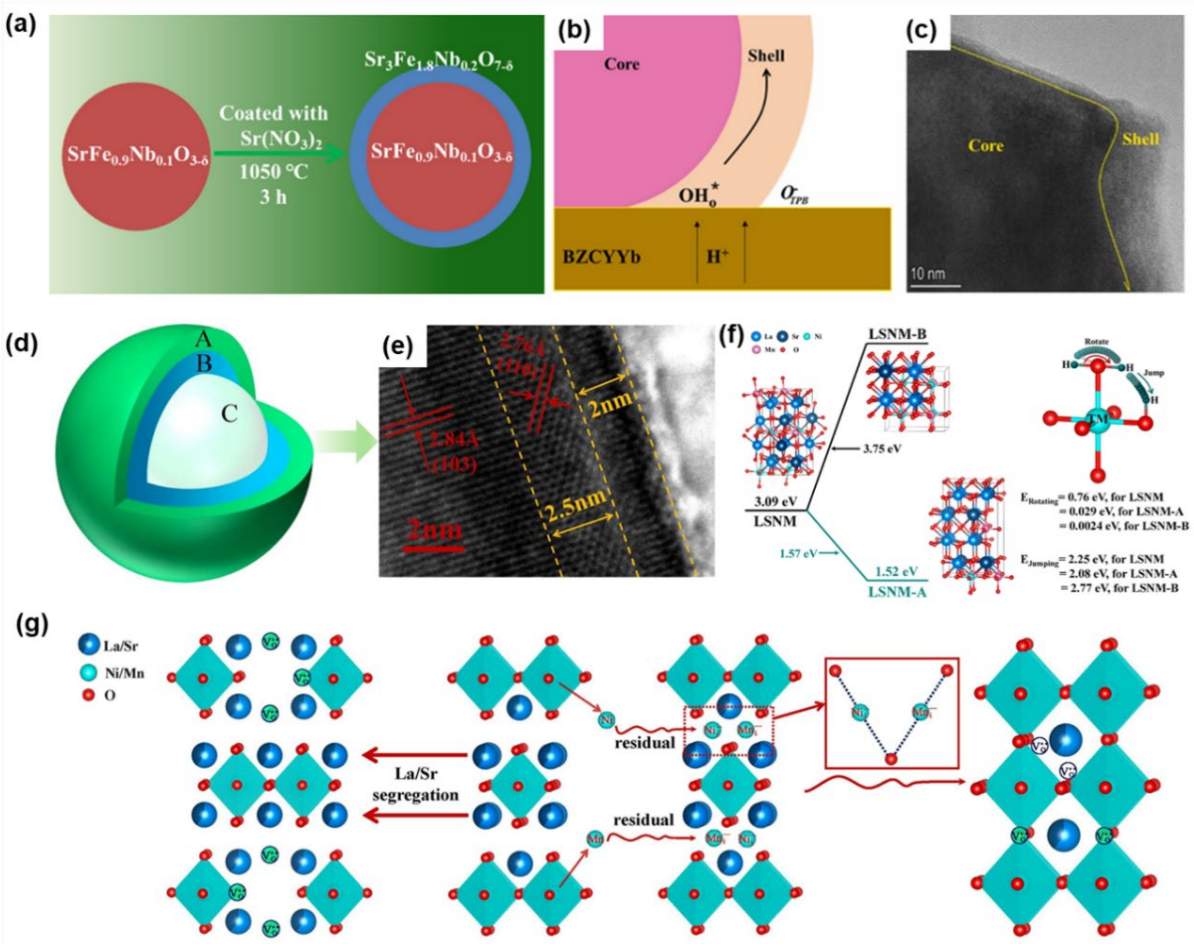

Figure 2.11 (a) The schematic diagram of the core−shell structure SFN113@327; Reproduced with permission.[112] Copyright (2021), American Chemical Society. (b) The enlarged core-shell surface region at the air electrode/electrolyte interface; (c) HR-TEM image of the core-shell structure for BCFZYA ai electrode; Reproduced with permission.[113] Copyright (2023), Elsevier. (d) Schematical diagram and (e) HR-TEM of the core/bi-shell structure for LSNM air electrode; (f) the formation energy of oxygen vacancies comparison of LSNM-A in A-shell, LSNM-B in B-shell, LSNM in C-core and the proton rotating and jumping energy barrier; (g) the phase conversion process for core-bi-shell structure for LSNM material. Reproduced with permission.[114] Copyright (2023), Elsevier.

2.3.4 Self-assembly Strategy

Self-assembly refers to the process whereby a disordered system spontaneously forms an organized structure through interactions among its fundamental building blocks, such as attraction, repulsion, and chemical bonding, without external intervention[118] . This technique promotes the development of nanocomposite materials with multifunctional features through precise design and control of their properties. For composite electrodes, the one-pot synthesis

method is a crucial self-assembly strategy for obtaining nanocrystalline phases with complementary functions[119]. During this process, all components are synthesized simultaneously within the same reaction environment without additional treatment. The interactions between different phases can generate enhanced contact and smaller particles, ensuring intrinsic chemical cooperation among the components, uniform distribution, expanded heterointerfaces, enhanced three-phase boundaries, and robust interfacial cohesion[120].

Self-assembly technology is commonly employed to fabricate nanocomposite electrodes that possess both proton/electron-conducting phases and oxygen ion/electron-conducting phases to ensure the high triple conductivity. For example, $BaCo_{0.7}(Ce_{0.8}Y_{0.2})_{0.3}O_{3-\delta}$ (BCCY) will spontaneously reconstructs into a Ce-rich H^+/e^- conducting phase close to $BaCe_{0.8}Y_{0.2}O_{3-\delta}$ (P-BCCY) and a Co-rich O^{2-}/e^- conducting phase close to $BaCo_{0.9}(Ce_{0.8}Y_{0.2})_{0.1}O_{3-\delta}$ (M-BCCY) after one-pot sintering (**Figure 2.12a- c**)[121]. Furthermore, these two phases are well-mixed and intimately connected within the micrometer-sized grains (0.5-1.0 μm) at the nanoscale (P-MCCY-155.2 nm and M-BCCY-132.8 nm). Such nanocomposite also holds a high triple conducting capability. Moreover, when the Ce was totally replaced by Zr for BCCY, the nanocomposite $BaCo_{0.7}(Zr_{0.8}Y_{0.2})_{0.3}O_{3-\delta}$ (BCZY) will self-assembled into three functional phases: a major cubic Co-rich phase (59.4 wt%, space group: Pm-3m), a minor cubic Zr-rich phase (35.6 wt%, space group: Pm-3m), and a very small amount of hexagonal Co-rich phase (5.0 wt%, space group: P63/mmc) (**Figure 2.12d- f**)[122]. The catalytic activity and stability are enhanced due to the strongly interacting interface introduced by the interdiffusion of Co and Zr ions. Similar phenomena have been observed in cobalt-free materials, as the nanocomposite

electrode $BaCe_xFe_{1-x}O_{3-\delta}$ (x = 0.36, 0.43, and 0.50) self-assembles into two phases after high-temperature sintering: the cubic perovskite (CP) and orthorhombic perovskite (OP) structures[123]. The CP phase $BaFeO_{3-\delta}$ demonstrates high oxygen ion permeability and electron conductivity, while the OP phase $BaCeO_{3-\delta}$ acts as a proton conductor. The self-assembled CP/OP mixture can be controlled by adjusting the Ce/Fe ratios to tailor the in-situ heterojunction structure and triple conductivity. Furthermore, the nominal composition $BaCe_{1-(x+0.2)}Fe_xY_{0.2}O_{3-\delta}$ ($0.1 \leq x \leq 0.6$) with Y substituting for Ce also self-assembles to form a Fe-rich cubic phase and a Ce-rich orthorhombic/trigonal phase via one-pot sol-gel method (**Figure 2.12g- i**)[124]. The proton concentrations of the two-phase composite $BaCe_{0.4}Fe_{0.4}Y_{0.2}O_{3-\delta}$ in 17 mbar pH_2O reached 1.4 mol% due to the suitable ratios of different phases. Similar trend was also in the optimized $BaCe_{0.16}Y_{0.04}Fe_{0.8}O_{3-\delta}$ nanocomposite electrode, which were composed of a cubic $BaFe_x(Ce/Y)_{1-x}O_{3-\delta}$ phase (Pm-3m, 98.6wt%) and orthorhombic $Ba(Ce/Y)_xFe_{1-x}O_{3-\delta}$ phase (Pmcn, 3.4wt%)[125]. Additionally, both Ce-Zr and Co-Fe contained nanocomposite-$Ba(CeCo)_{0.4}(FeZr)_{0.1}O_{3-\delta}$ (BCCFZ) will also conducted self-construction process, and the 40wt% mixed ion and electron-conducting phases of $BaCo_{1-(x+y+z)}Ce_xFe_yZr_zO_{3-\delta}$ (M-BCCFZ, Pm-3m) and a dominant (60%) proton-conducting phase of $BaCe_{1-(x+y+z)}Co_xZr_yFe_zO_{3-\delta}$ (H-BCCZF) were formed[126]. This low-cobalt-content self-assembled cubic-rhombohedral nanocomposite material exhibits suitable triple-conducting properties with a low enthalpy of protonation of -30 ± 9 kJ mol^{-1} and a low TEC of 9.6×10^{-6} K^{-1}. Such phases separation may derive from the significant differences between the B-site (Ce/Zr and Co/Fe) ionic radii[124], this leads to automatic restructuring within the of the parent lattice to achieve a thermodynamically stable structure.

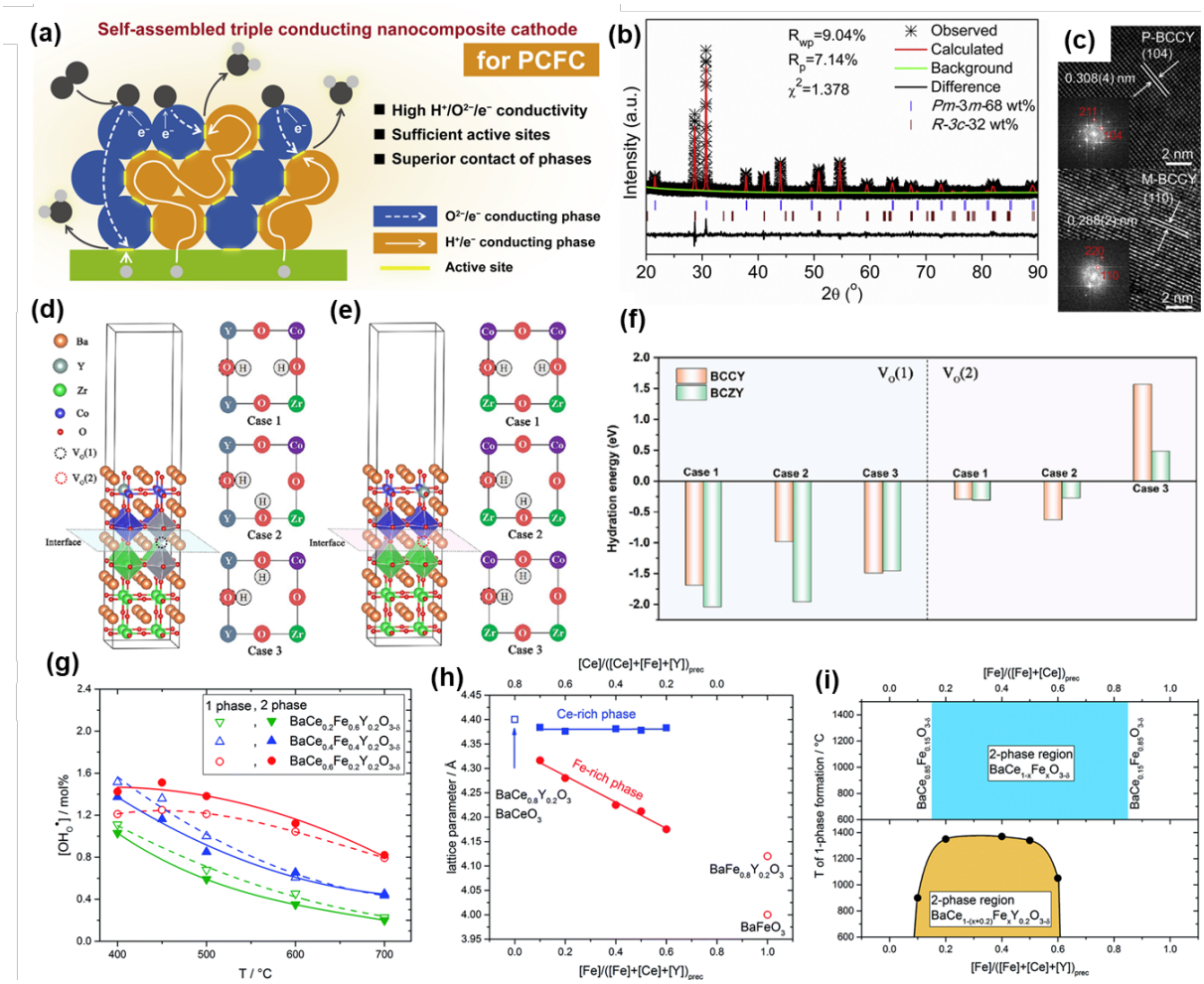

Figure 2.12 (a) The electrode reaction processes for self-assembled nanocomposite electrode; (b) refined XRD profiles and (c) HR-TEM image of one-pot synthesized composite; Reproduced with permission.[121] Copyright (2019), Elsevier. (d-e) Schematic diagram of hydrated electrode interface and (f) hydration energy of BCCY and BCZY electrodes; Reproduced with permission.[122] Copyright (2023), Elsevier. (g) comparison of the proton concentration of two-phase nanocomposites; (h) lattice parameters as functions of the Fe and Ce contents; (i) the phase diagram shows the miscibility gaps. Reproduced from Ref.[124] with permission from the Royal Chemical Society.

2.3.5 In-situ Exsolution Strategy

Exsolution is a controlled phase separation technique used to uniformly grow nanoparticles on a support, with perovskite oxides often serving as host materials due to their stability under redox conditions and high temperatures, as well as their ability to be doped and maintain non-stoichiometry. These nanoparticles (NPs), dispersed across the surface of oxide supports, significantly enhance catalytic activity through improved surface and interface

properties, such as increased active surface area and phase boundaries. Additionally, exsolved nanoparticles are strongly anchored to the oxide support, creating robust particle-substrate interactions. This anchoring results in exceptional resistance to agglomeration, carbon coking, and sulfur poisoning, enabling long-term stable operations[127-130]. However, exsolution primarily occurs in reducing atmospheres (e.g., H_2) and, in oxidizing environments like the air electrode working atmosphere at high temperatures, these nanoparticles may gradually re-dissolve into the parent lattice, raising stability concerns for air electrode materials. Therefore, efforts are ongoing to identify suitable driving forces for the evolution and develop stable nanoparticles that can withstand wet air conditions to fabricate the nanocomposite air electrode for R-PCECs.

Utilizing H_2O as a mediator to induce the in-situ formation of active catalytic nanoparticles has demonstrated significant potential for enhancing electrochemical reactions. For example, when the highly moisture-tolerant layered perovskite oxide $PrBa_{0.8}Ca_{0.2}Co_2O_{5+\delta}$ (PBCC) is exposed to wet air (3 vol% H_2O-air), Ba ions segregated by H_2O spontaneously combine with Co ions from the host oxide through topotactic cation exchange, resulting in the in-situ generation of $BaCoO_{3-\delta}$ (BCO) catalysts on the bulk PBCC[131, 132]. This process leads to a heterogeneous catalyst-coated surface, as evidenced by the SEM, TEM, EDX and Raman profilometry of the protonated PBCC sample[131, 132]. Furthermore, the oxygen surface exchange kinetics are significantly improved due to the lower activation energy required for BCO nanoparticles (0.60 eV versus 1.42 eV), as revealed by DFT calculations[131]. BCO nanoparticles stands out as a superior catalyst particle, maintaining stability in high steam and CO_2 atmospheres, and ensuring robust performance in both FC and EC modes[132]. The in-situ

exsolution of BCO NPs was also observed in a $Pr_{1-x}Ba_xCoO_{3-\delta}$ thin film coated $(La_{0.6}Sr_{0.4})_{0.95}Co_{0.2}Fe_{0.8}O_{3-\delta}$ (LSCF) air electrode exposed to high concentrations of water[102]. This heterogeneous catalyst coating significantly enhanced the electrocatalytic activity and stability of the LSCF electrode, attributed to improved surface oxygen exchange, rapid proton diffusion, and efficient H_2O and O_2 dissociation on the catalysts, as confirmed by DFT analyses. Similarly, $PrBaCo_{1.6}Fe_{0.2}Nb_{0.2}O_{5+\delta}$ (PBCFN) can interact with steam to generate Nb-deficient particles $PrBaCo_{1.6}Fe_{0.2}Nb_{0.2-x}O_{5+\delta}$ on its surface[133]. SEM images of the PBCFN electrode before and after testing revealed the presence of these nanoparticles, confirmed by HAADF TEM results, which indicated they are Nb-deficient and provide more active reaction sites in wet air. Comparable Nb-deficient NPs were also formed on the $Ba_{0.9}Co_{0.7}Fe_{0.2}Nb_{0.1}O_{3-\delta}$ (BCFN) air electrode skeleton via a water-promoted surface restructuring process[134]. Calculations of segregation energy (E_{segt}) for co-dopant cations and their interaction with steam indicated a segregation order of Co > Fe > Nb, leading to Nb-deficient NPs.

When a novel air electrode material, $Ba_{1-x}Gd_{0.8}La_{0.2+x}Co_2O_{6-\delta}$ (BGLC), was used in R-PCEC in electrolysis mode at 600 °C under 1.5 bar of steam for 72 h, partial substitution of Ba with La ($x < 0.5$) resulted in two phases: double perovskite and hexagonal BCO[135]. Indeed, XRD analysis showed that BGLC with 50% Ba substitution ($x = 0.5$) remained stable under these conditions, without BCO precipitation. These findings may suggest that both high steam concentrations and the unique lattice structure (segregation cations and its interaction with neighboring atoms and oxygen vacancies) contribute to in-situ exsolution of NPs. Another sample consisting of this is the A-site doping air electrode. Specifically, $BaCo_{0.4}Fe_{0.4}Zr_{0.18}Y_{0.02}O_{3-\delta}$, a well-known TCO air electrode, remains stable in wet air.

However, partial replacement of Ba with monovalent alkali metals (Li, Na, K) to fabricate $K_{0.05}Ba_{0.95}Co_{0.4}Fe_{0.4}Zr_{0.18}Y_{0.02}O_{3-\delta}$ (KBCFZY) led to the exsolution of BaO_x on the surface in humidified air (**Figure 2.13a- c**)[136]. This exsolution is caused by the formation of barium and oxygen vacancies facilitated by A-site acceptor doping, and DFT results showed a decrease in oxygen vacancy formation energy from 0.10 to -0.20 eV after K-doping. Additionally, water vapor likely contributes to this process through hydration and hydrogenation reactions that redistribute holes and redox-active elements, triggering BaO_x exsolution via lattice cation vacancy formation. Additional factors such as relaxation of lattice strain and defects' interactions may also contribute. Moreover, the highly basic BaO_x phases can act as catalysts for acid-base reactions, particularly hydration, enhancing the electrode's activity by facilitating proton incorporation. One more similar instance of water-mediated exsolution involves Ag-doped $BaCo_{0.4}Fe_{0.4}Zr_{0.1}Y_{0.1}O_{3-\delta}$ (BCFZY-Ag)[137]. To be specific, when exposed to a humid atmosphere, the redox-active elements (Ag^+ in this case) in protonic conducting oxides react with water through hydrogenation, consuming electron holes generated by the exsolution process (**Figure 2.13d, e**). This promoted the exsolution of Ag^+ with extreme reducibility, resulting in in-situ formation of Ag nano catalysts on the BCFZY surface without additional treatment (**Figure 2.13f**). Notably, unlike other metal oxide catalysts with generally low electronic conductivity and thus slow down the charge transfer process on the electrode surface, Ag remains outstanding electronic conductivity facilitates charge transfer on triple-conducting electrodes. Furthermore, it is stable under high oxygen partial pressure conditions and maintains excellent gas absorption/desorption and anti-poisoning properties, resulting in the

Ag-BCFZY air electrode exhibiting robust dual catalytic performance and stability for both ORR and OER processes.

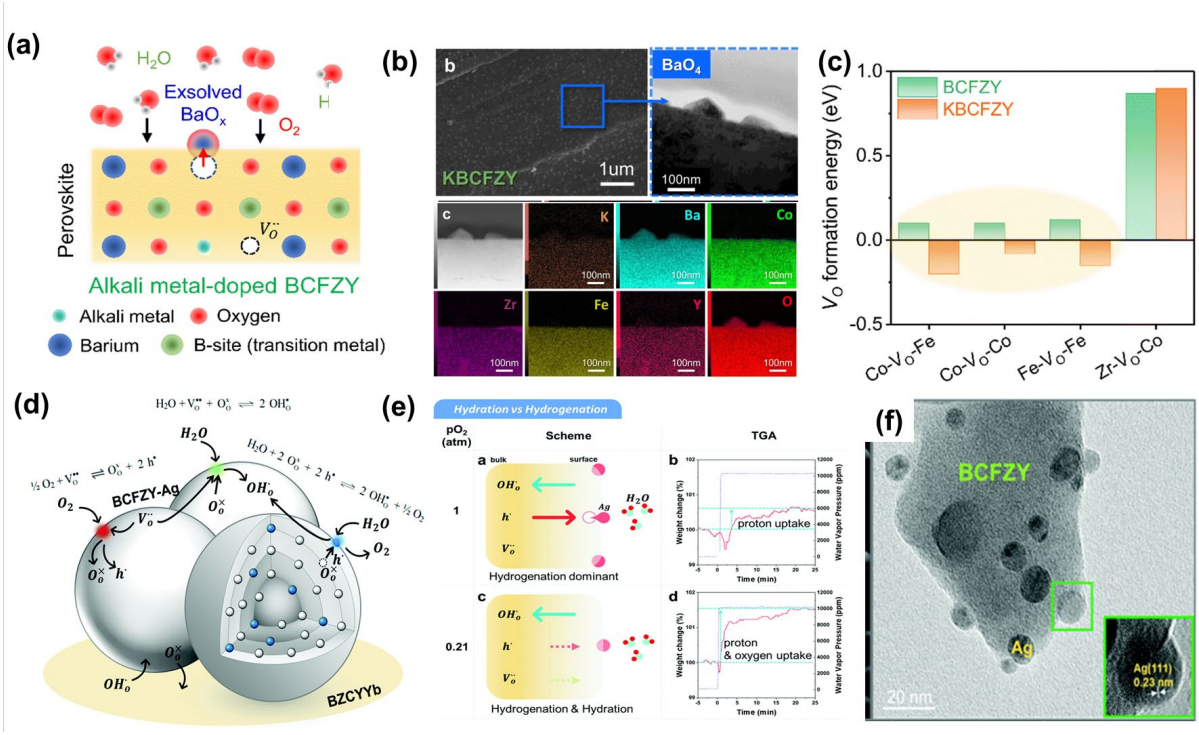

Figure 2.13 (g) reaction mechanism of ABCFZY in humidified air; (h) BaO_x exsolution onto KBCFZY (FE-SEM, TEM, HR-TEM and FFT pattern) and the mapping results; (i) the DFT calculated oxygen vacancy formation energy; Reproduced from Ref.[136] with permission from the Royal Chemical Society. (j) Schematic diagram of water-mediated ex-solution; (k) water uptake and thermogravimetric profiles of dense BCFZY-Ag pellets; (l) HRTEM image of exsolved Ag nanoparticles, (inset) magnified image. Reproduced from Ref.[137] with permission from the Royal Chemical Society.

CHAPTER 3 Methodology

3.1 Materials Synthesis

3.1.1 Electrolyte and Air Electrode

The nominal electrolyte and air electrodes powders are prepared through the method of sol–gel EDTA-citric acid (CA) complexing[138]. Taking the synthesis of the electrolyte material $BaZr_{0.1}Ce_{0.7}Y_{0.1}Yb_{0.1}O_{3-\delta}$ (BZCYYb) as a case, the corresponding metal ions from the perovskite oxides, $Ba(NO_3)_2$, $Zr(NO_3)_2$, $Ce(NO_3)_3$, $Y(NO_3)_3$, $Yb(NO_3)_3$,are accurately weighed according to the stoichiometric ratio of the chemical formula. Subsequently, they are dissolved in deionized water at 80 °C with thorough stirring to ensure complete dissolution. Citric acid and EDTA are then added in a ratio of metal ions: citric acid: EDTA = 1:2:1, and the pH of the solution is adjusted to approximately 7 using ammonia solution to achieve complete chelation of the metal ions. The solution is further subjected to rapid stirring and heating until the solvent is completely evaporated, resulting in the formation of a gel-like substance. This gel is transferred to an oven and dried at 170 °C for 10 hours to obtain the precursor. Following this, the precursor is transferred to a high-temperature furnace and calcined at 1050 °C for 5 hours. Upon annealing, the desired electrolyte powder sample is obtained.

Regarding the air electrode material, the synthesis process is like the electrolyte powder synthesis process. It simply requires changing the specific metal nitrate salts according to the designed material for the air electrode.

3.1.2 Fuel Electrode

The fuel electrode utilized in our R-PCEC fabrication comprises NiO-BZCYYb, synthesized via the following procedure. Firstly, ultrafine NiO and pre-prepared BZCYYb

powders are meticulously weighed in a ratio of 6.5:3.5. Subsequently, 10% starch is added as a pore-forming agent along with 30 ml of anhydrous ethanol serving as the solvent. The resulting solution is subjected to milling in a high-energy ball mill at a rotational speed of 400 revolutions per minute for a duration of 2 hours to ensure thorough mixing. Following milling, the solution is dried in a 120°C oven until a dry powder residue is obtained, constituting the finalized fuel electrode material. Herein, The NiO, starch, and anhydrous ethanol utilized in this process are all commercially sourced materials with a purity of 99.9%.

3.2 Cells Fabrication

3.2.1 Electrode Slurry

1 g of the phase-forming electrode powder was accurately weighed and combined with 10 mL of isopropanol, 2 mL of ethylene glycol, and 0.6 mL of propanetriol in a zirconia ball mill jar. Subsequently, the mixture was subjected to grinding in a planetary ball mill at a rotational speed of 400 rpm for a duration of 2 hours. Following this milling process, the resulting electrode slurry was retrieved and prepared for subsequent utilization.

3.2.2 Symmetrical Cell

The fabrication of the symmetrical cell commences with the preparation of a dense electrolyte substrate. This involves meticulously blending the BZCYYb electrolyte powder with 1% NiO (utilized as a sintering aid), followed by compacting the resultant powder under a uniaxial pressure of 250 MPa to attain the desired shapes. Subsequently, the formed specimens undergo sintering in a muffle furnace at 1450 °C for 5 hours, with controlled heating and cooling rates of 3°C/min and 5°C/min, respectively. After polishing the electrolyte disks to achieve a smooth surface texture, the air electrode slurry is uniformly sprayed onto both

faces of the electrolyte. During the spraying process, the electrolyte substrate is securely positioned on a heating platform set to a temperature of 170 °C. Upon completion of drying, the precursor material is transferred to the muffle furnace for additional sintering at 1000 °C for a duration of 2 hours. Ultimately, silver paste is applied to both sides to serve as current collectors, thereby concluding the meticulous preparation of the symmetrical cell samples.

3.2.3 Single Cell

The single cells fabricated in this research adopt a fuel electrode-supported structure to mitigate the unfavorable impact of electrolyte ohmic resistance. Initially, 0.4 g of the prepared fuel electrode powder was weighed and uniaxially pressed at 2 MPa pressure to form a compact base. Subsequently, 0.015 g of electrolyte powder was evenly loaded onto this substrate, followed by another co-pressing step at 4 MPa to create a half-cell configuration. This precursor was then transferred to a muffle furnace and sintered at 1400 °C for 5 hours to enhance its density and strength. Following this, the corresponding air electrode slurry was applied onto the electrolyte layer surface using a spray gun at 170 ºC. Subsequently, the sample underwent co-sintering at 850°C for 2 hours in a high-temperature furnace to achieve a fully integrated single-cell structure.

Prior to conducting tests on this single cell, it is essential to apply silver paste as current collectors on the side of the air electrode. This completes the assembly of the single cell, rendering it ready for testing.

3.3 Bar Samples Preparation

The block-shaped samples were intended for conducting tests on the electrical conductivity relaxation and thermal expansion coefficient. The specific preparation procedure

involved initially weighing 0.7 g of fresh air electrode powder into a mortar. Subsequently, 1 mL of polyethylene glycol was added to the mortar for thorough mixing. The resulting mixture was then transferred to a split mold, where it was evenly spread and subjected to a pressure of 250 MPa to form a strip sample measuring 1.0*0.5*0.5 cm^3. Following this, the sample was transferred to a muffle furnace and sintered at 1150°C for 5 hours to obtain dense strip samples exhibiting a metallic luster.

3.4 Materials Characterization

To comprehensively investigate the various physicochemical properties of the modified materials, a series of characterization methods were employed to provide accurate insights. X-ray diffraction (XRD, Rigaku SmartLab 9kW) was utilized to examine the phase composition of the synthesized materials, with refined results further confirming their composition content and relevant lattice parameters by using the Opensource Fullprof Suite software. Scanning electron microscopy (SEM, TESCAN MAIA) was extensively used to observe the microstructures of both the prepared materials and the overall structure of the cells. High-resolution transmission electron microscopy (HRTEM, America, FEI Tecnai F20) and its mapping results were employed to analyze variations in the interplanar spacing at the nanoscale and the distribution of constituent elements. Thermogravimetric analysis (TG, Germany, Netzsch TG 209 F3 Tarsus) and temperature-programmed desorption (TPD) were employed to analyze the oxygen vacancy concentration and lattice oxygen activity of the synthesized materials at high temperatures. X-ray photoelectron spectroscopy (XPS, Thermo Fisher Scientific Nexsa) was employed to provide information on the types and valence states of various elements on the material surfaces. Synchrotron radiation techniques were used to

further explore changes in the chemical environment of the bulk materials, including coordination environments, coordination bonds, coordination numbers, bond lengths, bond angles, and valence states. The electronic conductivity relaxation (ECR) testing was employed to characterize the surface exchange and bulk transport kinetic properties of oxygen ions or protons in bulk samples under different conditions.

All spin-polarized DFT calculations for periodic material systems were performed with the Vienna Ab initio simulation package (VASP) using the projector-augmented wave (PAW) method. The exchange–correlation function was handled using the generalized gradient approximation (GGA) formulated by the Perdew-Burke-Ernzerhof (PBE). An effective U value of 4.0 eV for Fe and 3.3 eV for Co were determined using the Hubbard U model (DFT + U). The van der Waals (vdW) interactions are described with the DFT-D3 method in Grimme's scheme. The interaction between the atomic core and electrons was described by the projector augmented wave method. The plane-wave basis set energy cutoff was set to 500 eV. The Brillouin zone was sampled with a 3 × 3 × 1 grid centered at the gamma (Γ) point for geometry relaxation. All the slabbed models possessed a vacuum spacing of ≈15 A˚ sampled, ensuring negligible lateral interaction of adsorbates. The bottom layers about half of the structure were kept frozen at the lattice position. All structures with a dynamic magnetic moment were fully relaxed to optimize without any restriction until their total energies were converged to $< 1\times10^{-6}$ eV, and the average residual forces were < 0.02 eV/Å.

3.5 Electrochemical Measurement

3.5.1 Symmetrical Cell

The polarization resistance of the symmetrical cells is measured by the electrochemical

impedance spectroscopy (EIS) using Solarton 1260 and Solarton 1287 equipment within the temperature range of 450-650°C. Nyquist plots were obtained under open circuit voltage (OCV) conditions with a 20 mV AC amplitude in the frequency range of 10^6 to 10^{-1} Hz. The gas flow rate was maintained at 100 ml/min throughout the experiments. The testing atmospheres with different oxygen partial pressures were achieved by adjusting the flow rate ratio of oxygen, while varying water vapor pressures were accomplished by placing the bubbler at different temperatures. After switching the atmosphere during the experiment, a waiting period of 2 hours was observed to ensure stabilization before conducting the tests.

3.5.2 Single Cell

The i-V-p curves of the fuel electrode-supported single cells are obtained using a four-probe configuration with the help of Keithley 2440 source meter equipment, covering the temperature range of 450-650°C. EIS results were obtained using Solarton equipment to determine the ohmic and polarization resistance with a 20 mV AC amplitude in the frequency range of 10^6 to 10^{-1} Hz. During fuel cell operation, the fuel electrode side was supplied with pure H_2 (50 ml/min), while the oxygen electrode was exposed to ambient air. In the electrolysis operation mode, the hydrogen side continued to receive the same gas (dry hydrogen) as mentioned in the fuel cell mode, while the atmosphere of the oxygen electrode was switched to wet air (3% H_2O-air) at a flow rate of 100 ml/min.

During the testing procedure, the temperature was adjusted at a rate of 2 °C/min, and the system was allowed to stabilize for 30 minutes before conducting the tests. Similarly, when switching between different atmospheres for testing, a waiting period of 1 hour was needed.

CHAPTER 4 Unlocking Triple Conductivity in Air Electrodes via Anion Engineering

4.1 Introduction

As mentioned in Chapter 1, the R-PCECs emerge as a promising candidate for energy conversion and storage (**Figure 4.1**) due to the advantages of encompassing a reduced activation energy for proton transport, decreased working temperature (promoting swift startup and enhanced durability), elevated fuel utilization, and diminished cost[25, 134, 139].

Up to now, extensive efforts have been devoted by researchers to find effective methods to develop air electrodes with high triple conduction properties[101, 132, 140].

The state-of-art $Ba_{0.5}Sr_{0.5}Co_{0.8}Fe_{0.2}O_{3-\delta}$ (BSCF), as reported as a typic TCO, shows excellent performance as an air electrode for SOFC but its performance for PCFC is low, partly due to the low proton conductivity and sluggish ORR catalytic activity in a water-containing environment at intermediate temperatures[121, 141].Therefore, to further improve the electrocatalytic activity of the BSCF perovskite oxide, A-and B-site cationic doping involving the introduction of elements such as potassium (K), praseodymium (Pr), and phosphorus (P) into lattice of based oxides has been employed to derive $Ba_{0.4}K_{0.1}Sr_{0.5}Co_{0.8}Fe_{0.2}O_{3-\delta}$ (BKSCF), $PrBa_{0.5}Sr_{0.5}Co_{1.5}Fe_{0.5}O_{5+\delta}$ (PBSCF), and $Ba_{0.5}Sr_{0.5}(Co_{0.8}Fe_{0.2})_{0.95}P_{0.05}O_{3-\delta}$ (BSCFP0.05) functional air electrode materials with improved ORR/OER[50, 142, 143]. Other peculiar air electrode materials with $H^+/e^-/O^{2-}$ conduction properties have been substantially improved for proton conducting oxides applications by doping either Zr, Ni, or Mg in their lattice as in the case of $Sr_2Fe_{1.5}Mo_{0.5}O_{6-\delta}$[144], $La_{0.8}Sr_{0.2}CoO_{3-\delta}$ [145]and BCFZY[44, 45]. It should be emphasized that the enhanced ORR/OER catalytic performance of these doped electrodes mainly due to the

increased oxygen vacancy concentration and improved proton uptake and conduction properties. In fact, in addition to cationic site substitution, anionic site doping has also been considered as an effective way to tune the diffusion behavior of the conducting species in oxides to achieve desired characteristic[146-148]. However, few related works have been reported about the ORR/OER catalytic performance regulation of TCO air electrodes through anion engineering.

Herein, we propose a practical approach of systematically introducing a small amount of anion substitution on the oxygen site of a prominent air electrode material, BSCF, to achieve a superior TCO air electrode. Through the utilization of different electronegative elements ($F^{-}>O^{2-}>Cl^{-}$), the oxygen chemical environment within the material matrix was altered, leading to the weakening metal-oxygen chemical bond and more high-efficiency O^{2-}/H^{+} transport paths. This modification promotes bulk migration ability of the electrode and significantly improves its proton uptake and conduction performance under humidified conditions. The resulting electrode, $Ba_{0.5}Sr_{0.5}Co_{0.8}Fe_{0.2}O_{2.9-\delta}F_{0.1}$ (BSCFF) exhibits enhanced ORR/OER catalytic activity, offering a rational design strategy for fabricating high-performance R-PCEC with favorable operating stability.

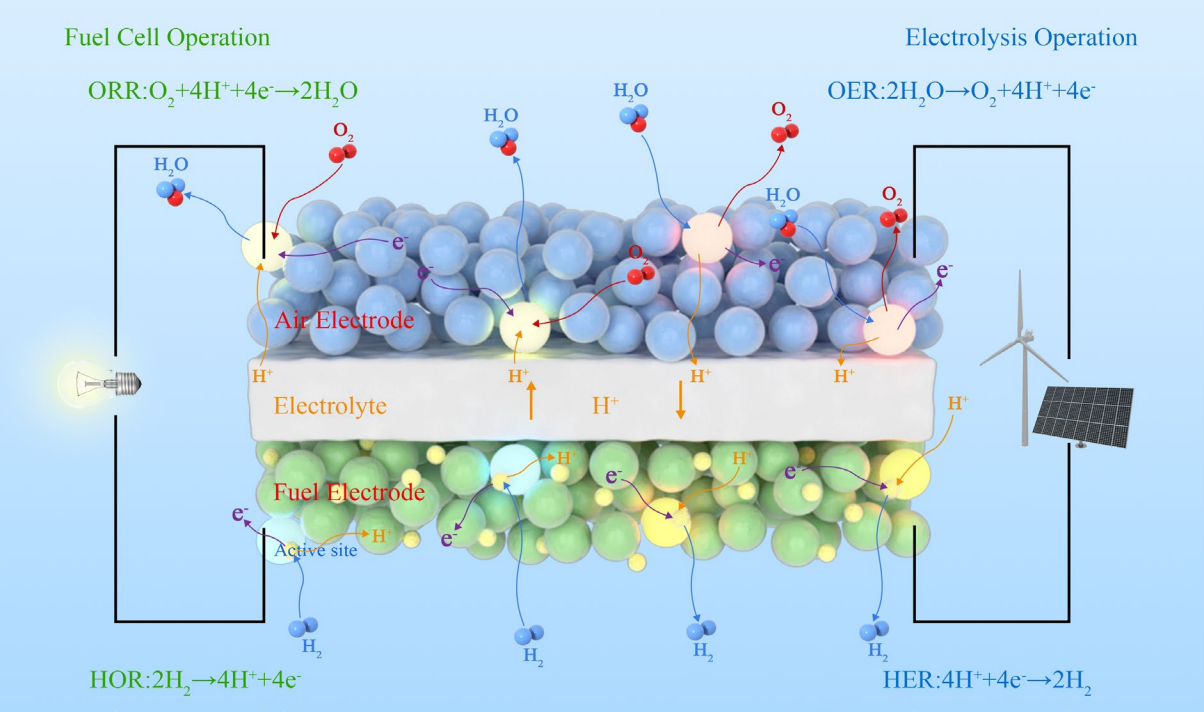

Figure 4.1 Schematic diagram of R-PCEC in fuel cell and electrolysis operation modes

4.2 Results and Discussion

4.2.1 Structural Evolution

As previously mentioned in chapter 3, the primary anion dopants (F^- and Cl^-) substituted into the oxygen sites of BSCF was achieved through the partial replacement of the traditional $Sr(NO_3)_2$ with SrF_2 or $SrCl_2$ compounds during the synthesis process. The remarkable stability of SrF_2 or $SrCl_2$, as shown in **Figure 4.2**, confirms the possibility of successful incorporation.

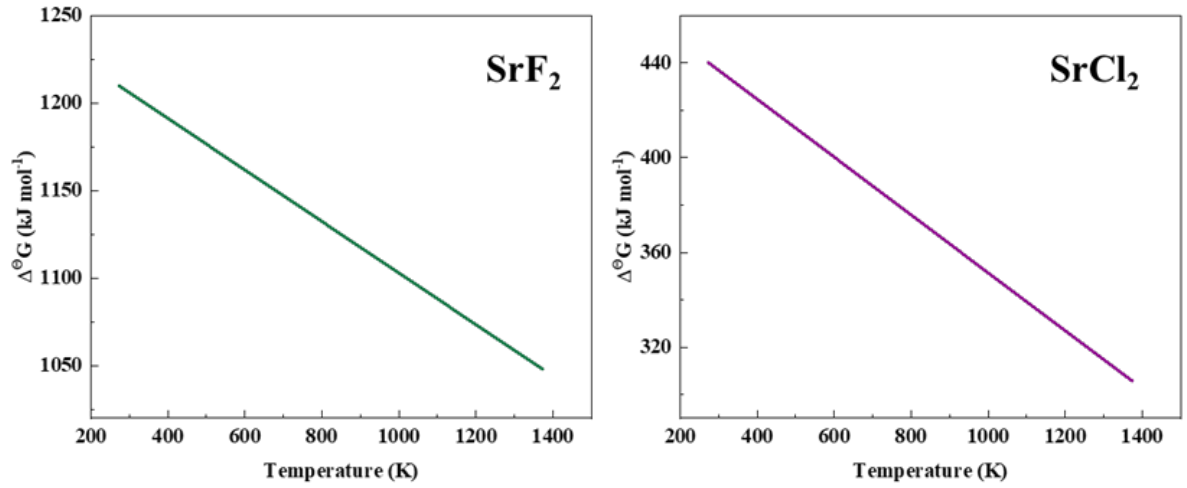

Figure 4.2 The standard Gibbs free energy change ($\Delta^{\Theta}G$, $kJ \cdot mol^{-1}$) of reactions (a)

$2SrF_2+O_2 \rightarrow 2SrO+2F_2$ and (b) $2SrF_2+O_2 \rightarrow 2SrO+2F_2$. The positively high value of ($\Delta^{\Theta}G$) means the reactions are hard to conduct, which indicates the doping F^- and Cl^- is stable in this composite after high-temperature sintering.

Figure 4.3a- c show the refined room temperature XRD patterns of BSCF, BSCFF, and $Ba_{0.5}Sr_{0.5}Co_{0.8}Fe_{0.2}O_{2.9-\sigma}Cl_{0.1}$ (BSCFC) after calcination for 1000 °C in ambient air. **Figure 4.3d** compares the unrefined diffraction patterns of the BSCFF, BSCFC, and BSCF. The diffraction peaks confirm that the anions (F^- and Cl^-) were successfully incorporated in the lattice structure of the BSCF without any impurity phase (such as SrF_2 or $SrCl_2$ secondary phases). The Rietveld refinement results indicated that BSCF, BSCFF and BSCFC perovskite oxide all have a cubic structure with a space group Pm-3m. From **Figure 4.3d**, the higher diffraction angle of BSCFF from 30.7° to 32.5° indicate a contraction in its lattice size compared to BSCF while the shift of the diffraction pattern of BSCFC to a lower diffraction angle confirms an expansion in its lattice size[149]. This observed contraction and expansion in the lattice of BSCF could be attributed to the smaller ionic radius of F^- (1.33 Å) and larger ionic radius of Cl^- (1.81 Å) compared with O^{2-} (1.40 Å)[150, 151]. This observed phenomenon was also corroborated with the Rietveld refinements in **Figure 4.3a- c**. The lattice parameters of BSCF are a = b = c = 3.986 Å while those of BSCFF and BSCFC were 3.977 Å and 3.995 Å, respectively. Considering the reliability factors R_p (unweighted) and R_{wp} (weighted profile factors R_p) are all around 10% of these three oxides, the fitted results were very reliable, which illustrates a sound agreement between the observations in **Figure 4.3a- c** and **Figure 4.3d**.

The HR-TEM images of BSCF, BSCFF and BSCFC samples (**Figure 4.3e- g**) present the arrangement of the crystalline fringes with the corresponding d-spacing (100 lattice plane distances) estimated to be 3.987 Å, 3.976 Å, 3.997 Å, respectively, which intimately agree with the Rietveld results and the shifted direction of the diffraction peaks. The EDS mapping results

in **Figure 4.3h, i** indicate that the anion elements (F and Cl) and the other elements (Ba, Sr, Co, Fe, O) were uniformly distributed in the lattice of BSCFF and BSCFC without any obvious segregation. These results highly confirmed that the anion dopants F^- and Cl^- were well incorporated into the oxygen site of the oxide lattice as targeted through the EDTA–CA complexing sol-gel process for both BSCFF and BSCFC samples.

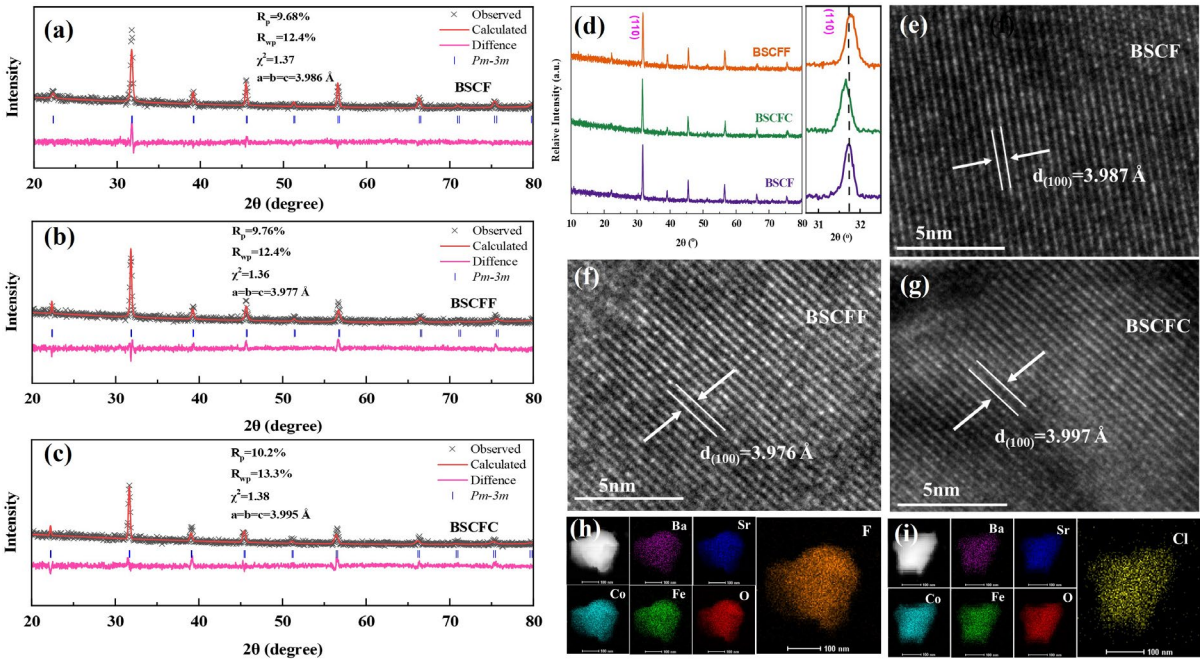

Figure 4.3 The XRD Rietveld refinement profiles of (a) BSCF, (b) BSCFF and (c) BSCFC powders; (d) RT- XRD patterns of BSCF, BSCFF and BSCFC with a local enlargement; HR-TEM images of (e) BSCF, (f) BSCFF and (g) BSCFC samples; The elements distribution of (h) BSCFF and (i) BSCFC.

4.2.2 Oxygen-related Chemical State

As the air electrode functional material of R-PCEC, the high ORR/OER catalytic activity is closely related to the intrinsic oxygen environment in the lattice structure of oxygen electrodes. Hence, the concentration of oxygen vacancies plays an important role in achieving superb ORR catalytic performance. Iodometric titration and thermo-gravimetric analysis were carried out to determine the oxygen non-stoichiometry (δ) of all the samples in room temperature and high temperature, respectively. The results depicted in **Figure 4.4a** reveal a

gradual reduction in the δ value of the BSCF oxide samples, from 0.346 to 0.319, upon successful incorporation of F^- and Cl^-. This reduction indicates a decrease in the concentration of oxygen vacancies. Such an effect is attributable to the electron-neutral rule, wherein F^- and Cl^-, with less negative charge, replace the O^{2-} site. This replacement leads to a corresponding reduction in the number of oxygen vacancies exhibiting positive charge characteristics[151-153]. Additionally, anion dopants may also occupy the site of oxygen vacancies resulting in a diminution, as shown in **Equation 4.1** by Kröger–Vink notation[151, 153, 154]:

$$SrF_2(SrCl_2) + V_O^{\cdot\cdot} \xrightarrow{SrO} Sr_{Sr}^{\times} + 2F_O^{\cdot}(2Cl_O^{\cdot}) \quad (4.1)$$

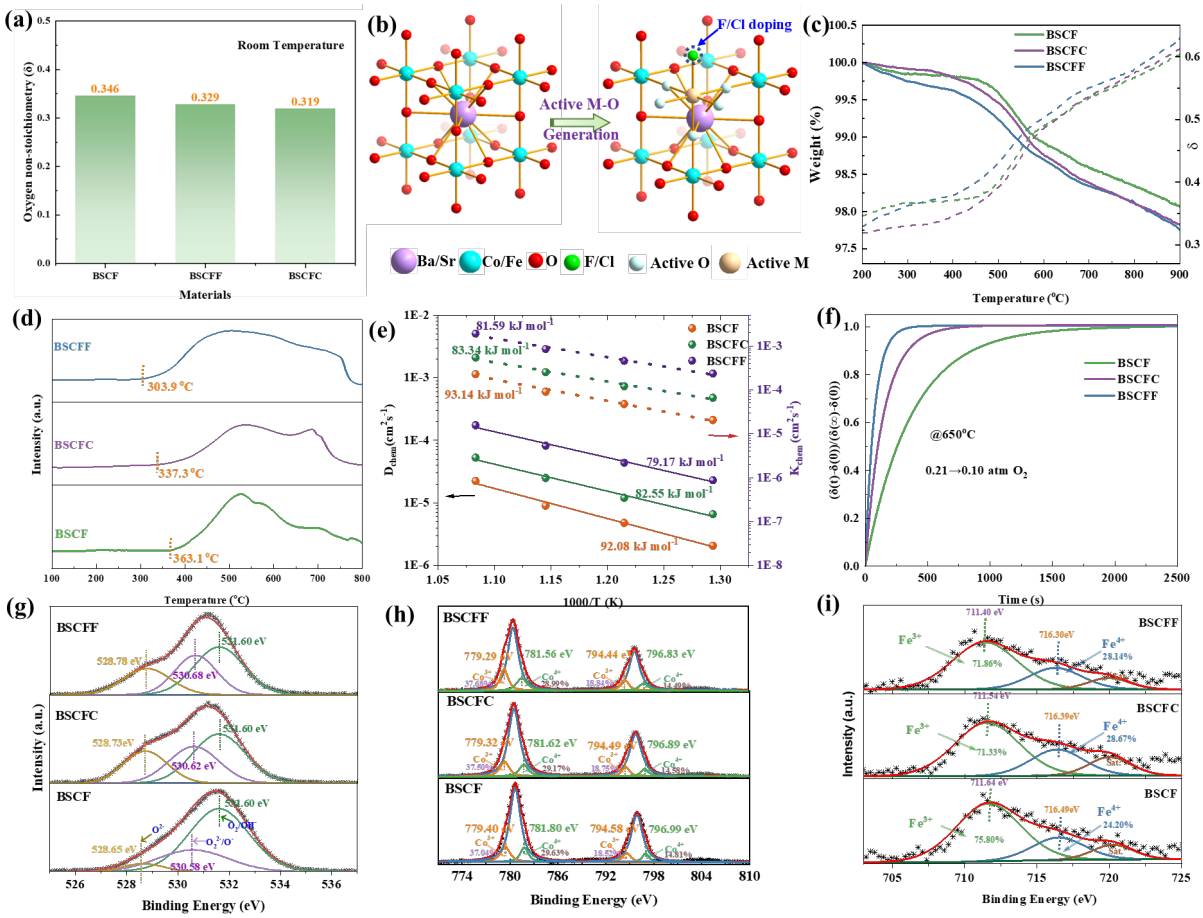

Figure 4.4 (a) The oxygen non-stoichiometry of the BSCF, BSCFF, and BSCFC samples at room temperature; (b) Schematic diagram of substituted the O site of perovskite oxide with F/Cl and generate highly active metal-oxygen bonds; (c) recorded TGA profiles under dry air; (d) O_2-TPD curves in the temperature range of 100 to 800 °C; (e) the comparison of fitted D_{chem} and k_{chem} values at various elevated temperatures; (f) the fitting ECR response curves at 650 °C; the XPS spectra of (g) O-1s, (h) Co 2p (yellow and green lines) and Ba 3d (blue lines); and

(i) Fe 2p (green and blue lines).

Figure 4.4b exemplifies the mechanism of O site substitution in perovskite oxides with F/Cl in the lattice structure to achieve a highly active M-O bonds[147]. The TGA curves presented in **Figure 4.4c** demonstrate that the weight loss of BSCFF and BSCFC was greater than that of BSCF within the elevated temperature range of 200 ºC to 900 ºC (solid line). This indicates that approximately 10% more lattice oxygen is removed due to the anion doping, with an increase from 1.94% to 2.18% and 2.25% for Cl^- and F^- doping, respectively. Moreover, by combining iodometric titration and TGA analysis, the theoretically calculated oxygen non-stoichiometry of the three samples (dotted line) revealed that BSCFF exhibited the highest oxygen vacancies value at high temperature, although it was lower than that of the BSCF samples at room temperature. Similarly, BSCFC displayed a similar trend, indicating that the lattice oxygen in BSCFF/BSCFC was highly active at high temperature, which is beneficial for oxygen absorption and O^{2-} generation and transport processes, leading to enhanced ORR catalytic activity[155]. This is further supported by the O_2-TPD profiles of the three samples presented in **Figure 4.4d**, wherein the initial desorption temperature of BSCF decreased from 363.1 ºC to 337.3 ºC for BSCFC and 303.9 ºC for BSCFF. The lower temperatures of oxygen desorption are usually attributed to the valence change from tetravalent (Co^{4+}) to trivalent (Co^{3+})[156], suggesting that the reduction of B-site transition metal ions was promoted, and oxygen vacancy generation was much easier. These results preliminarily indicate that the metal-oxygen bond was in a more activated state after anion doping, which contributed to the acceleration of the ORR/OER of R-PCECs air electrodes.

The oxygen evolution kinetics were evaluated using ECR measurements, by normalizing conductivity relaxation curves at different temperatures when the oxygen partial pressure was

suddenly changed from 0.21 to 0.1 atm. These ECR response profiles provided important indicators associated with the chemical surface oxygen exchange and diffusion characteristics for BSCF, BSCFF, and BSCFC samples. Specific D_{chem} and k_{chem} values were fitted (**Figure 4.4e**) to investigate the effect of F^-/Cl^- incorporation. After the successful incorporation of F/Cl in the O site of BSCF, the relaxation time was significantly reduced, as seen in **Figure 4.4f**. For instance, the relaxation time is decreased from 1911 s for BSCF to 341 s for BSCFF and 706 s for BSCFC. This dramatic decrease indicated the acceleration of the surface exchange and bulk transport process of oxygen after doping[44, 157]. Furthermore, the higher value of D_{chem} and k_{chem} for BSCFF and BSCFC than that of BSCF confirmed this result. The specific D_{chem} and k_{chem} values for BSCF were found to be 2.24×10^{-5} cm^2 s^{-1} and 2.28×10^{-4} cm s^{-1} at 650 °C, respectively, which were close to the literature values[154]. The corresponding values for BSCFC and BSCFF were found to be significantly improved, at 5.31×10^{-5} cm^2 s^{-1} and 5.40×10^{-4} cm s^{-1} (more than doubled) for Cl doping, and 17.4×10^{-5} cm^2 s^{-1} and 19.1×10^{-4} cm s^{-1} for F doping. Additionally, the lower activation energy value for BSCFF (79.17 kJ mol^{-1}, 81.59 kJ mol^{-1}) and BSCFC (82.55 kJ mol^{-1}, 83.34 kJ mol^{-1}) compared with BSCF (92.08 kJ mol^{-1}, 93.14 kJ mol^{-1}) confirmed that the generation and surface transport of O-ions were prompted after doping. The faster surface exchange and bulk diffusion steps of oxygen are beneficial for the typical ORR/OER processes[45, 143].

In general, the results (more oxygen vacancies generated at high temperature, lower desorption temperature and significantly improved D_{chem} and k_{chem} values) indicated that the oxygen involved activities, such as the oxygen surface exchange and bulk oxygen transport processes, were significantly accelerated after doping on the O-sites of BSCF, thus exhibiting

enhanced ORR/OER catalytic performance. These changes were most likely resulted from the altered O chemical environment and/or metal ions coordinated with it in the sample due to the dopant substitution at the O site of the perovskite[146, 152, 154, 158]. To gain further insights into the variability, XPS characterization was performed on the samples. As seen in **Figure 4.4g**, the binding energies of the lattice oxygen were 528.65 eV, 528.73 eV and 528.78 eV for BSCF. BSCFC and BSCFF, respectively. This increase could be attributed to the fact that F^- or Cl^- inclusion reduce the valence electron density of O^{2-}, weakening the chemical bonds between A- or B-site metal cations and oxygen ions, and making the lattice oxygen more active, which kept in line with the TGA and O_2-TPD results in this work and other reported results[158, 159]. Moreover, the chemical states and concentration of oxygen and B-site transition metals in these three samples have also undergone corresponding changes, as shown in **Figure 4.4h, i**, further indicating the presence of distinct chemical environments within the changed samples. For instance, electronic structure information of Co/Fe ions indicated that the binding energy value of Co ions (both Co^{4+}/Fe^{4+} and Co^{3+}/Fe^{3+}) for BSCF was higher than that for BSCFC and BSCFF, which further demonstrated that the Coulombic force between B site metal cations and oxygen anions were weakened, and consequently, oxygen migration inside the bulk oxide as well as the oxygen transfer kinetics in the oxide surface would be accelerated[152, 154, 158]. This explains, at least in part, the improvement of D_{chem} and k_{chem} values of the F/Cl doped BSCF air electrode. Notably, F-doping had a more obvious lifting effect compared with Cl-doping due to the difference in electronegativity property between anionic dopants and oxygen[148]. The incorporation of F (χ=3.98) has higher electronegativity than oxygen (χ=3.44), while the other Cl (χ=3.16) is less electronegative, leading to a stronger ability of F^- to attract bonding

electrons and increase the polarity of the metal-oxygen chemical bonds[150, 159]. This can be verified by the lowest binding energy of Co and the peak binding energy of oxygen for BSCFF. Therefore, the BSCFF air electrode exhibits a more active oxygen chemical environment with more efficient oxygen transport path and increased oxygen migration rate[148, 152].

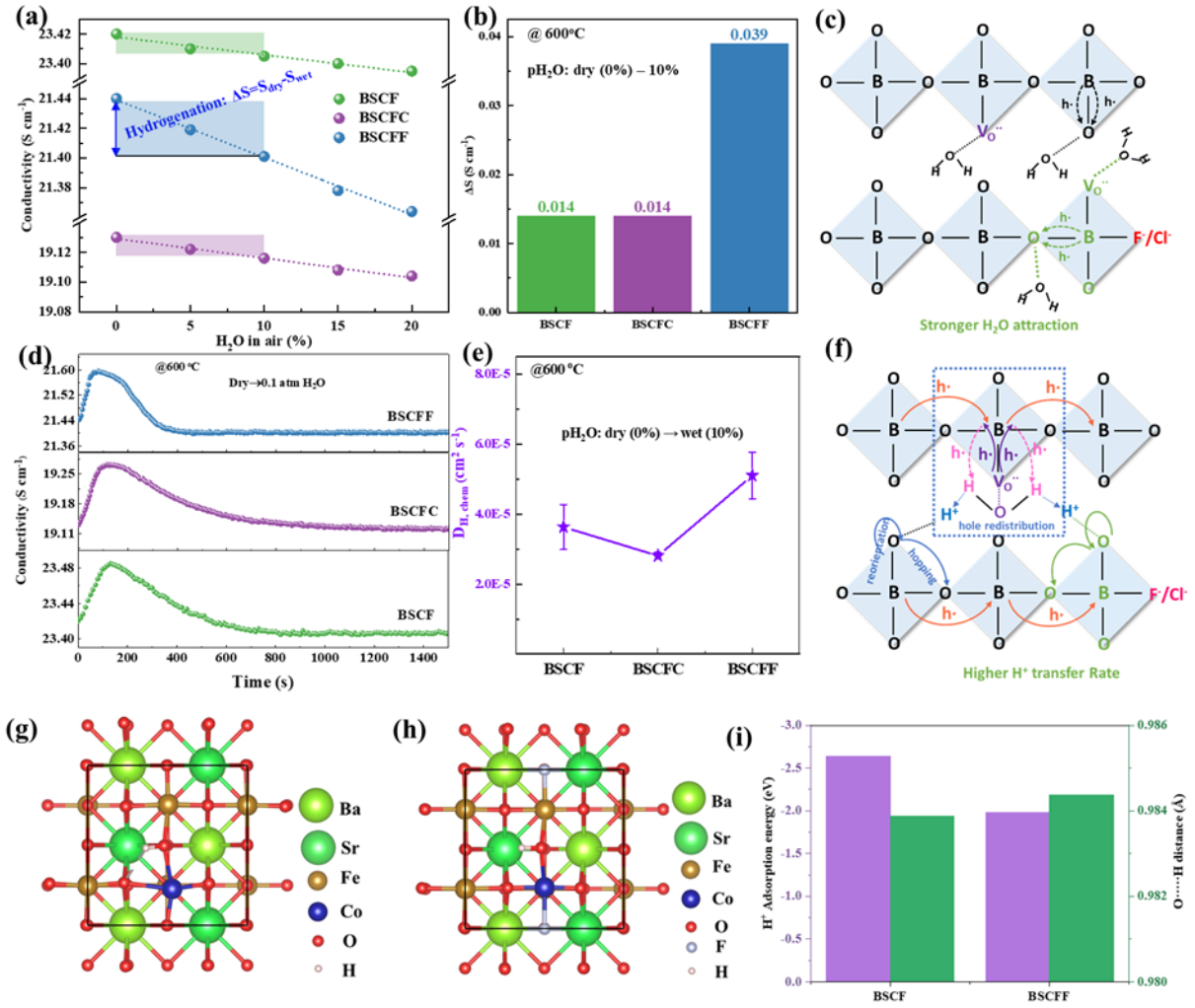

Figure 4.5 Proton generation and mobility for BSCF, BSCFC and BSCFF samples: (a) the different conductivity at various H_2O partial pressure at 600 °C; (b) the delta conductivity values (pH_2O: dry→10%) for three samples; (d) the typical ECR respond profiles and (e) the comparison of fitted $D_{H,\,chem}$ values shown in **Figure 4.5d**; schematic diagrams of (c) strong H_2O attraction and (f) higher H^+ migration properties of designed samples; Schematic illustration of H^+ on Fe-O-Co in (g) parent BSCF and (h) BSCFF cell; (i) the O···H formation energy and distance comparison for BSCF(F) samples.

4.2.3 Proton-related Chemical State

Excellent proton uptake and conduction capabilities are critical for oxide-based R-PCECs

air electrode materials to attain favorable ORR/OER catalytic performance.

For the P-type conductor of BSCF based air electrodes, which contains abundant oxygen vacancies and electron holes ($h^{\cdot}$), the intervention of protons is mainly through two forms of hydration reaction (**Equation 2.16**) and hydrogenation reaction (**Equation 2.17**). As reported before[160], it appears that the hydrogenation reaction is the main mechanism of proton uptake in p-type conductors. According to this mechanism, the proton incorporation process is spontaneous when the oxide material contains an abundance of holes, which act as sources to facilitate the conduction during the process, which can be confirmed by theories and previous research results[143, 144, 160, 161]. However, it should be noted that this reaction generates proton defects ($OH_O^{\cdot}$) at the cost of electron holes, which can result in a significant decrease in conductivity. Therefore, changes in electrical conductivity can reflect the hydrogenation reactivity of the sample in a humid atmosphere. To investigate the proton uptake properties of different cathodes, the conductivity of three bar samples (BSCF, BSCFC, and BSCFF) was tested at various H_2O partial pressures in air at 600 °C (**Figure 4.5a**). The results showed that the electrical conductivity of all samples decreased significantly with increasing water partial pressure in the atmosphere, providing further evidence that proton absorption in BSCF-based air electrode is carried out may through the hydrogenation reaction. Furthermore, it can be tentatively concluded that the decrease in conductivity values for the three samples suggests that, compared with the BSCF and BSCFC test samples, the conductivity reduction of BSCFF is more pronounced. To better illustrate this change, the difference in conductivity between dry air and air containing 10% water (ΔS) was selected for comparison (**Figure 4.5b**). It is evident that the ΔS value of BSCF and BSCFC is 0.014 S cm^{-1}, while that of BSCFF increases

significantly to 0.039 S cm^{-1} under the same conditions, indicating that BSCFF has a strikingly improved proton absorption capacity, producing more proton defects. This may be due to the introduction of strong electron affinity of fluorine that enhances the basicity of the anions in the perovskite lattice, and this active oxygen chemical environment is favorable for the adsorption of water in the surrounding environment, thus showing enhanced hydrogenation[37, 158]. In addition, as shown in **Figure 4.5c**, the hydrogenation reaction may happen in the humid atmosphere accompanied by hydration reaction which consumed the oxygen vacancies to attach H_2O and produced proton defects accordingly. As mentioned earlier, the higher concentration of $V_O^{\cdot\cdot}$, which are the H_2O absorption sites of hydration, always have lower hydration energy, indicating that it is more favorable for the formation of protonic defects in fluorinated perovskites. It is worth emphasizing that the stronger H_2O attraction ability facilitates the progress of ORR/OER.

Beyond the stronger proton uptake ability, the fast proton mobility is another particularly vital indictor for the choice of oxygen electrodes. Considering that the proton conductivity in the air electrode material is several orders of magnitude lower than the electron conductivity, it is difficult to accurately separate the proton conductivity from the total conductivity. Herein, a prudent ECR repones method through uplifting the H_2O partial pressure in testing atmosphere was applied to determine the values of chemical diffusion coefficient ($D_{H,chem}$) of proton to assess the migration of the protons[162]. This is a feasible way to unravel the bulk diffusion of H^+ in air electrodes by solving the Fick diffusion equations based on the mechanism that all carriers (oxygen vacancies, holes, and proton defects) will be redistributed when introducing more water in operational environment. As shown in **Figure 4.5d**, when the water partial

pressure is switched from 0 atm to 0.1 atm at 600 °C, the electrical conductance of the BSCF sample first experienced a short period of rising, and then subsequently decreased until reaching a steady state, similar curve trends were also observed for BSCFF and BSCFC samples. These interesting non-monotonic relaxation curves can be explained by the phenomenon that the holes would redistribute accompanied by the proton transfer step (**Figure 4.5f**)[37, 162]. During hydration or hydrogeneration process, the active O incorporation and bulk diffusion processes would generate holes, as shown in **Equation 4.2**, while the H is converted to H^+ by consuming a hole shown in **Equation 4.3**. This means that the active oxygen transport process in the sample would produce more electron holes and lead to an increase in conductivity, while the active hydrogen transport process would consume electron defects and lead to a decrease in conductivity. During the ECR response process, oxygen bulk diffusion and proton transport processes took place simultaneously, these two opposite effects on hole concentration led to a non-monotonic variation in the conductivity when the atmosphere is suddenly shifted, and similar results are also observed in the BCFZY, BSCFP0.05 and $Sr_2Fe_{1.5}Mo_{0.4}Zr_{0.1}O_{6-\delta}$ air electrodes[143, 144, 162].

$$O^* + V_O^{\cdot\cdot} \rightarrow O_O^{\times} + 2\,h^{\cdot} \quad (4.2)$$

$$OH_O^* + h^{\cdot} \rightarrow OH_O^{\cdot} \quad (4.3)$$

Based on various ECR profiles showing conductivity variation as a function of elapsed time with increasing pH_2O, different parameters of $D_{H,chem}$ were determined and summarized in **Figure 4.5e**. It can be clearly observed that BSCFF sample exhibited the highest $D_{H,chem}$ value, which was 5.11×10^{-5} cm^2 s^{-1}, while that of BSCF sample was only 3.64×10^{-5} cm^2 s^{-1} under the same conditions, and it was even a little lower for the BSCFC sample. Such a

noticeable improvement of $D_{H,chem}$ manifested that the fluorinating BSCF perovskite oxide was an efficient way to enable more rapid proton bulk diffusion process This may be explained from several conveniences: Initially, owing to the increased electronegativity of fluorine, it manifests a heightened affinity for bonding electrons, resulting in a notable reduction in the electronic density surrounding adjacent oxygen atoms, thereby weakening the O···H interaction. Furthermore, as illustrated in **Figure 4.5g- i**, the BSCFF sample exhibits a higher positive formation energy for O···H chemical bonds when compared to the BSCF sample, as determined through DFT calculations. This discrepancy implies that protons form a more robust attachment to oxygen in the BSCF configuration compared to BSCFF, resulting in a hard hopping process based on the Grotthus mechanism. Additionally, extended O···H distances were also observed in fluorinated oxides, further underscoring the propensity for the disruption of O···H bonds. In essence, the fluorinated system would require a lower energy barrier for the displacement of protons from M-OH to an adjacent position [163]. Secondly, the introduction of F element causes a certain degree of lattice contraction, which shortens the O-O bonds distance along the intra-octahedron direction correspondingly. As previously noted, the O-O bond distance is exactly the proton hopping gap from one oxygen site to another neighboring oxygen ion site. Thus, the decreased hopping distance, meaning lower energy consumption, can accelerate the proton conduction, as the activation energy of proton transport is related not only to the proton reorientation energy but also to the proton hopping energy. From this point of view, the introduction of Cl element is unfavorable to proton hopping process. Finally, the activation energy for proton conduction typically decreases with higher radius of B-site elements since the larger acceptor helps in tilting the octahedra[164]. And the B-site metal

ions in BSCFF have significantly more Co^{3+} (0.61 Å) ions with larger radius than Co^{4+} (0.53 Å), which is also beneficial to the proton transport process. Combined with these factors which indexed a lower energy barrier and higher proton transfer property, it is foreseeable that the fluorinated BSCF shows greatly improved proton chemical diffusion coefficient.

4.2.4 The Electrochemical Performance

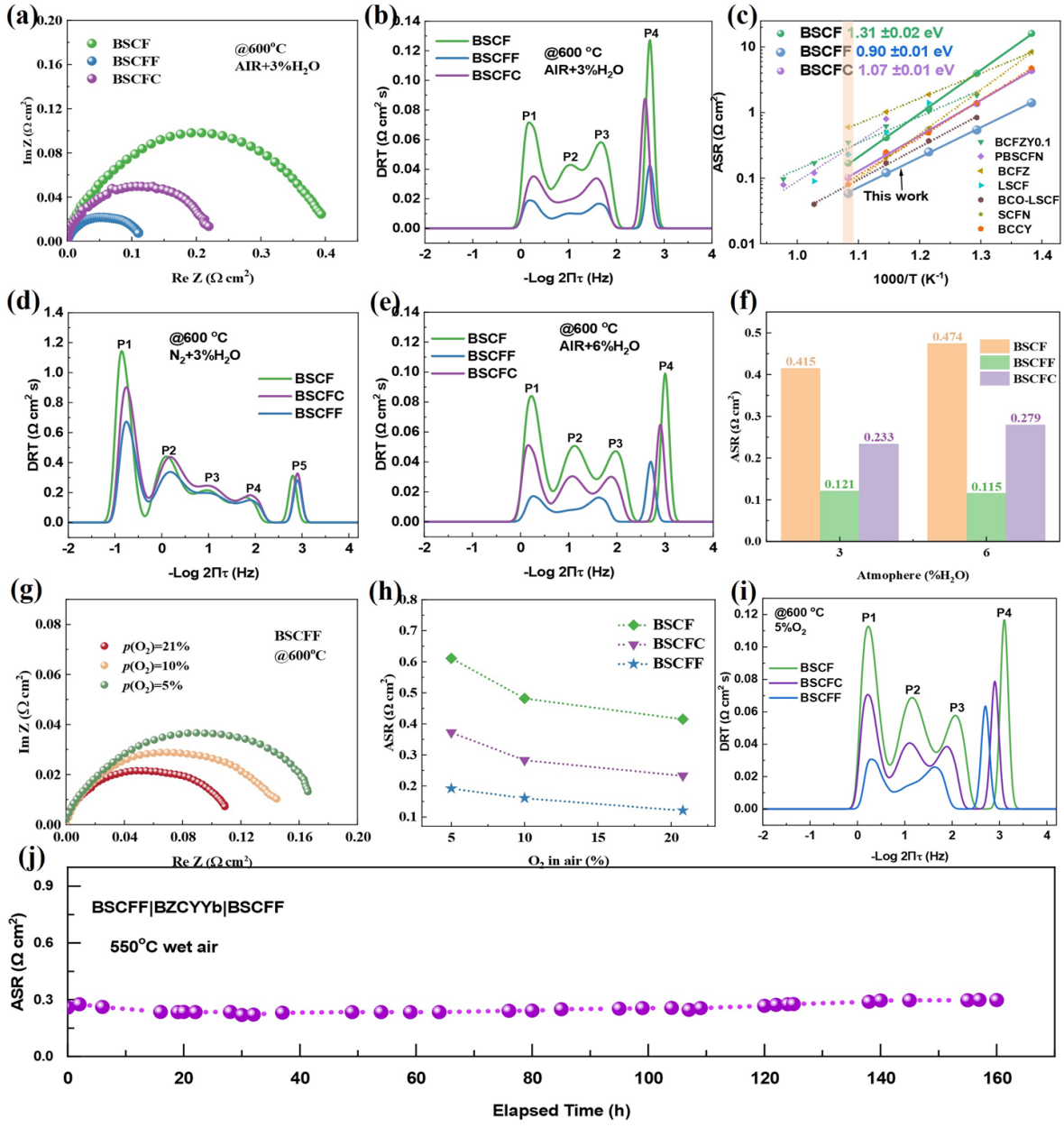

Figure 4.6 The electrocatalytic activity of three samples: (a) the typical Nyquist plots of symmetrical cells at 600 °C in wet air; (b) the corresponding DRT analysis; (c) Arrhenius plots in wet air; the DRT results in (d) wet N_2 and (e) 6%H_2O-air atmospheres; (f) the summarized

ASR values at different H_2O partial pressure in air; (g) the Nyquist plots of BSCFF in different oxygen partial pressure; (h) the summarized ASR values variation with various O_2 content; (i) the DRT results in 5%O_2+95%N_2; (j) the long-term stability of symmetrical cell with the BSCFF electrodes.

The electrocatalytic performance of three electrodes were assessed in the BZCYYb proton-conducting electrolyte supported symmetrical cells with BSCF, BSCFC and BSCFF air electrodes between 450 ºC and 650 ºC. EIS was used to compare the typical Nyquist plots in humid air at 600 °C, as shown in **Figure 4.6a**. The BSCFF electrode showed the lowest ASR value of only 0.12 Ω cm^2, whereas those of BSCF and BSCFC were 0.41 Ω cm^2 and 0.23 Ω cm^2, respectively.

To gain further insight into this noticeable improvement, the DRT technology was applied by deconvoluting the corresponding EIS data to discriminate against a train of overlapping electrode processes (**Figure 4.6b**). Four characteristic peaks were observed in the DRT plots, denoted as three different segments according to the located frequency range: low frequency P1 (LF, <10 Hz), intermediate frequency P2 and P3 (IF, 10-10^3 Hz), and high frequency P4 (HF, >10^3 Hz). Specifically, referring to previously reported DRT analysis results and their corresponding peak patterns related to R-PCEC air electrode[88, 143, 165], as well as the actual ORR and OER processes, these can be assigned to the electrochemical processes of gas (O_2/steam) conversion (P1), ions (H^+/O^{2-}) transfer at the electrode bulk (P2 & P3), and ions/charge transfer from the electrolyte to the electrode at the triple-phase boundaries (P4) [133, 166]. **Figure 4.6b** showed that all characteristic peak areas for BSCFF(C) reduced compared to the pristine BSCF electrode, indicating that almost all interconnected sub-processes were accelerated during the cathode electrochemical reaction. Therefore, it exhibited a lower resistance for the whole oxygen reduction reaction.

In addition, the Arrhenius plots of the ASR values as a function of temperatures were summarized and used to compared with other high-performance cathodes based on BZCYYb electrolyte supported symmetrical cells in wet air, such as $BaCo_{0.4}Fe_{0.4}Zr_{0.1}Y_{0.1}O_{3-\delta}$ (BCFZY) , $PrBaCo_{1.6}Fe_{0.2}Nb_{0.2}O_{5+\delta}$ (PBCFN) , $BaCo_{0.4}Fe_{0.4}Zr_{0.2}O_{3-\delta}$ (BCFZ) , $La_{0.6}Sr_{0.4}Co_{0.2}Fe_{0.8}O_{3-\delta}$ (LSCF) , barium cobaltite (BCO) coated LSCF , $Sr_{0.9}Ce_{0.1}Fe_{0.8}Ni_{0.2}O_{3-\delta}$ (SCFN) , and self-assembled $BaCo_{0.7}(Ce_{0.8}Y_{0.2})_{0.3}O_{3-\delta}$ (BCCY) (**Figure 4.6c**). The BSCFF cathode still exhibited the smallest ASR value, and its Ea value was also significantly reduced in comparison with other air electrodes, at only 0.90 eV. Therefore, it may be more conducive to the low-temperature operation. These results preliminarily confirmed that a small amount of anion doping in BSCF perovskite was an effective way to improve the catalytic performance of R-PCEC air electrode, and the introduction of F had a more significant effect on improving the electrode performance than Cl due to the higher-level enhanced oxygen and proton involved electrochemical reaction processes.

To further analyze the proton uptake and transport capabilities of the three electrodes in a humid atmosphere, the ASRs and DRT (**Figure 4.6d**) plots were carried out in humid nitrogen, eliminating the influence of O^2 diffusion, oxygen-related surface exchange, and O^{2-} transfer processes[167]. The DRT analysis results showed that the enhancement of fluorinated BSCF can be attributed to faster H_2O conversion (P1) and proton transfer (P2-P4) sub-steps, which consist with the stronger water attraction and protons transfer ability mentioned in **Figure 4.5**. Moreover, when the water partial pressure is increased to 6% H_2O in air, the resistance of these samples (**Figure 4.6f**) showed a different trend. Both the impedance BSCFC and BSCF grew with amplitudes of 0.046 Ω cm^2 and 0.059 Ω cm^2, respectively, while that of BSCFF decreased

from 0.121 Ω cm^2 to 0.115 Ω cm^2, which might be due to the different proton conductivity of these samples[168]. From the Nyquist plots and corresponding DRT analysis results (**Figure 4.6e**), it was because the remarkable accelerated water diffusion and consumption processes so that the ORR was progressively enhanced even in higher water content and lower oxygen levels[168]. This illustrated that outstanding formation and transfer of hydroxide defects of the BSCFF triple conducting oxide are highly valuable.

At the same time, to further investigate the influence of the oxygen concentration on the reaction kinetics of different electrodes, we collected the EIS data (**Figure 4.6g**) of these symmetrical cells in the different oxygen partial pressure and performed the DRT analysis (**Figure 4.6i**). As expected, the ASR values for all electrodes increased abruptly with decreasing oxygen partial pressure. And according to the corresponding DRT diagram, the reduction of the oxygen partial pressure leads to a significant slowdown of each step reaction process, especially the low-frequency (P1) associated with gas (O_2) diffusion process and the intermediate-frequency (P2, P3) related to oxygen surface exchange activation and bulk phase transport process. However, as the comparison of ASR values (**Figure 4.6h**) for these samples and the corresponding DRT results shown, the fluorinated BSCF still exhibited the lowest resistance when the oxygen content reduced to only 5%, indicating that BSCFF electrode has the strongest ability to utilize oxygen to participate in the ORR, which is benefited from its abundant concentration of oxygen vacancies and weaker metal-O bonds[43, 152].

To gain more understanding of the electrochemical reaction kinetics of the BSCFF air electrode, the corresponding EIS curves and DRT plots under different water partial pressure (pH_2O) and oxygen partial pressure (pO_2) were applied to further demonstrate the elementary

sub-step involved in the whole electrode reactions. As shown in **Figure 4.7a, b**, the ASR values were lower in higher pH_2O and pO_2, which further indicates the excellent proton and oxygen conduction ability of the BSCFF air electrode. As observed in **Figure 4.7c**, the P4 (HF) and P3(IF) were significantly reduced with the increased pH_2O which prompts the formation and transfer of hydroxide defects[140], suggesting that the P4 and P3 might be strongly associated with the proton migration process from the electrolyte the electrode and the production of hydroxide defects at the electrode bulk. In the meantime, the P1 (LF) was slightly dropped with the increased pH_2O, suggesting the P1 correlated with the steam mass diffusion process. Moreover, the P2 shows a different change tendency, firstly declining and then increasing with the increased pH_2O. As the inlet water maybe consumes the concentration of oxygen vacancies generated in the electrode material, the higher content of steam in the testing atmosphere can lead to a detrimental effect on the oxygen transport process. Therefore, P2 can be linked with the process of oxygen transport in the electrode bulk, which can be further illustrated by the results of the various pO_2 effects on the electrode reactions displayed in **Figure 4.7d**. It can be clearly seen that all peaks reduced with the higher pO_2, which keeps consistent with some previous reports[133, 140, 143], indicating that all peaks can relate to the oxygen-involved sub-steps of electrode reactions. Combined with the location of the peaks (characteristic frequency), the P1 (LF) may correspond to the oxygen gas diffusion process; the P2 (IF) was associated with the oxygen transfer in the electrode bulk while the P3(IF) likely linked with the production of the O^{2-}; the P4 (HF) may be related with charge transfer process involved in ORR processes. In conclusion, the electrochemical processes corresponding to the characteristic peaks observed in the DRT plots keep line with the mentioned analysis results (considering both the

influence of pH_2O and pO_2).

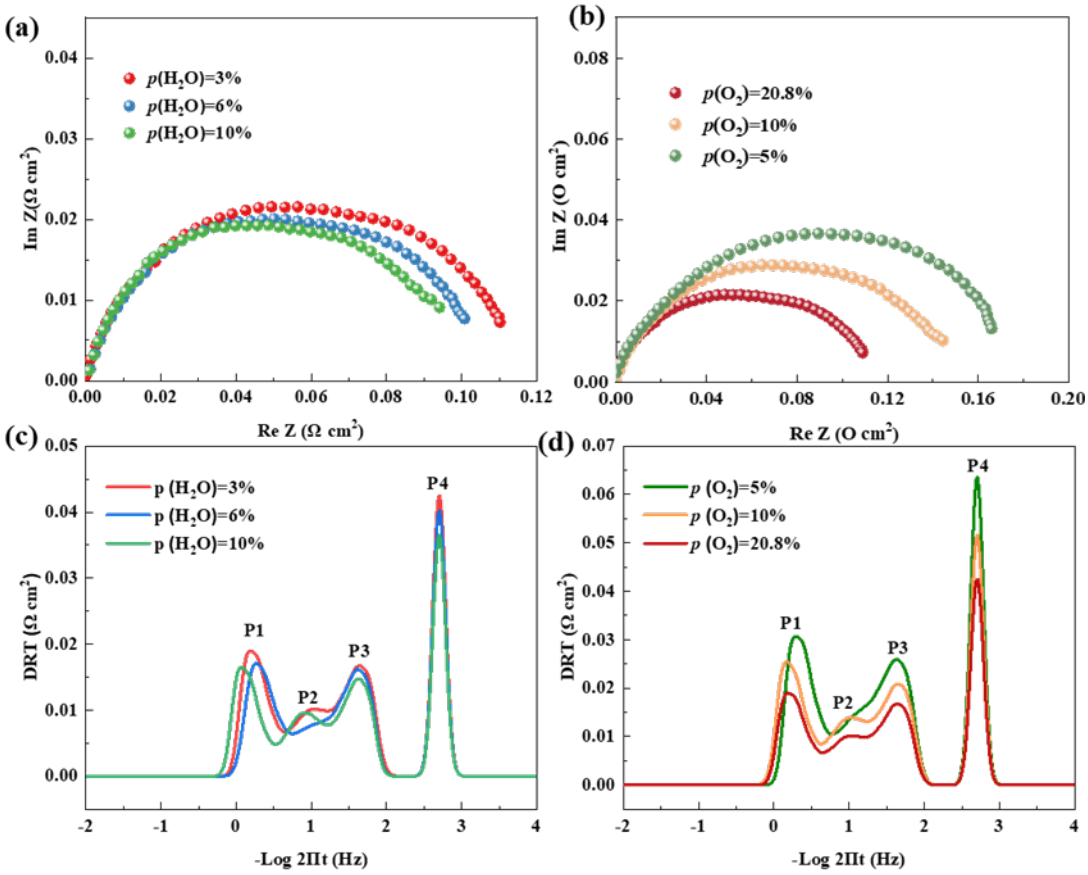

Figure 4.7 The comparison of (a, b) Nyquist plots and (c, d) DRT plots of BSCFF air electrode in different (a, c) *p*H2O and (b, d) *p*O2 atmospheres operating at 600 °C.

The EIS and DRT results all imply that BSCFF has superior electrocatalytic activity, and the excellent catalytic performance can be operated in a long time, which can be confirmed by the long-term stability of the symmetrical cell in humid air at 550 °C with a configuration of BSCFF|BZCYYb|BSCFF (**Figure 4.6j**). After 160 h of operation, the evaluated ASR values remained around 0.28 Ω cm^2 without any significant degradation, implying a remarkable stability of the BCSFF electrode on the BZCYYb proton-conducting electrolyte in water-containing atmosphere. This electrode with efficient and stable electrocatalytic activity is very suitable for use as an oxygen electrode based on proton conductor electrolyte cells.

4.2.5 Actual Electrochemical Performance in Different Modes

To verify the superior ORR catalytic performance of the BSCFF air electrode in FC mode,

the NiO-BZCYYb anode supported single cells with BSCF, BSCFC and BSCFF air electrodes were fabricated and tested. The typic i-V-p curves comparison of these cells, supplying pure H_2 and air to both sides at 650 °C, are shown in **Figure 4.8a**. It is evident that the cell with BSCFF electrode exhibited the highest peak power density (PPD) of 977 mW cm^{-2}, while the parent perovskite BSCF cathode the chlorine BSCF electrode achieved only 657 mW cm^{-2} and 770 mW cm^{-2}, respectively. Similar trends were observed in the detailed i-V-p curves recorded at 600-450 °C (**Figure 4.8b**), further confirming the superior ORR catalytic activity of the fluorine modified BSCF electrode. Remarkably, the PPDs of 668, 472, 303, 215 mW cm^{-2} were reached for BSCFF air electrode at 600, 550, 500 and 450 °C, respectively, and the corresponding open circuit voltages (OCVs) all achieved above 1.05 V, indicating the electrolyte film is dense which further illustrated by the SEM images. When compared to state-of-art air electrodes reported, such as $PrNi_{0.5}Co_{0.5}O_{3-\sigma}$ (PNC), $BaCo_{0.7}(Ce_{0.8}Y_{0.2})_{0.3}O_{3-\delta}$ (BCCY), $Sr_{0.9}Ce_{0.1}Fe_{0.8}Ni_{0.2}O_{3-\delta}$ (SCFN), $SrEu_2Fe_{1.8}Co_{0.2}O_{7-\delta}$ (SEFC), $Sr_3Fe_2O_{7-\sigma}$ (RP-SF), $(PrBa_{0.8}Ca_{0.2})_{0.95}Co_2O_{6-\delta}$ (PBCC95), $BaCe_{0.5}Fe_{0.3}Bi_{0.2}O_{3-\delta}$ (BCFBi), $BaCo_{0.4}Fe_{0.4}Zr_{0.1}Y_{0.1}O_{3-\sigma}$ (BCFZY), the electrochemical performance of the prepared PCFC based on the fluorine BSCF achieved a rarely high PPD (**Figure 4.8c**). The impressive performance can be related to the enhanced oxygen and proton kinetic rate of transport and surface diffusion so that it showed accelerated ORR catalytic activity which could be further demonstrated by the significantly lower ASR value, that were only 0.08 and 0.19 Ω cm^2 under OCV condition at 650 °C and 600 °C, respectively. To clearly highlight the operational stability of the BSCFF air electrode, the long-term durability test of this single cell under a constant current density of 0.38 A cm^{-2} at 550 °C was conducted (**Figure 4.8d**). It can be found that the cell voltage didn't show

detectable degradation and stabilized at around 0.78 V during the 60-h operation. At the same time, the inset SEM image also identified that the BSCFF air electrode had good contact with the electrolyte film without any breaks after the test, which suggested that the BSCFF air electrode and BZCYYb electrolyte film had a good thermal expansion coefficient matching and thermal stability.

Moreover, to confirm the excellent electrocatalytic activities of BSCFF air electrode in R-PCEC mode, similar single cells with different electrodes were also prepared for electrochemical reversibility measured. The i-V curves of R-PCEC with the parent BSCF air electrode and the corresponding fluorine and chlorine BSCF air electrodes were obtained by inletting the pure H_2 and 3% H_2O-air to fuel and air electrodes, respectively (**Figure 4.8e**). The assembled R-PCEC operated in FC mode had lower power output than the proton ceramic fuel cell due to the slight difference in cell preparation and the introduction of steam in the air electrode[167]. It can be clearly observed that when the reversible cells function in EC mode and the applied voltage was 1.3V for BSCFF electrode, the electrolysis current density could achieve 950, 590, 316, 190 mA cm^{-2} at 650, 600, 550 and 500 °C. The electrolysis performance was higher than those of the BSCF and BSCFC air electrodes and exceeded many reported state-of-art air electrode (**Figure 4.8g**) utilized in R-PCEC, such as $Sr_{0.9}Ce_{0.1}Fe_{0.8}Ni_{0.2}O_{3-\delta}$ (SCFN), $SrEu_2Fe_{1.8}Co_{0.2}O_{7-\delta}$ (SEFC), $SrEu_2Fe_2O_{7-\delta}$ (SEF), $La_{1.2}Sr_{0.8}NiO_4$ (LSN), $Sm_{0.5}Sr_{0.5}CoO_{3-\delta}$ (SSC), $BaGd_{0.8}La_{0.2}Co_2O_{6-\delta}$ (BGLC) , $Pr_2NiO_{4+\delta}$ (PNO). Furthermore, the electrolysis operational stability test for this cell in EC mode was carried out at 550 °C. It can be directly observed that the electrolysis performance of BSCFF kept stable without obvious degradation under a constant electrolysis current density of -295 mA cm^{-2}, which further

demonstrated the superiority of BSCFF electrode.

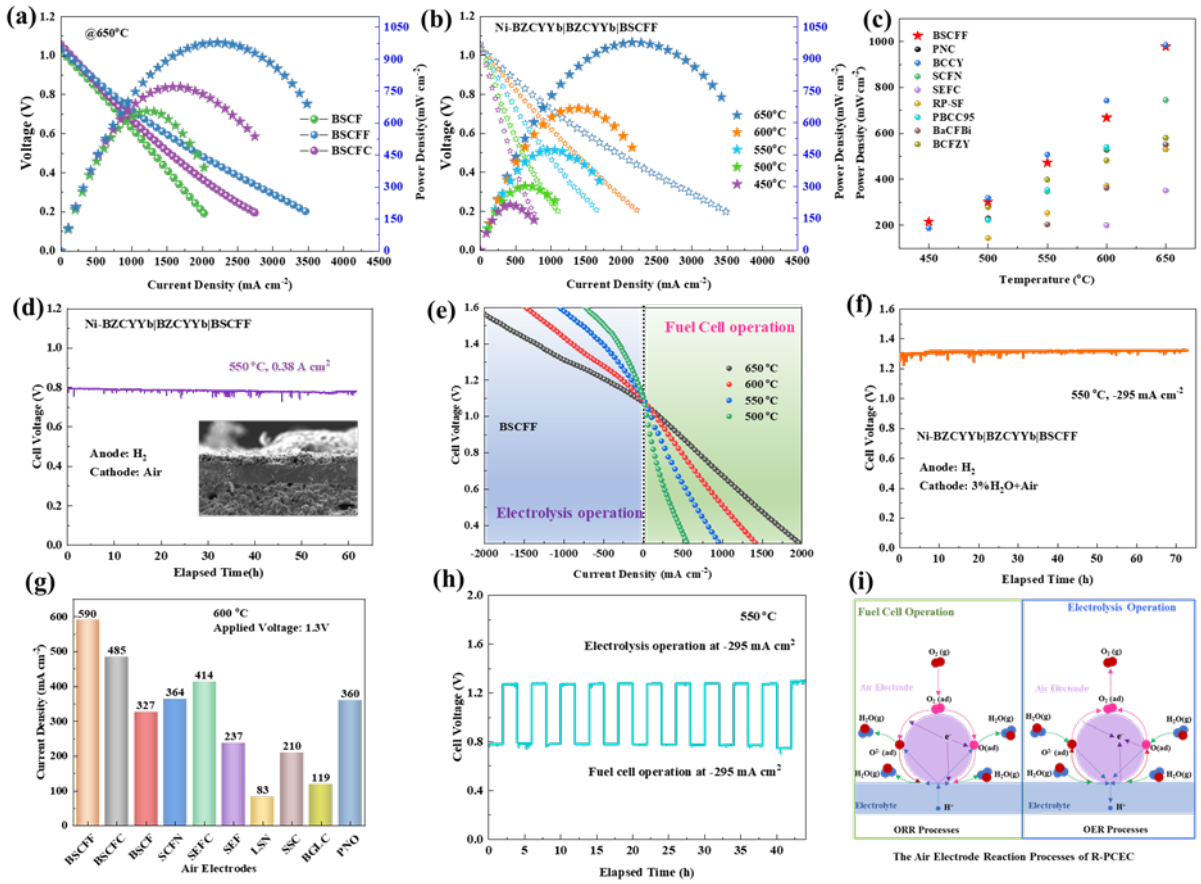

Figure 4.8 (a) The comparison of i-V-p curves for BSCF, BSCFC and BSCFF air electrodes at 650 °C; (b) the i-V-p curves for BSCFF at 450-650 °C; (c) PPDs comparison of PCFCs with different electrodes; (d) durability of the single cell at 550 °C under a current density of 0.38 A cm^{-2}; (e) the i-V curves of R-PCEC with dry H_2 and wet air (3% H_2O) as the reactant gas in both fuel cell and electrolysis operations at 500-650 °C with BSCFF electrode; (f) operating stability of R-PCEC at 550°C; (g) the current density comparison of R-PCEC at 1.3V with various air electrodes; (h) continuous R-PCEC operation, cycling between EC and FC modes at 550 °C; (i) schematic illustration of the ORR/OER processes for air electrodes.

To further confirm the feasibility of R-PCEC with this advanced BSCFF electrode, cell reversibility was also evaluated by cyclic switching between the electrolysis hydrogen production (-295 mA cm^{-2}) and power generation modes (295 mA cm^{-2}) under different current density conditions at 550 °C, and it has run stably throughout 11 reversible cycles within 44h (2h each condition) without negligible performance degradation (**Figure 4.8h**). The reliable conversion operation under different current densities strongly revealed that BSCFF air

electrode has good durability and chemical stability, as well as excellent adhesion and compatibility with the electrolyte. These results suggest that BSCFF is a potential air electrode material for R-PCEC (**Figure 4.8i**) with high activity and durability.

4.3 Conclusion

In summary, the more active oxygen chemical atmosphere was achieved by tuning the metal-oxygen bond of BSCF triple-conducting perovskite oxide via different electronegativity anions (F^-, Cl^-) doping. The chemical properties of these samples were systematically investigated, and all results revealed that an optimal F^--dopant with greater electronegativity enhanced the bulk oxygen/proton diffusion, surface oxygen exchange and proton uptake characteristics, and benefiting from these positive effects, significantly accelerated the sluggish ORR/OER kinetics of the parent BSCF air electrode, which ensuring the excellent electrochemical performance of the BSCFF catalyst in both FC and EC modes. The PPD of the single cell working in FC mode reached 977 mW cm^{-2} at 650 ^oC, and the current density of the EC mode reached 950 mA cm^{-2} at applied voltage of 1.3V. The cycle operation of power generation and hydrogen production under different current densities was further demonstrated the high adaptability and durability of the BSCFF catalyst assembled as the R-PCEC air electrode. This approach, modulating the chemical bonding interactions based on anions-doping in perovskite cathodes, offers a rational design for functional material to improve electrochemical performance of energy storage and conversion devices based on proton conductors, and has significance for the exploration of catalysts in other electrochemical systems.

CHAPTER 5 Dual-Anion Engineering Coupled with In Situ Exsolution for Simultaneous Bulk and Surface Modification

5.1 Introduction

Currently, as a typic TCO widely applied in proton-conducting fuel cells, BCFZY is regarded as a benchmark air electrode material since it possesses convincing ORR catalytic activity in ambient air[169]. Unfortunately, when it directly employed as the air electrode for R-PCECs, like most TCO electrode materials, the ORR catalytic activity significantly diminishes due to the impede oxygen ion/proton formation and transport capabilities, particularly in humid conditions, leading to hindering OER catalytic activity as well[139]. Given this fact, extensive efforts have been devoted to finding effective technologies to enhance air electrodes with high triple-conduction properties. Recent findings have affirmed the efficacy of partial substitution at the A-site of single-phase perovskite materials. A specific instance of this approach involved the partial potassium (K) doping at the A-site to create $Ba_{0.9}K_{0.1}Co_{0.4}Fe_{0.4}Zr_{0.2}O_{3-\delta}$[170], $Ba_{0.4}K_{0.1}Sr_{0.5}Co_{0.8}Fe_{0.2}O_{3-\delta}$[142], and $Sr_{1.75}K_{0.25}Fe_{1.5}Mo_{0.5}O_{6-\delta}$[171] air electrodes. Additionally, a systematic exploration was conducted for different A-site element substitutions in the double perovskite material ($LnBa_{0.5}Sr_{0.5}Co_{1.5}Fe_{0.5}O_{5+\delta}$ (LnBSCF, Ln=Pr, Nd, and Gd))[172]. All modified materials showcased enhanced triple-conduction characteristics and proton absorption capacity. Furthermore, successful investigations have also validated the effectiveness of partial substitution at the B-site of single-phase TCO, exemplified by P incorporating- BSCFP0.05[143], Mg doping- $Ba(Co_{0.4}Fe_{0.4}Zr_{0.1}Y_{0.1})_{0.95}Mg_{0.05}O_{3-\delta}$[45], Ta substitution- $BaCo_{0.8}Ta_{0.2}O_{3-\delta}$[173], and Cs doping- $PrBa_{0.9}Cs_{0.1}Co_2O_{5+\delta}$[174] electrodes. Remarkably, whether the modification is carried out at the A-site or B-site of traditional TCO

air electrode materials, these methodologies are grounded in a robust theoretical framework: regulating the M-O chemical bonds within the target lattice. This optimization process enhances the Lewis acidity and defects (oxygen vacancies, proton defects) environment, leading to accelerated ion transport and generation, particularly proton conductivity. The robustness of these approaches is further corroborated by detailed DFT calculations and experimental results reported elsewhere[37, 164, 175]. Indeed, directly modulating the anions in perovskite oxides stands out as a more immediate and effective strategy for fine-tuning the M-O chemical bonds within their lattice[158]. This method not only upholds structural integrity through the support of A-site metal cations but also preserves the catalytic attributes of B-site metal cations critical for electrochemical reactions, holding significant promise for crafting catalyst materials that are both highly efficient and stable. Notably, considering the electronegativity of fluorine (χ = 3.98) surpasses that of oxygen (χ = 3.44), and the valence electron density of oxygen is lower than that of fluorine atoms, the introduction of fluorine is anticipated to mitigate the coulombic forces between B-site metallic ions and oxygen ions. Consequently, this adjustment weakens the M-O chemical bonds, thereby amplifying the generation and migration capabilities of active carriers, as confirmed by the research work in Chapter 4.

Moreover, in additional to the modification of the main phase, surface regulation has also proven to be a highly efficient method for enhancing the catalytic activity of air electrodes[176]. For instance, the incorporation of the heteroatom boron (B) onto the surface of $Pr_4Ni_3O_{10+\delta}$ through mechanical mixing has been demonstrated to enhance the concentration of surface Brønsted acid (-OH), thereby improving its surface electrocatalytic activity[90]. Additionally,

the introduction of nano-catalysts through impregnation, such as infiltrating $BaCoO_{3-\delta}$ on the LSCF surface[101], coating $Pr_{0.1}Ce_{0.9}O_{2+\delta}$ on the $PrBaCo_2O_{5+\delta}$ surface[103], and dropping an efficient catalyst $PrNi_{0.5}Co_{0.5}O_{3-\delta}$ (PNC) on the surface of $BaCe_{0.5}Pr_{0.3}Y_{0.2}O_{3-\delta}$ (BCPY)[105]. Notwithstanding these achievements, challenges include the uncontrollable appearance of the electrodes, particularly under humid conditions, and the associated time-consuming and labor-intensive preparation processes. Nowadays, a new focus in air electrode development is creating stabilized materials through in situ formations/exsolution of active nanoparticles (NPs). Illustrative examples involve the in situ formation of $Gd_xCo_yO_{3-\delta}$ NPs in a double perovskite $Ba_{0.8}Gd_{0.8-x}Pr_{0.4}Co_{2-y}O_{5+\delta}$[140], in situ exsolved $BaCoO_{3-\delta}$ nanoparticles on the surface of $PrBa_{0.8}Ca_{0.2}Co_2O_{5+\delta}$[132], in situ generation of $BaCeO_3$ and CeO_2 double phases on the surface of $PrBa_{0.8}Ca_{0.2}Fe_{1.8}Ce_{0.2}O_{6-\delta}$[165], and the surface generation of nanosized β-$NaFeO_2$ (NF) on the electrocatalytically active $Na_ySr_zTi_uFe_{1-u}O_{3-\delta}$ perovskite main phase[177]. Additionally, the in-situ generation of metal oxide (MO) NPs on the electrode material surface has demonstrated enhanced surface reaction activity. Critically, these nanoparticles resist reverting to the main phase structure under oxidative conditions, thereby avoiding the loss of catalytic activity, notable examples include NiO nanoparticles[178, 179].

Herein, we propose a novel strategy of concurrent introduction of nickel (Ni) ions with highly catalytic active and fluorine (F) ions with greater electronegativity into both the B-site and O-site of the parent BCFZY perovskite oxide to simultaneously enhance the bulk ionic transport and surface electrochemical catalytic active sites of air electrode materials. Benefiting from both the weakened M-O bonds in the bulk phase and the heightened catalytic active sites of surface nano-particles MO, the modified air electrode exhibits high-efficiency bulk O^{2-}/H^+

transport paths and significantly improved rates of O^{2-}/H^{+} migration, along with enhanced surface exchange kinetics. Therefore, the designed air electrode nanocomposite $Ba(Co_{0.4}Fe_{0.4}Zr_{0.1}Y_{0.1})_{0.95}Ni_{0.05}F_{0.1}O_{2.9-\delta}$ (N-BCFZYNF) presents a superior ORR/OER catalytic activity in R-PCECs, providing a rational avenue for improving the high-performance R-PCECs electrodes with favorable operational stability.

5.2 Results and Discussion

5.2.1 Bulk and Surface Microstructures

Herein, the cationic Ni^{2+} and anionic F^{-} were incorporated into the BCFZY perovskite lattice through the introduction of nickel nitrate ($Ni(NO_3)_2 \cdot 6H_2O$) and barium fluoride (BaF_2) compounds, respectively. Notably, the positively high value of Gibbs free energy of BaF_2 ensures that F does not loss during the high-temperature sintering process[162], which confirms the possibility of successfully incorporation of F^{-} and Ni^{2+} at the same time. To identify the effect of these introduced different ions substituted into the B-site and O-site of BCFZY, the room temperature XRD patterns of the parent BCFZY and the targeted N-BCFZYNF powders were observed, as shown in **Figure 5.1a**. The as-obtained BCFZY was found to show a single-phase perovskite structure without impurity phase, while the synthesized N-BCFZYNF sample exhibited a major perovskite phase and a minor NiO phase. This phenomenon may be attributed to the introduction of fluorine with a higher electronegativity, resulting in the weakening of the metal-oxygen bonds within the modified material lattice. This facilitates the selective precipitation of Ni-O (with lower binding energy) from the parent material during the high-temperature treatment process[180, 181]. Additionally, the higher diffraction angle of N-BCFZYNF can be found in the enlargement XRD patterns from 36 ° to 45 °, indicating a

contraction in its lattice size compared to the BCFZY-based lattice. Considering the larger ionic radius of Ni^{2+} (0.69 Å) in comparison to other B-site metal ions in the host perovskite lattice, coupled with the fact that F^- (1.33 Å) possess a smaller size than O^{2-} (1.40 Å)[45, 158], it is highly plausible that, during the synthesis process, fluorine has successfully incorporated into the lattice, while nickel may have been either limited or absent from lattice incorporation. This observation partially accounts for the formation of a minor quantity of NiO phase for the N-BCFZYNF sample. Additionally, the Rietveld refinement of XRD data of modified N-BCFZYNF sample was conducted to further determine the degree of nickel exsolution, as presented **Figure 5.1b**. A visual representation of the NiO content could be found and estimated at 1.19%, implying that a significant portion of Ni precipitates from the host phase. Moreover, as compared with the corresponding Rietveld result of parent BCFZY, the N-BCFZYNF oxide exhibited a smaller lattice size while both samples show a cubic structure with space group Pm-3m, which further keeps in line with the XRD patterns exhibited in **Figure 5.1a**. Considering the refinement parameters such as the reliability factors R_p (unweighted) and R_{wp} (weighted profile factors R_p) are all around below 15%, the fitted results were very reliable, which illustrates a sound agreement between the observations in **Figure 5.1 a, b**.

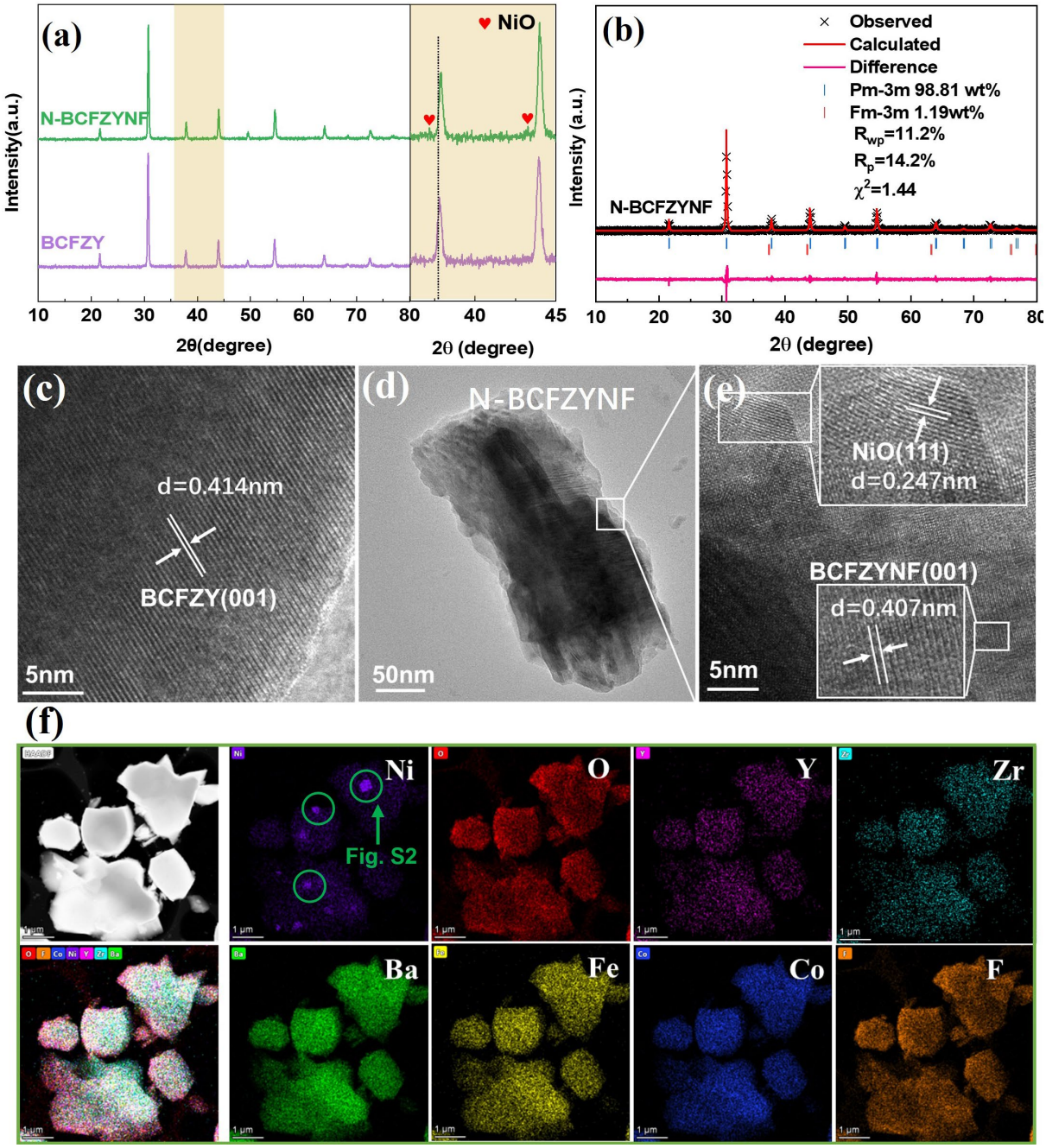

Figure 5.1 (a) The RT-XRD patterns of BCFZY and N-BCFZYNF with a partial enlargement; (b) The XRD Rietveld refinement profiles of N-BCFZYNF with two phases; HR-TEM images of (c) BCFZY, (d-e) N-BCFZYNF samples; (f) The elements distribution of N-BCFZYNF sample.

The formation of two phases oxide by introduction F^- and Ni^{2+} at anion and cation sites simultaneously was further supported by HR-TEM images as shown in **Figure 5.1c- e**. The crystalline fringes with the corresponding d-spacing (001 lattice plane) were estimated to be 4.14 Å for BCFZY sample (**Figure 5.1c**). However, the same d-spacing value for N-BCFZYNF

sample was determined to be 4.07 Å (**Figure 5.1e**) through the enlargement part of the particle shown in **Figure 5.1d**, which intimately agree with the Rietveld results and the shifted direction of the diffraction peaks. Moreover, **Figure 5.1e** showed another diffraction planes with 0.247 nm for the 111-lattice plane of NiO, from which it is also obvious that these two phases were connected to each other very well. Meanwhile, the EDS mapping results in **Figure 5.1f** displayed that some Ni element aggregated while other metal element were distributed uniformly in the single grain, which could be found more clearly in **Figure 5.2a**. On the contrary, as shown in **Figure 5.2b**, the BCFZY sample exhibited a pure perovskite oxide, and all elements were uniformly distributed without any obvious segregation. Additionally, the anion element (F, O) also displayed the similar uniformly distribution, indicating the successfully incorporation of F into the oxygen site as targeted. These results highly demonstrated the existence of nanoscale NiO particles in the perovskite oxide and the anion dopants were well incorporated into the lattice for the designed N-BCFZYNF sample.

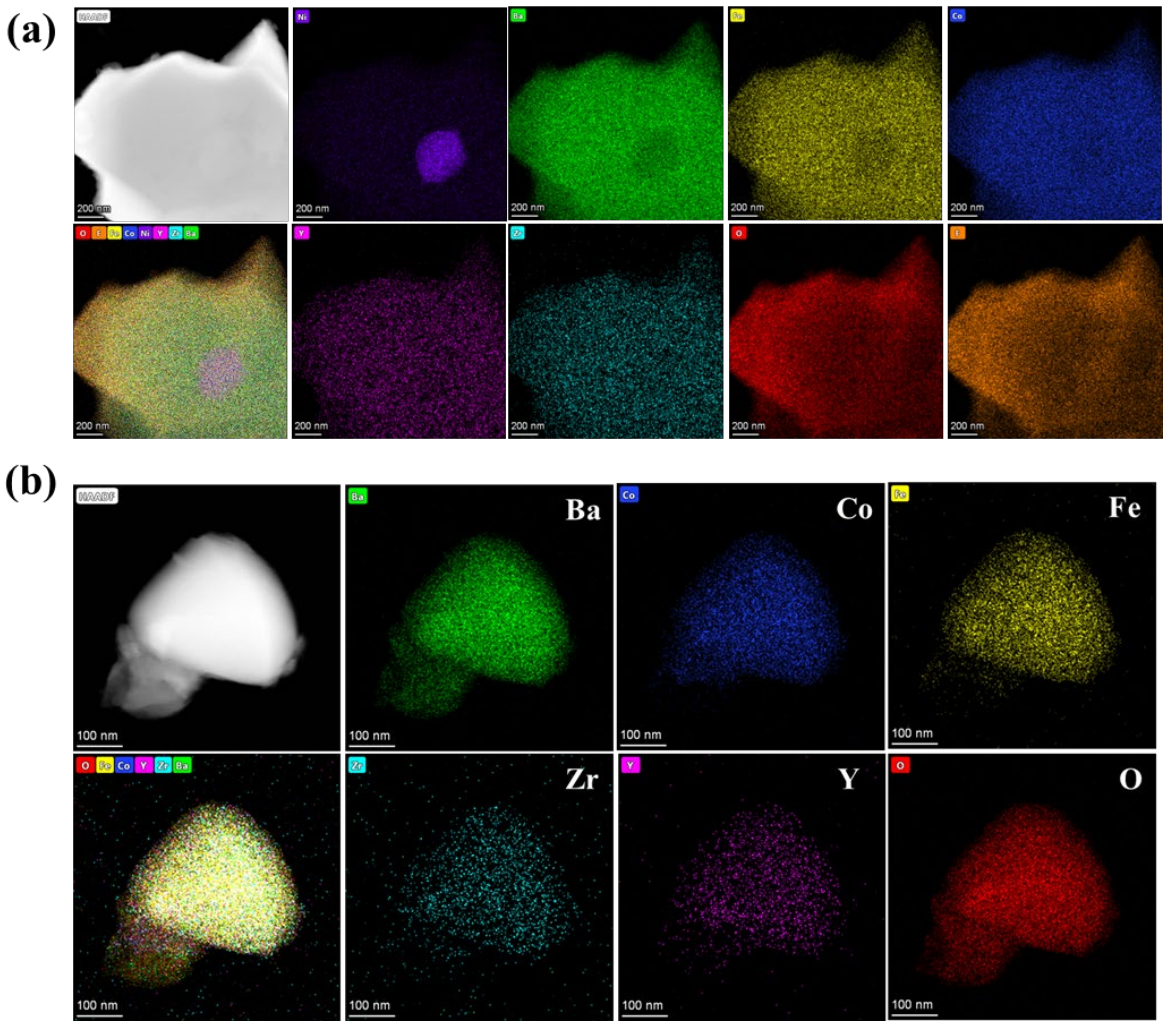

Figure 5.2 The elements distribution result of (a) the enlargement part of the images shown in Fig 5.1 (f) and (b) BCFZY sample.

5.2.2 Oxygen Activity in Lattice

As an idea air electrode functional material for R-PCECs, the high ORR/OER catalytic performance is strongly associated with the intrinsic oxygen chemical environment as well as the oxidation state of the transition metals at B-site of perovskite oxide[175, 179]. Therefore, to better comprehend the necessary modifications applied to conventional air electrodes and the diverse chemical characteristics of oxygen and B-site transition metals exhibited by the target air electrode, a detailed exposition has been schematically investigated. **Figure 5.3a** exemplifies the mechanism of highly actively M-O generation and nanoscale MO catalysis in-situ information through substituting the O-site and B-site of the parent oxide crystal structure

with F-element and Ni-element[147]. In further elucidating the impact of modification technology on the oxidation state of B-site transition cations in the perovskite oxide, the valence of Co and Fe in the bulk phases of BCFZY and the targeted N-BCFZYNF was comparatively studied using X-ray absorption fine structure (XAFS). The X-ray absorption near edge (K-edge) structure (XANES) results, depicted in **Figure 5.3b, c**, reveal a slightly higher valence state of Co in the modified N-BCFZYNF sample compared to the raw BCFZY sample, while the valence of Fe remains nearly constant. Given that the B-site dopant Ni introduced into the lattice primarily exists in the form of second-phase MO, the observed variations in the valence states of the transition metals are most likely attributed to the introduction of F anions. In fact, besides forming bonds with metals by substituting lattice oxygen sites, F anions may partially occupy oxygen vacancies bonding with transition metals, leading to an increase in the metal valence state. Similar experimental results have also been reported in other studies[153, 154]. Certainly, the minor B-site defects induced by partial precipitation of Ni would also trigger a certain degree of charge compensation by other transition metal cations at the B-site.

As previously discussed, the intrinsic oxygen chemical environment also contributes a lot in achieving the outstanding ORR/OER catalytic performance. Considering the crucial role played by the concentration of oxygen vacancies in air electrode materials, thermogravimetric (TG) technology was carried out to determine the oxygen non-stoichiometry (δ) of the investigated samples at the intermediate operating temperature of the R-PCECs. The TG curves in **Figure 5.3d** indicate that a more pronounced weight loss for N-BCFZYNF compared to BCFZY sample within the elevated temperature range of 100 ºC to 1000 ºC (solid line).

Specifically, the weight loss value for BCFZY is 1.67%, while that of N-BCFZYNF increases to 2.03%. Based on the molecular weights derived from their respective chemical formulas, the 0.37% weight loss difference implies a deviation of 0.1 in the stoichiometric number of oxygens. More oxygen vacancies generation, to a certain extent, implies that the crystal oxygen in the improved air electrode material is highly activated at intermediate temperatures, which is conducive to oxygen adsorption, oxygen ion generation, and bulk-phase conduction, thereby accelerating oxygen kinetics and facilitating the ORR/OER processes[155]. Simultaneously, the O_2-TPD was conducted to evaluate the oxygen desorption properties of these materials over a temperature range from 50 ºC to 800 ºC, and the profiles presented in **Figure 5.3e**. With the rise in temperature, the perovskite oxide's active cations underwent thermal reduction, resulting in a relatively lower oxidation state, and concurrently, oxygen was liberated from the crystal lattice. Hence, the decreased initial desorption temperature from 323.1 ºC for BCFZY to 303.9 ºC for N-BCFZYNF demonstrated that the faster surface oxygen exchange kinetics and the higher rate of oxygen migration within the perovskite lattice. To further get insights into the variability, O1s XPS spectra for these samples were obtained. As depicted in **Figure 5.3f**, the binding energies of lattice oxygen (O^{2-}) were measured at 528.37 eV and 528.67 eV for BCFZY and N-BCFZYNF samples, respectively. This increase can be ascribed to the reduction in valence electron density of O^{2-} in N-BCFZYNF due to the inclusion of F^-, which weakens the chemical bonds between A- or B-site metal cations and oxygen ions, rendering the lattice oxygen more active. These findings align with the results obtained from TG and O_2-TPD in this work, and other reported results[158, 159]. Moreover, one significant phenomenon that should be clarified is that the N-BCFZYNF electrode material exhibits a discernibly higher

concentration of oxygen components originating from bound water under identical conditions. This observation may suggest a significantly enhanced capacity for water and proton absorption capacity, thereby substantially improving the reaction kinetics of the R-PCEC air electrode. In summary, the obtained results preliminarily indicate that the intrinsic oxygen chemical environment becomes more favorable for the oxygen-involved R-PCEC air electrode reaction processes after modification, potentially leading to improved catalytic activity.

To validate the suitability of the improved air electrode material as a superior electrocatalyst for ORR, both samples were assembled into SDC electrolyte-supported symmetrical cells as the air electrode. The electrocatalytic performance was assessed through ASRs values determined by EIS techniques. As shown in **Figure 5.3g**, N-BCFZYNF had a lower ASR value (0.085 Ω cm^2) compared to BCFZY (0.12 Ω cm^2) when operated at 600 ºC in dry air. Clearly, the improved N-BCFZYNF holds a much better ORR activity under the same conditions, which is strongly associated with the enhanced state of the intrinsic oxygen chemical environment as well as the oxidation state of the B-site cations as analysis previously. Furthermore, the Arrhenius plots of the ASR values as a function of temperature range from 650 ºC to 450 ºC were summarized and displayed in **Figure 5.3h**. The targeted N-BCFZYNF always occupies the lowest ASR values, indicating the best ORR catalytic performance accordingly. These results affirm that the active M-O through incorporation of F^- and the surface modification with MO nanoparticles through incorporation of Ni^{2+} is a highly effective strategy for enhancing the ORR catalytical performance of R-PCEC air electrode.

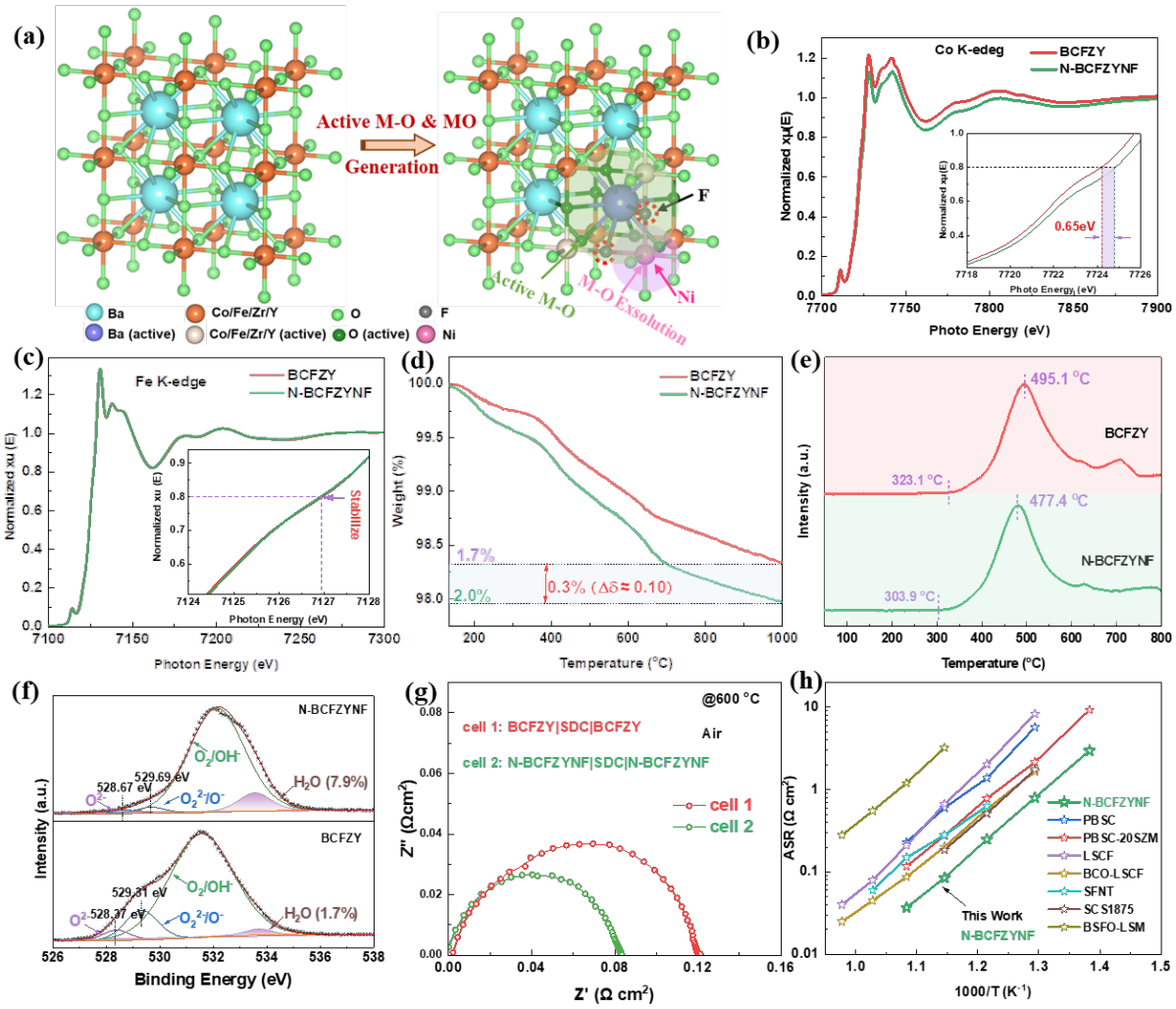

Figure 5.3(a) Schematic diagram of substituting the O-site and B-site of the parent perovskite oxide with F-element and Ni-element so that generated highly active M-O bonds and MO nanoscale phase. The comparison of BCFZY and modified N-BCFZYNF samples: (b) the spectra of Co K-edge XAFS and (c) Fe K-edge XAFS plots; (d) TG curves recorded at the temperature range of 100-1000 ºC in dry air; (e) O_2-TPD profiles between 50 ºC and 800 ºC; (f) the XPS spectra of O-1s; (g) the typic Nyquist plots of SDC-electrolyte supported cell at 600 ºC in dry air; (h) Arrhenius plots of the ASRs of the SDC-supported symmetrical cell as a function of temperatures in dry air.

5.2.3 The Triple Conductivity Properties

Exceptional triple conductivity (e^-, O^{2-}, H^+) capabilities are critical for R-PCEC's air electrode to achieve the favorable ORR/OER catalytic performance at intermediate temperatures. To explore the e^- migration prosperity, the electrical conductivities of BCFZY and N-BCFZYNF air electrode materials were measured between 350 ºC and 750 ºC in wet air,

and the recorded curves were shown in **Figure 5.4a**. Both samples displayed a typic p-type semiconducting behavior, where the electrical conductivity increase with rising temperature. Exactly, the BCFZY exhibited values ranging from 1.86 S cm^{-1} to 1.07 S cm^{-1}, whereas the N-BCFZYNF demonstrated values of 1.51 S cm^{-1} and 0.97 S cm^{-1}, respectively. The higher conductivities for BCFZY composite compared to N-BCFZYNF mainly resulting from the higher concentration of the oxygen vacancies in the oxide and the interface regions between the main cubic phase and NiO phase since they can acted as the scattering centers or random traps for electrons, and similar results were reported for other air electrodes[70, 182, 183].

For the air electrode material with triple conductivity property, one significant factor affecting the ORR/OER kinetics is the oxygen surface exchange and bulk migration rate. Herein, the oxygen incorporation kinetics were identified using the ECR measurements. These ECR response profiles provided important indicators linked with chemical surface oxygen exchange (k_{chem}) characteristics of the tested sample. Specific k_{chem} values in temperature ranging from 650 ºC to 450 ºC were summarized in **Figure 5.4c** and the normalizing conductivity relaxation curves were shown in **Figure 5.4b**. It is evident that with the decrease in test temperature, the time to reach a stable conductivity value (relaxation time) gradually increases. More importantly, the modified N-BCFZYNF sample exhibits a shorter relaxation time compared to BCFZY under the same conditions. For instance, as shown in **Figure 5.4b**, the relaxation time for BCFZY is 453 s at 600 ºC, while that of N-BCFZYNF is significantly shortened to only 120 s, which preliminarily implies an accelerated oxygen incorporation kinetic. Furthermore, it is confirmed by the larger k_{chem} values obtained from fitting the normalized conductivity relaxation curves. Specifically, the k_{chem} values of BCFZY at 600 ºC

were fitted to be 5.53×10^{-4} cm s^{-1}, while those indictors up to 1.91×10^{-3} cm s^{-1} after modification (**Figure 5.4c**). Additionally, the activation energy value of k_{chem} values based on operating temperature for N-BCFZYNF (0.36 eV) were lower compared with BCFZY (0.44 eV), confirmed that the surface generation and migration of O^{2-} were facilitated and thus prompting the typical ORR/OER steps.

Considering the actual operating atmosphere of R-PCECs' air electrode is humid air, exploration of the oxygen surface exchange and bulk diffusion kinetic characteristics in wet air is essential. **Figure 5.4d** illustrates the ECR response curves of the N-BCFZYNF sample in both dry and humid air environment. It can be visually observed that the relaxation time significantly increases in humid conditions, from an initial 120 s to 188 s, similar trend was also observed in the BCFZY sample. As previously analyzed, a longer relaxation time may indicate the sluggish oxygen ion introduction and migration processes. This is further validated by the D_{chem} and k_{chem} values fitted from the corresponding normalized conductivity relaxation curves at 600 ºC, with results shown in **Figure 5.4e**. The k_{chem} values of the N-BCFZYNF sample decreased from 1.91×10^{-3} cm s^{-1} to 7.91×10^{-4} cm s^{-1}, and a comparable reduction is also occurred for BCFZY sample. However, it is noteworthy that the introduction of Ni and F into the BCFZY lattice results in significantly higher k_{chem} compared to the parent sample, suggesting a more robust oxygen ion migration capability of the targeted N-BCFZYNF sample even in the humid atmosphere. These results further demonstrate that introducing F into the BCFZY lattice and the presence of Ni oxide on the surface can significantly enhance the generation and migration of oxygen ions, providing possibilities for higher ORR/OER catalytic activity.

Beyond the stronger oxygen mobile ability, the fast proton migration capability also plays an essential role in attaining the favorable ORR/OER catalytic performance. Herein, a feasible way by uplifting the H_2O partial pressure from dry (0 atm) to wet (0.1 atm) in the testing atmosphere was applied, and then the values of chemical diffusion coefficient of protons ($D_{H,chem}$) were determined form this prudent ECR responses to assess the protons transfer rate[162]. The typic ECR profiles were shown in **Figure 5.4f**, it could be clearly seen that the electrical conductance of BCFZY sample firstly experienced a short period of rise, and then subsequently decreased until reaching a steady state, similar curves trend was also observed for N-BCFZYNF sample. These interesting non-monotonic relaxation curves can be explained by the phenomenon that all the carriers (oxygen vacancies, holes, and proton defects) would redistribute accompanied by the proton transfer step[37, 162, 184]. Moreover, compared to the BCFZY material, the modified N-BCFZYNF air electrode material exhibits a faster response to changes in external humidity, with a significantly shortened relaxation time. This preliminary confirms its enhanced proton transport capability. Additionally, based on the normalized conductivity profiles of the air electrode samples at 550 °C, different $D_{H,chem}$ values were obtained and summarized in **Figure 5.4g**. The N-BCFZYNF sample demonstrates a higher value $D_{H,chem}$ of 3.349×10^{-5} cm s^{-1}, nearly 3 times that of the parent BCFZY sample (1.176×10^{-5} cm s^{-1}) under the same test conditions. These results further affirm the pronounced proton bulk transport capability of the N-BCFZYNF sample activated by M-O bonds.

In general, these results demonstrated that the vital oxygen and proton mobility ability of the R-PCECs' air electrode were significantly improved after incorporating F into the perovskite oxide lattice to activate the M-O chemical bonds and decorating the MO nanoscale

catalyst on the parent oxide surface. The mechanism of this promotion is schematically shown in **Figure 5.4h, i** from the aspect of lattice structure[164, 185, 186]. Benefiting from the altered oxidative environment, as well as the enhanced catalytic activity on the material surface, there is a noticeable acceleration in both surface oxygen exchange and bulk-phase oxygen transport processes, which manifests as a faster generation and migration of oxygen ions (even under humid conditions). Additionally, owing primarily to the activation of M-O bonds resulting from the replacement of lattice oxygen with more electronegative F anions in the bulk phase, the modified material exhibits enhanced hydration capability and proton migration processes. Combined with these enhancement factors, it is foreseeable that the surface modification fluorinated BCFZY air electrode may hold better ORR/OER catalytic performance and could be employed as an ideal air electrode in R-PCECs.

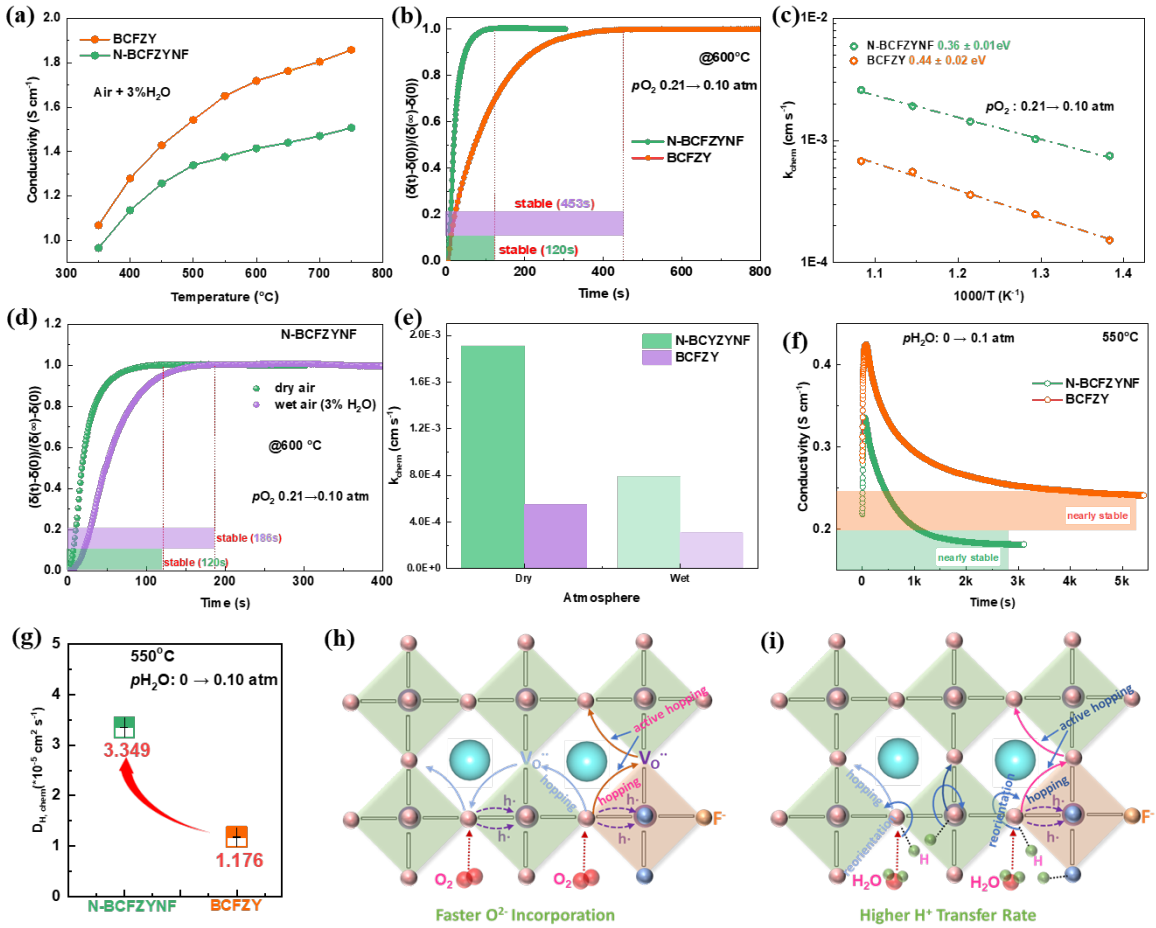

Figure 5.4 the triple conductivity (e-, O^{2-}, H^{+}) properties for BCFZY and N-BCFZYNF samples: (a) the electronic conductivity at 350 ºC -750 ºC in wet air; (b) the fitted D_{chem} and K_{chem} values from 450 ºC to 650 ºC; (c) the ECR responses curves; (d) the comparison ECR response profiles of N-BCFZYNF in dry air and wet air; (e) the summarized D_{chem} and k_{chem} values obtained from the different ECR process in dry air and wet air; (f) the typic ECR response profiles when switching the atmospheres from dry to pH_2O=0.10 atm at 550 ºC; (g) the comparison of fitted $D_{H,chem}$ values shown in **Figure 5.4f**; schematic diagrams of (h) higher O^{2-} mobility and (i) faster H^{+} migration rate properties for the designed N-BCFZYNF sample.

5.2.4 The Catalytic Performance

The electrocatalytic performance of the air electrodes was systematically investigated by assembling them in symmetrical cells with the configuration of (N)BCFZY(NF)|BZYCYYb|(N)BCFZY(NF). The detailed electrochemical reaction steps, illustrated in **Figure 5.5a,** provide a deeper insight into the mechanisms of the ORR/OER processes, simultaneously aiding in the elucidation of the specific factors contributing to the enhancement of electrode kinetics. The typic EIS was applied to evaluate electrocatalytic

activity between 650 ºC and 450 ºC. It could be found that the N-BCFZYNF exhibited a lower ASR value compared to the raw BCFZY at the same operating temperature in wet air. Specifically, as shown in **Figure 5.5b**, the ASR value for BCFZY electrode is determined to be 0.264 Ω cm^2 at 600 ºC, whereas that for N-BCFZYNF is only 0.165 Ω cm^2, indicating the better catalytic performance was achieved after targeted modification. To get further intuitive insights into this noticeable improvement, DRT technology was conducted by deconvoluting the corresponding EIS response to separate the overlapping electrode processes. Three main characteristic peaks were observed in the DRT plots denoted as three different segments according to the located frequency range: low frequency P1 (LF, $<10^0$ Hz), intermediate frequency P2 (IF, 10^0–10^2 Hz), and high frequency P3 (HF, $>10^2$ Hz). Referring the previously reported DRT analysis results and their located peak patterns related to R-PCEC air electrode, these can be assigned to the gas (O_2/steam) diffusion (P1), surface exchange and/or ions (H^+/O^{2-}) bulk migration (P2, Padd1 and Padd2), and ions/charges transfer in the interface between the electrolyte and electrode at three-phase boundaries (P3). Based on these illustrated results, the accelerated air electrode kinetic for N-BCFZYNF is mainly due to the faster sub-steps of surface exchange and ions bulk diffusion since the intermediate frequency peaks (P2, Padd1 and Padd2) were reduced significantly compared to the pristine BCFZY. In addition, the Arrhenius plots of ASR values as a function of temperature were calculated to compare with other reported high-temperature air electrode based on proton-conducting BZCYYb electrolyte supported cells in wet air, with the results summarized in **Figure 5.5c**. The N-BCFZYNF electrode still exhibited the smallest ASR values with a significantly reduced electrode Ea value, at only 1.16 eV, indicating the best catalytic activity for the air electrode reactions was obtained.

Furthermore, to enhance our comprehension of the electrochemical reaction kinetics for the N-BCFZYNF air electrode, EIS response curves and corresponding DRT plots under varying water partial pressure (pH_2O) and oxygen partial pressure (pO_2) were employed to provide additional insights into the individual elementary steps involved in the overall electrode reactions. **Figure 5.5d** displays the comparison fitted DRT plots for N-BCFZYNF sample when the pH_2O increases from 3% to 10% in air, form which three separated peaks were observed and nearly kept no change with the different steam content in the operating atmosphere. This phenomenon suggests that the air electrode reaction kinetics will keep stable even under high steam content, which could be further demonstrated by the determined ASR values form the Nyquist profiles in air with different pH_2O **(Figure 5.5e**). The ASR value for N-BCFZYNF air electrode, at around 0.165 Ω cm^2, is nearly stable, whereas those of BCFZY increase from the initially 0.264 Ω cm^2 to 0.296 Ω cm^2 with the pH_2O lift from 3% to 10%. This contrasting trend observed in different air electrodes further underscores the efficient stability of the modified N-BCFZYNF electrode's electrocatalytic activity, which is likely attributed to the enhanced proton generation and conduction capabilities of N-BCFZYNF, compensating for the weaker oxygen ion transport characteristics under high vapor pressure.

To delve deeper into the proton uptake and transport kinetics capabilities of both electrodes in a humid atmosphere, ASRs and DRT plots were conducted in humid nitrogen, eliminating the influence of O_2 mass diffusion, oxygen-related surface exchange, and O^{2-} transfer processes. The DRT analysis results (**Figure 5.5f)** indicated a reduction in all peaks for the fluorinated BCFZY decorated by NiO nanoparticles, suggesting an enhancement in all related to proton-involved sub-steps of electrode reactions. By combining the peak locations

and the analysis results presented in **Figure 5.5d**, this improvement can be attributed to faster H_2O diffusion (P1, LF) and the rapid formation and transfer of hydroxide defects (P2, P3, IF), aligning with the stronger proton transfer ability mentioned in **Figure 5.4**. The ions (H^+) transfer at the interface between the electrolyte and electrode layers (P4, HF) is primarily attributed to the heterojunction between the oxide nanoparticles and the parent perovskite. This illustrates that the outstanding formation and transfer of hydroxide defects of the N-BCFZYNF triple conducting oxide are highly valuable for R-PCECs air electrodes.

Above all, the EIS and DRT results collectively indicate that N-BCFZYNF exhibits superior electrocatalytic activity, and this excellent catalytic performance can be sustained over an extended period, as evidenced by the long-term stability of the symmetrical cell in humid air at 550 °C (**Figure 5.5g**). The assessed ASR values remained approximately 0.407 Ω cm^2 without significant degradation during the 300h-opetation in wet air, indicating remarkable durability of the N-BCFZYNF electrode on the BZCYYb proton-conducting electrolyte in a steam-containing atmosphere. With its efficient and stable electrocatalytic activity, this electrode is highly suitable for using as an air electrode in proton conductor electrolyte cells.

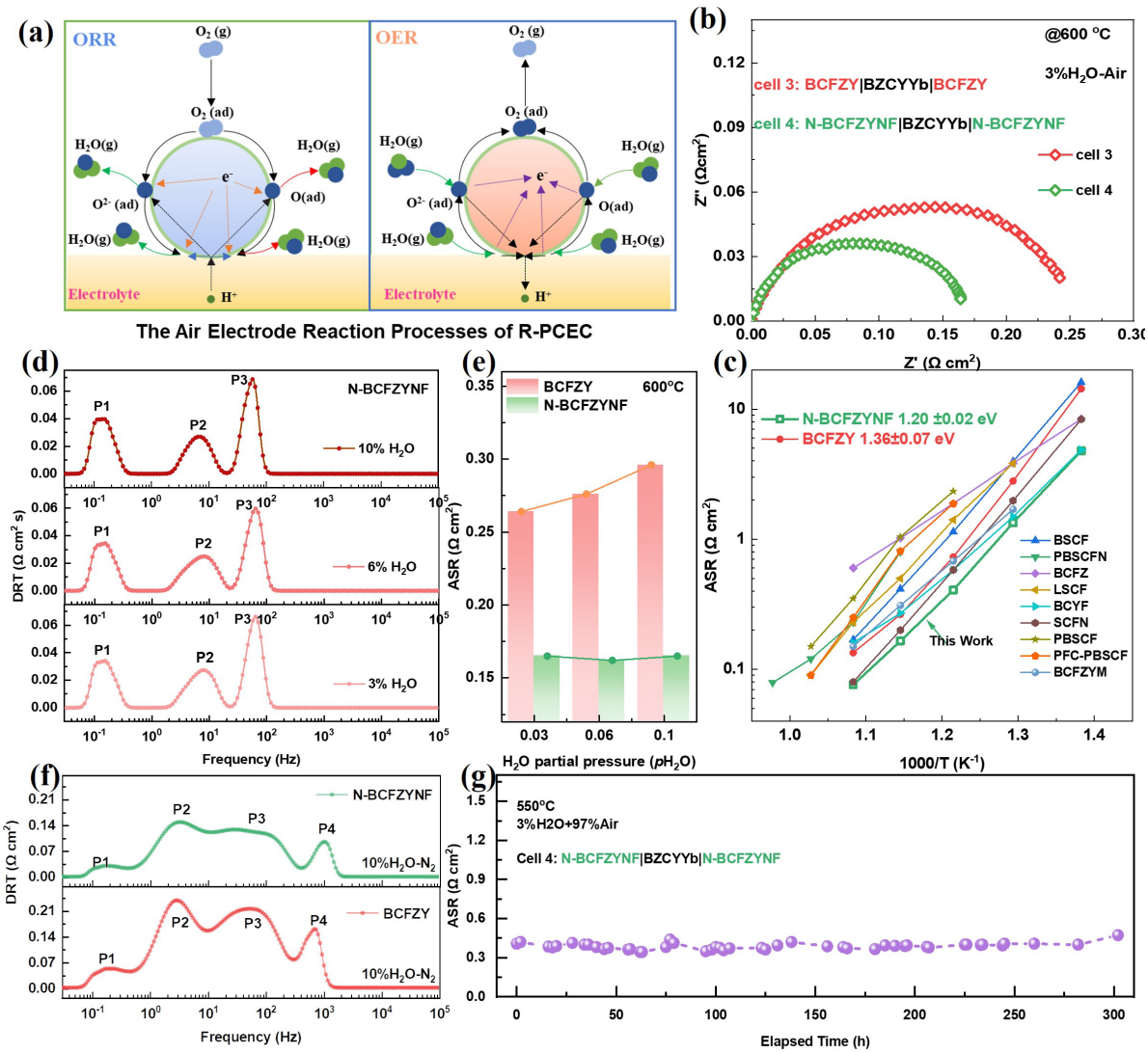

Figure 5.5 The electrocatalytic activity of BCFZY and N-BCFZYNF samples: (a) schematic illustration of the ORR/OER processes for air electrodes; (b) the Nyquist plots of symmetrical cell 3 and 4 at 600 °C in wet air; (c) Arrhenius plots of ASR values as a function of temperature in wet air; (d) the comparison of DRT plots for N-BCFZYNF sample in different pH_2O operating at 600 °C; (e) the corresponding ASR values of both samples; (f) the comparison DRT plots for various samples in high pH_2O (10%) without oxygen at 600 °C; (i) the long-term ASR values of symmetrical cell 4 with N-BCFZYNF air electrode.

5.2.5 Enhanced Electrochemical Performance

To verify the superior ORR/OER catalytic performance of N-BCFZYNF under real fuel cell operating mode, the NiO-BZCYYb fuel electrode supported single cells with the pristine BCFZY and modified N-BCFZYNF air electrodes were fabricated and tested, respectively. **Figure 5.6a** presents the typic i-V-p polarization curves of the PCFC with BCFZY air electrode,

fueled with pure H_2 and ambient air as the oxidant. It is evident that the PPD of this cell reached 626 mW cm^{-2} at 650 °C, the PPDs are 433 mW cm^{-2}, 284 mW cm^{-2},169 mW cm^{-2} when the operating temperatures down from 600 °C to 500 °C. Meanwhile, when the single cell utilized N-BCFZYNF as the air electrode (**Figure 5.6b**), its PPD values significantly increased to 996 mW cm^{-2}, 779 mW cm^{-2}, 545 mW cm^{-2}, and 374 mW cm^{-2} under the same test conditions, with the maximum PPD value experiencing a 60% enhancement at 650 °C. This enhancement confirms the superior ORR catalytic activity of the fluorine-nickel-modified BCFZY electrode. Remarkably, as shown in **Figure 5.6c**, the rarely high PPDs achieved for the single cell based on N-BCFZYNF is also outperformed most of state-of-art air electrodes reported so far, suggesting the favorable potential of applying the N-BCFZYNF as the air electrode for actual application. The exceptional performance can be attributed to the enhanced kinetics of oxygen and proton transport and surface diffusion, resulting in accelerated ORR catalytic activity. To underscore the operational stability of the N-BCFZYNF air electrode, a long-term durability test of this single cell was conducted under a constant current density of 0.42 A cm^{-2} at 550 °C, with results shown in **Figure 5.6d**. It can be observed that the cell voltage exhibited negligible degradation, stabilizing at around 0.79-0.75 V during the 60-hour operation. Simultaneously, the inset SEM image and results also confirmed that the N-BCFZYNF air electrode maintained good contact with the electrolyte film without any breaks or delamination after the durability test, indicating the favorable TEC matching and thermal stability properties of these layers.

Moreover, to validate the reversible ORR/OER electrocatalytic activities of the distinct air electrodes, equivalent single cells were prepared for electrochemical reversibility testing in the R-PCEC mode. As illustrated in **Figure 5.6e, f**, the obtained i-V curves of R-PCEC with

BCFZY air electrode and N-BCFZYNF-modified air electrodes both exhibited excellent reversibility between FC and EC modes by supplying pure H_2 and 3% H_2O-air to the fuel and air electrodes, respectively. Notably, the electrolysis current density for the BCFZY electrode reached 886 mA cm^{-2}, 527 mA cm^{-2}, 317 mA cm^{-2}, and 148 mA cm^{-2} at temperatures of 650 °C, 600 °C, 550 °C, and 500 °C, respectively, when the applied voltage was 1.3 V. Conversely, those of the N-BCFZYNF electrode sharply increased to 1570 mA cm^{-2}, 1089 mA cm^{-2}, 684 mA cm^{-2}, and 354 mA cm^{-2}, indicating the fluorine-nickel-modified BCFZY electrode's more active OER catalytic performance. Additionally, this remarkable electrolysis performance surpassed many reported state-of-the-art air electrodes assembled in R-PCECs **(Figure 5.6g**). Furthermore, as depicted in **Figure 5.6h**, an electrolysis operational stability test for this cell in EC mode was conducted at 550 °C. It was observed that the electrolysis performance of N-BCFZYNF remained stable without significant degradation under a constant high electrolysis current density of -0.50 A cm^{-2}, further demonstrating the superiority of the N-BCFZYNF electrode.

Most importantly, the good reversibility feasibility of the superior R-PCEC with this advanced N-BCFZYNF air electrode should also be emphasized for practical application. The cell reversibility was evaluated by cyclic switching between the hydrogen production (-0.50 A cm^{-2}) and power generation modes (0.38 A cm^{-2}) under varying current density conditions at 550 °C, with the results shown in **Figure 5.6i**. It can be intuitively seen that the R-PCEC has run stably throughout 15 reversible cycles within 100 h without appreciable performance degradation. The reliable conversion operational capability at different current densities strongly revealed that N-BCFZYNF air electrode has good durability and chemical stability, as

well as excellent adhesion and compatibility with the electrolyte. These findings suggest that the N-BCFZYNF holds promise as a potential air electrode material for R-PCEC with highly appreciated activity and durability.

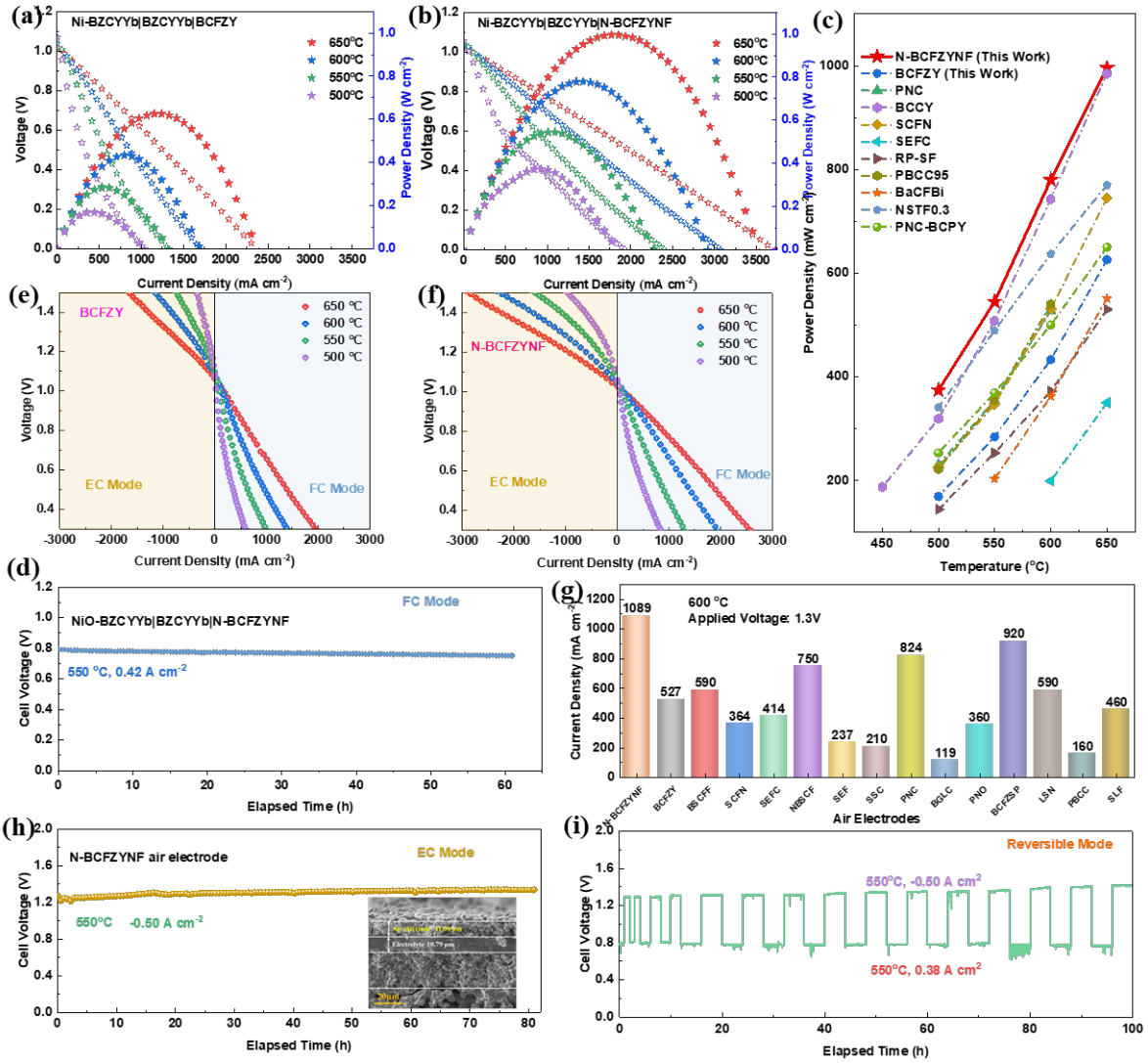

Figure 5.6 The electrochemical performance of R-PCEC with BCFZY and N-BCFZYNF air electrodes: the comparison i-V-p curves of the NiO-BZCYYb supported PCFCs with (a) the BCFZY and (b) N-BCFZYNF electrodes at 500 ºC-650 ºC; (c) the PPD values of PCFCs fabricated by different air electrodes (this work and other reported ones); (d) durability of single cell with targeted N-BCFZYNF air electrode at 550 ºC with a constant 0.42 A cm^{-2}; the i-V curves of R-PCEC operated at both modes at 500 ºC-650 °C with (e) BCFZY and (f) N-BCFZYNF air electrodes; (g) the electrolysis current density comparison of R-PCEC at 1.3 V with various air electrodes; (h) the stability of R-PCEC operated in electrolysis mode at 550 ºC; (i) The durability of continuous R-PCEC operation at 550 ºC.

5.3 Conclusion

Through simultaneously regulating both bulk-phase M-O bonds and in-situ formation of surface MO nano-catalyst, a novel bifunctional air electrode material was successfully synthesized (N-BCFZYNF). The physicochemical properties of this electrode material are systematically investigated, and all results reveal that the synergistic optimization effects at both bulk and surface modifications significantly enhance the electrochemical environment for interactions involving oxygen and protons, which manifested in substantially improved oxygen adsorption/desorption and hydration rates, as well as enhanced capabilities for oxygen ion and proton transport in both surface and bulk. Such improvements are deemed favorable for optimizing electrode kinetics. Therefore, the sluggish ORR/OER kinetics of the parent BCFZY air electrode is significantly accelerated, ensuring the excellent electrochemical performance of the N-BCFZYNF catalyst in both FC and EC modes. Specifically, the PPD operating in FC mode reached 996 mW cm^{-2} at 650 °C, and the electrolysis current density in EC mode reached a remarkably high value of 1570 mA cm^{-2} at an applied voltage of 1.3 V. The cyclic operation of power generation and hydrogen production under different current densities further demonstrated the high adaptability and durability of the N-BCFZYNF catalyst when assembled as the R-PCEC air electrode. This approach, simultaneously optimizing the bulk M-O chemical bonds and surface-modified MO nano-catalysts in the perovskite oxide air electrode, provides a rational design for functional materials aimed at improving the electrochemical performance of energy storage and conversion devices.

CHAPTER 6 Concomitant Activity-Stability Enhancement via Anionic Control and Multiphase Bulk Self-Assembly

6.1 Introduction

As previously discussed, triple-conducting ($H^+/O^{2-}/e^-$) air electrodes exhibit significantly enhanced ORR/OER catalytic activity at reduced operating temperatures in R-PCECs[13, 187]. Conventional design strategies focus on introducing proton conductivity and hydration capability into single-phase mixed ionic-electronic conductors (MIECs) through cation doping. For instance, A-site substitution with high-basicity cations—such as K^+ in $Ba_{0.9}K_{0.1}Co_{0.4}Fe_{0.4}Zr_{0.2}O_{3-\delta}$[170], $Sr_{1.75}K_{0.25}Fe_{1.5}Mo_{0.5}O_{6-\delta}$[171], and Cs^+ in $Ba_{0.95}Cs_{0.05}Ce_{0.3}Fe_{0.7}O_{3-\delta}$[188]—enhances hydration capacity, while B-site doping with hydrophilic, low-electronegativity cations (e.g., Zn-substitution in $PrBaCo_{1.9}Zn_{0.1}O_{6-\delta}$[189], Mg-incorporation in $Ba(Co_{0.4}Fe_{0.4}Zr_{0.1}Y_{0.1})_{0.95}Mg_{0.05}O_{3-\delta}$)[45] aims to foster proton defect formation. However, these approaches still suffer from some inherent limitations. For instance, K^+ volatilized during high-temperature sintering process[190], Cs^+ induced lattice distortion (due to large ionic radius at A-site) and cost inefficiency, while the catalytic activity reduced due to the non-transition metal dopants at B-site. Consequently, single-phase electrodes often achieve only compromised triple-conductivity rather than simultaneous optimization, which is not hard to become an idea bifunctional catalyst for ORR/OER.

To overcome these constraints, multiphase nanocomposite electrodes—particularly those formed via self-assembly (surface or bulk)—offer a promising choice. Specifically, surface self-assembly always generates minor nanoscale secondary phases on the surface of air electrode oxides (e.g., $BaCoO_3$ on $BaCo_{0.8}Zr_{0.1}Zn_{0.1}O_{3-\delta}$[191]; NiO on

$Pr_{0.2}La_{0.2}Ba_{0.2}Sr_{0.2}Ca_{0.2}Fe_{0.8}Ni_{0.2-x}O_{3-\delta}$[192], $BaCo_{0.85}In_{0.15}O_{3-\delta}$ on $PrBaCo_{1.9}In_{0.1}O_{5+\delta}$[193], CeO_2 and $La_{0.5}Sr_{0.5}CoO_{3-\delta}$ phases on $Ce_{0.2}Ba_{0.2}Sr_{0.2}La_{0.2}Ca_{0.2}CoO_{3-\delta}$[194]), which enhance surface oxygen/H_2O adsorption and bulk ionic transport, thereby improving ORR/OER activity[195]. Nevertheless, such surface phases (e.g., $BaCoO_3$, NiO, $La_{0.5}Sr_{0.5}CoO_{3-\delta}$) possess negligible proton conductivity and may block active reaction sites, thereby limiting electrode reaction kinetics. Therefore, bulk-phase self-assembly—enabling high-volume fractions of proton-conductive phases—is critical for optimizing triple-conductivity to enhance ORR/OER catalytic performance[196-198].

In addition to achieving high triple conductivity, exceptional steam resistance and thermodynamic compatibility with the electrolyte are also critical for air electrode materials in R-PCECs[199-201]. Superior steam resistance ensures sustained ORR/OER catalytic activity in humidified environments[202], whereas the oxides incorporating high-basicity or highly active cations (e.g., Ba^{2+}, Sr^{2+}, Co^{3+}) risk deleterious phase decomposition via humidity-induced bulk-to-surface segregation[200, 203]. On the other hand, thermodynamic compatibility minimizes interfacial resistance and enhances thermal stability due to the matching thermal expansion coefficients (TECs) between air electrode and electrolyte[204]. Currently, Co-rich perovskite oxides dominate air electrodes due to their superior redox activity and catalytic performance. However, excessive thermal expansion caused by $Co^{3+/4+}$ leads to instability at elevated temperatures[166, 205, 206]. Therefore, identifying Co-free alternatives is necessary to enhance the air electrode materials' steam resistance and thermal expansion, even though it will be at the expense of catalytic activity. To mitigate this challenge, a trade-off method through anion engineering is proposed[207]. Specifically, substituting electronegative F^- at oxygen sites to

weaken metal-oxygen bonds, thus enhancing ionic mobility while preserving catalytic performance[208, 209].

Following this rational design route, this work innovatively designs a bulk-phase self-assembled nanocomposite air electrode, $Ba(Zr_{0.1}Ce_{0.7}Y_{0.1}Yb_{0.1})_xFe_{1-x}F_{0.1}O_{2.9-\delta}$ (BZCYYFF, x = 0.5–0.7), through a synergistic combination of dual-phase architecture and anion engineering. The dual-phase structure integrates a Ce-rich proton/electron-conductive phase (P-BZCYYFF)—chemically akin to proton-conducting electrolytes like BZCYYb to ensure hydration tolerance and interfacial adhesion—with an Fe-rich oxygen-ion/electron-conductive phase (M-BZCYYFF) for rapid bulk oxygen ions and electrons transport. Moreover, the socked dual-phase nanostructure is achieved through the sharing A-site Ba^{2+} cations, isovalent B-site cations substitution, and interphase ion exchange via one-pot self-assembly process. Additionally, a Co/Sr-free composition eliminates phase segregation and thermal expansion mismatch in conventional perovskites, while F^- anion doping enhances ionic mobility without compromising catalytic activity.

By harmonizing high triple conductivity, steam resistance, and thermal compatibility, this design positions BZCYYFF as a novel air electrode for durable R-PCEC operation under harsh thermal and humidified operation conditions.

6.2 Results and Discussion

6.2.1 Nanoscale Biphasic Architectures

Herein, to systematically elucidate the influence of B-site Fe^{3+} cations and O-site F^- anions on the phase evolution of the parent materials, room-temperature XRD patterns were acquired for powders synthesized via a one-pot sol-gel co-sintering approach with fixed F^- and

controlled Fe^{3+} doping levels, as depicted in **Figure 6.1a**. All synthesized electrode materials exhibit a well-defined dual-phase nanocomposite architecture, consisting of a Fe-enriched cubic perovskite phase with mixed triple ($H^+/O^{2-}/e^-$) conductivity (M-BZCYYFF) and a Ce-rich rhombohedral phase dominated by protonic conduction (P-BZCYYFF). Notably, the absence of secondary phases (e.g., BaF_2) confirms the successful dual-anion/cation incorporation and self-assembly into impurity-free dual-phase nanocomposite. Critical analysis of the magnified XRD profiles (28–32° range) reveals two key trends: phase dominance modulation and lattice parameter evolution. The diffraction intensity of the M-BZCYYFF phase increases progressively with Fe^{3+} content, eventually becoming the majority phase, while P-BZCYYFF peaks diminish in intensity. Concurrently, a continuous contraction of the M-BZCYYFF unit cell is observed, contrasting with the invariant lattice dimensions of P-BZCYYFF. These phenomena corroborate the $Fe^{3+/4+}$ enrichment in the M-BZCYYFF and $Ce^{3+/4+}$ segregation into the P-BZCYYFF. The lattice contraction in M-BZCYYFF directly correlates with a gradual reduction in Ce^{3+} occupancy within its structure. This partitioning behavior arises from the substantial ionic radius mismatch at the shared B-site: Ce^{3+} (1.03 Å) $\gg$ Fe^{3+} (0.64 Å), which thermodynamically limits Fe^{3+} substitution in the Ce-dominated P-BZCYYFF lattice.

Rietveld refinement of sample F6 (**Figure 6.1b**) quantitatively resolves the phase distribution and crystallographic parameters. The refined model identifies M-BZCYYFF with Pm-3m space group as the primary phase (72 wt%), while P-BZCYYFF with R-3c space group constitutes only 28 wt%. This experimental phase ratio markedly deviates from the theoretical prediction (45 wt%, assuming complete Ce ions partitioning in P-BZCYYFF), providing

unambiguous evidence for partial Ce retention in the M-BZCYYFF matrix.

The HR-TEM images of the F6 sample (**Figure 6.1c**) reveal an interpenetrating dual-phase nanostructure, indicative of excellent interfacial compatibility and structural stability. Furthermore, lattice fringe measurements in regions ① and ② yield interplanar spacings of 2.88 Å and 3.08 Å, respectively, corresponding to the (110) plane of the M-BZCYYFF phase (denoted as M-F6) and the (104) plane of the P-BZCYYFF phase (denoted as P-F6). These values exhibit close agreement with XRD-derived d-spacing data and Rietveld refinement results.

To elucidate the elemental partitioning between these two phases, ED) elemental mapping and line-scan profiles of Ce and Fe were acquired (**Figure 6.1d**). Distinct localized enrichment of Ce and Fe is observed, consistent with the nanoscale dual-phase architecture comprising P-F6 and M-F6. The line-scan profiles further confirm this phase-segregated configuration, showing abrupt increases in atomic ratios at phase boundaries, thereby demonstrating ordered dual-phase alternation. Notably, the Fe-enriched regions retain a non-negligible Ce concentration (>5 at%), confirming partial Ce incorporation into the M-F6 phase. This residual Ce doping likely enhances the triple-conducting ($H^+/O^{2-}/e^-$) capability of M-F6 by facilitating proton transport, a hypothesis aligned with the lattice parameter shifts observed in XRD analysis.

Complementary EDS mapping of all constituent elements (**Figure 6.1e**) reveals homogeneous distributions for non-phase-segregated species (e.g., Ba, Zr, Y), underscoring their uniform solubility across both phases and further corroborating the interfacial coherence. Importantly, the anion sublattice elements (F^- and O^{2-}) also exhibit uniform spatial distribution,

confirming the successful incorporation of F^- anions into the oxygen sublattice as designed. Collectively, these multimodal characterization results unambiguously validate the coexistence of nanoscale M-F6 and P-F6 phases, with precise anion/cation doping achieving targeted lattice integration.

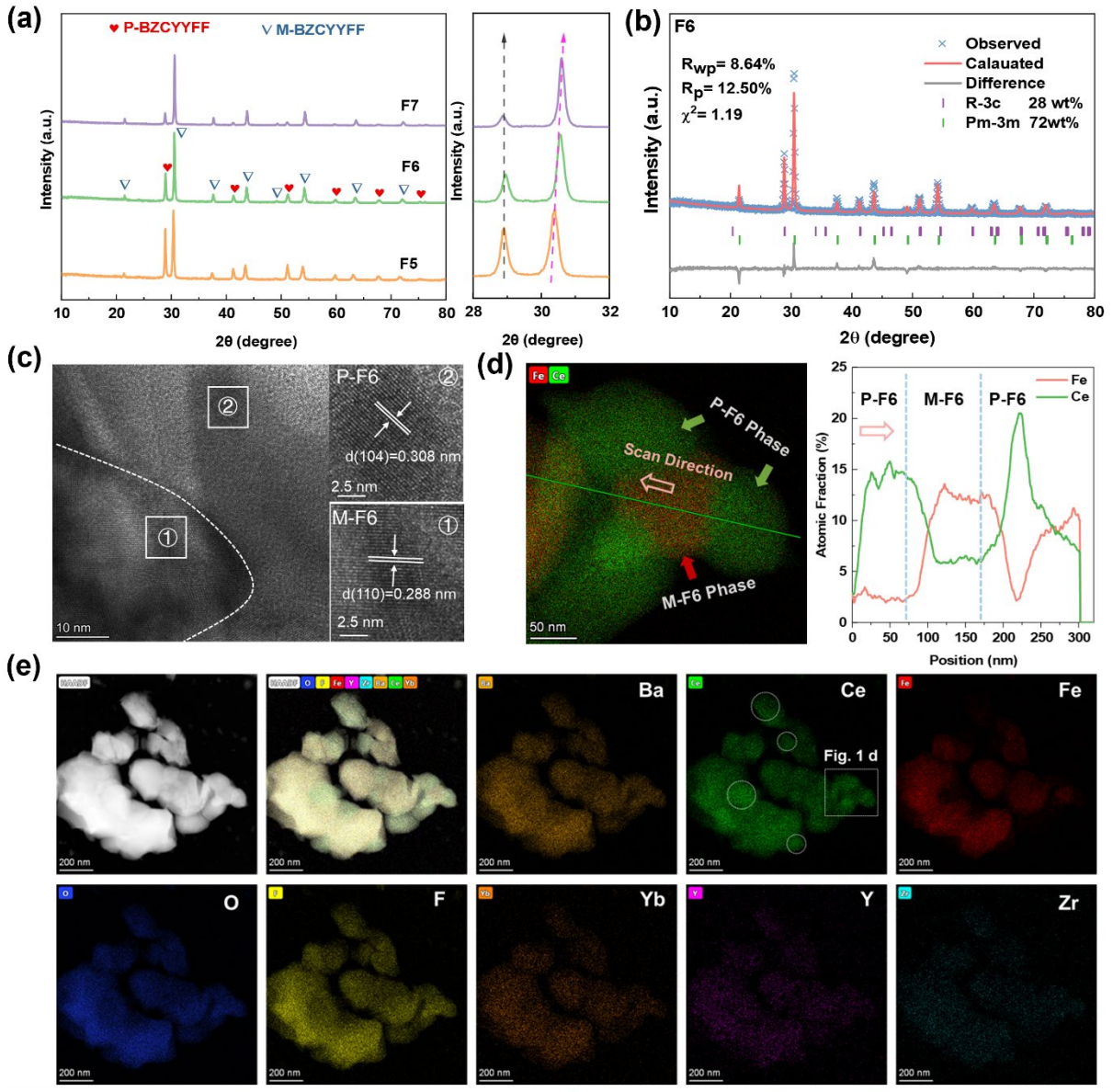

Figure 6.1 (a) The XRD patterns and its enlargement of F5, F6 and F7 powders; (b) The Refinement results of F6 sample; (c) HR-TEM images of F6 sample; (d) The Fe and Ce elements distribution and its line scan results of F6 sample; (e) The EDS mapping results of F6 sample.

6.2.2 Steam and Heating Resistance

The stability of R-PCEC air electrode materials under humidified atmospheres is critical

for their practical application. To evaluate the physicochemical durability of the synthesized air electrode material, the F6 sample was subjected to a 100-hour aging treatment in air containing 5 vol% H_2O at 550 °C, followed by morphological and structural characterization. SEM images (**Figure 6.2a, b**) reveal negligible microstructural degradation, with both samples maintaining their original morphology—bulk substrates decorated with uniformly dispersed secondary nanoparticles. Complementary XRD analysis (**Figure 6.2c**) confirms the phase stability of the dual-phase composite, as no impurity phases are detected after prolonged steam exposure. These results collectively demonstrate the exceptional hydrothermal resistance of the F6 material, attributed to its robust dual-phase architecture.

Thermal compatibility with the electrolyte is another vital criterion for air electrodes, as it governs the integrity of the electrolyte-electrode interface during thermal cycling. The thermomechanical behavior of F5–F7 samples was investigated via dilatometric measurements over 300–900 °C to determine their thermal expansion coefficients (TECs), as shown in **Figure 6.2d**. All samples exhibit nearly overlapping expansion/contraction curves during heating and cooling cycles, indicating excellent thermal cycling stability. Calculated TEC values (**Figure 6.2e**) reveal a progressive increase with Fe content, rising from F5 to F7. This trend correlates with the increasing proportion of the M-BZCYYFF phase, which exhibits intrinsically higher thermal expansion than the Ce-rich P-BZCYYFF phase at elevated temperatures. Remarkably, the TEC of the optimized F6 sample (12×10^{-6} K^{-1}) remains significantly lower than those of conventional air electrodes (typically $>17 \times 10^{-6}$ K^{-1})[121, 210-224]. This superior thermomechanical compatibility arises from a synergistic combination of phase-intrinsic thermal expansion suppression—where both phases exhibit reduced TECs compared to their

monophasic counterparts—and interphase constraint effects mediated by the interpenetrating dual-phase architecture, which mechanically buffers lattice expansion through mutual stress compensation at phase boundaries. Moreover, these attributes ensure close thermal matching with state-of-the-art electrolytes (BZCYYb: TEC ≈ 10 × 10^{-6} K^{-1}), minimizing interfacial delamination risks during operation.

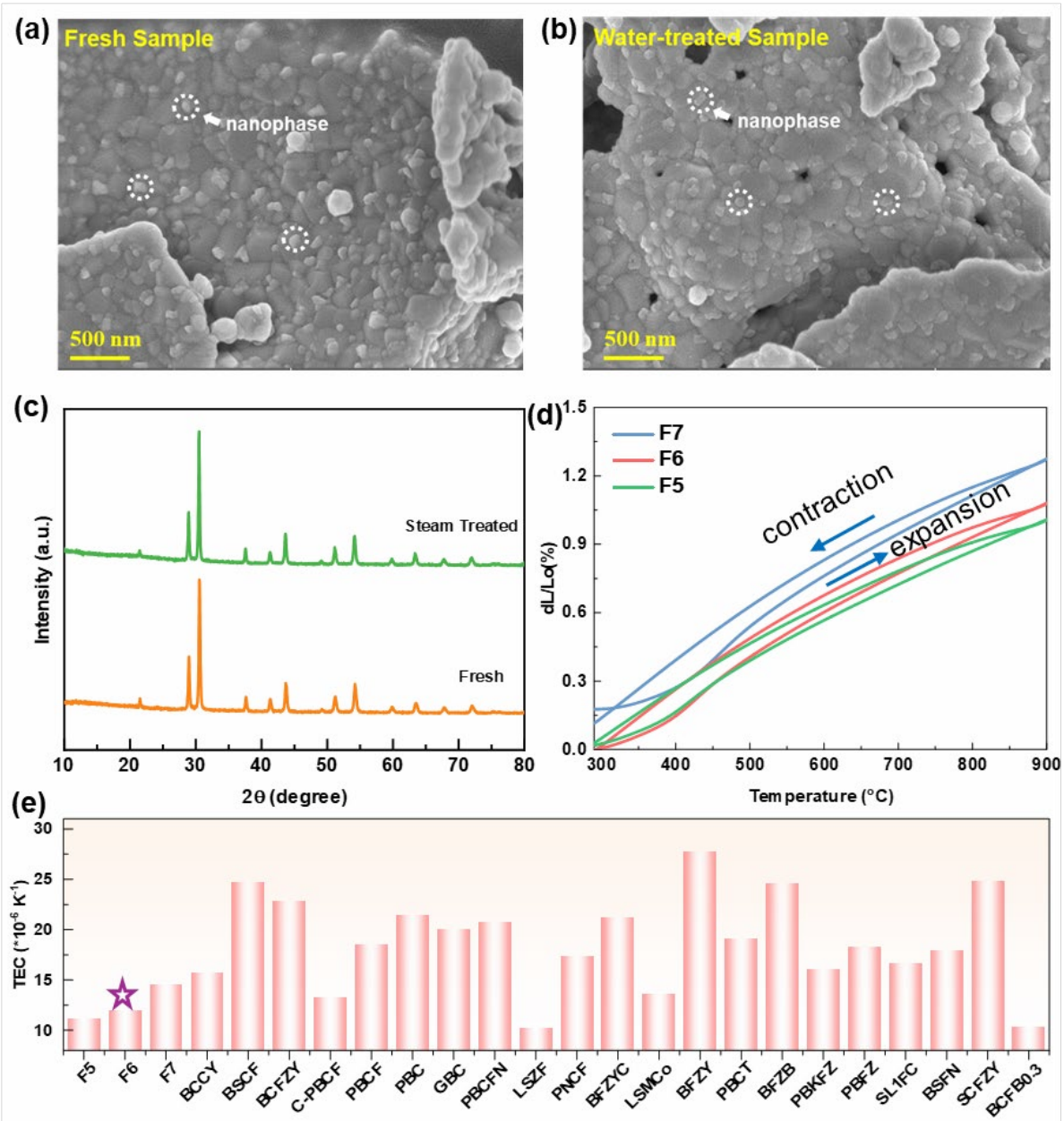

Figure 6.2 The SEM images of the powder treated in (a) dry air and (b) 5%H_2O-air for 100 h at 550 ℃; (c) The corresponding XRD pattern; (d) Thermal expansion and contraction curves of F5, F6 and F7 bar samples at 300–900 ℃; (e) The TEC values for various air electrode

materials in this work and other reported results.

6.2.3 Triple Conductivity Ability

The high ORR/OER catalytic performance of R-PCEC air electrodes is critically dependent on the intrinsic proton and oxygen incorporation and transport properties of the designed materials, which are strongly correlated with oxygen vacancy concentration. To quantify oxygen non-stoichiometry (δ), thermogravimetric (TG) analysis was performed on the synthesized materials (**Figure 6.3a**). The F6 sample exhibited significantly greater weight loss (2.91%) compared to F5 (1.39%) and F7 (1.65%) over 40–900 ℃ in dry air. Based on stoichiometric calculations, the derived δ values for F5, F6, and F7 were 0.24, 0.49, and 0.27, respectively, confirming that F6 generates abundant oxygen vacancies at elevated temperatures to enhance oxygen kinetics. Complementary XPS O-1s spectra (**Figure 6.3b**) revealed that F6 possesses the lowest lattice oxygen content (10.0%) compared to F5 (14.1%) and F7 (16.7%), further corroborating its elevated oxygen vacancy concentration, which promote crystal lattice oxygen activation at intermediate temperatures, thus facilitating oxygen adsorption, oxygen-ion generation, and bulk-phase conduction—key steps in accelerating ORR/OER kinetics. Notably, adsorbed water species (H_2O/CO_3^{2-}) in F6 remained comparable to F5 but significantly higher than F7. This disparity likely arises from the reduced proportion of the proton-conductive Ce-rich phase (P-BZCYYFF) in F7, which diminishes its capacity to form protonic defects and compromises proton conductivity.

The proton/oxygen-ion incorporation and transport kinetics—critical determinants of ORR/OER activity—were probed via ECR measurements. Normalized conductivity relaxation curves for F6 in dry air (**Figure 6.3c**) and derived D_{chem} and k_{chem} across 450–650 ℃ (**Figure 6.3d**) demonstrate accelerated kinetics with increasing temperature. Specifically, D_{chem}

increased from 0.128 × 10^{-3} to 0.462 × 10^{-3} $cm^2 \cdot s^{-1}$, while k_{chem} rose from 1.36 × 10^{-3} to 4.48 × 10^{-3} $cm \cdot s^{-1}$, surpassing advance electrodes such as BSCFF and N-BCFZYNF.

Given the operational relevance of humidified environments for R-PCEC electrodes, ECR kinetics were further evaluated under 3% H_2O-air at 550 ℃ (**Figure 6.3e**). The relaxation time decreased slightly from 241 s (dry) to 229 s (humidified), with corresponding increases in D_{chem} (0.212 → 0.259 × 10^{-3} $cm^2 \cdot s^{-1}$) and k_{chem} (0.228 → 0.270 × 10^{-3} $cm \cdot s^{-1}$). This marginal enhancement under humidified conditions reflects the dual-phase architecture's hydration resistance and its ability to maintain structural/chemical stability. The coexistence of Ce-rich P-BZCYYFF and Fe-rich (Ce included) M-PZCYYFF phases create abundant proton/oxygen-ion adsorption sites and transport channels, ensuring robust oxygen kinetics without significant protonic defect interference.

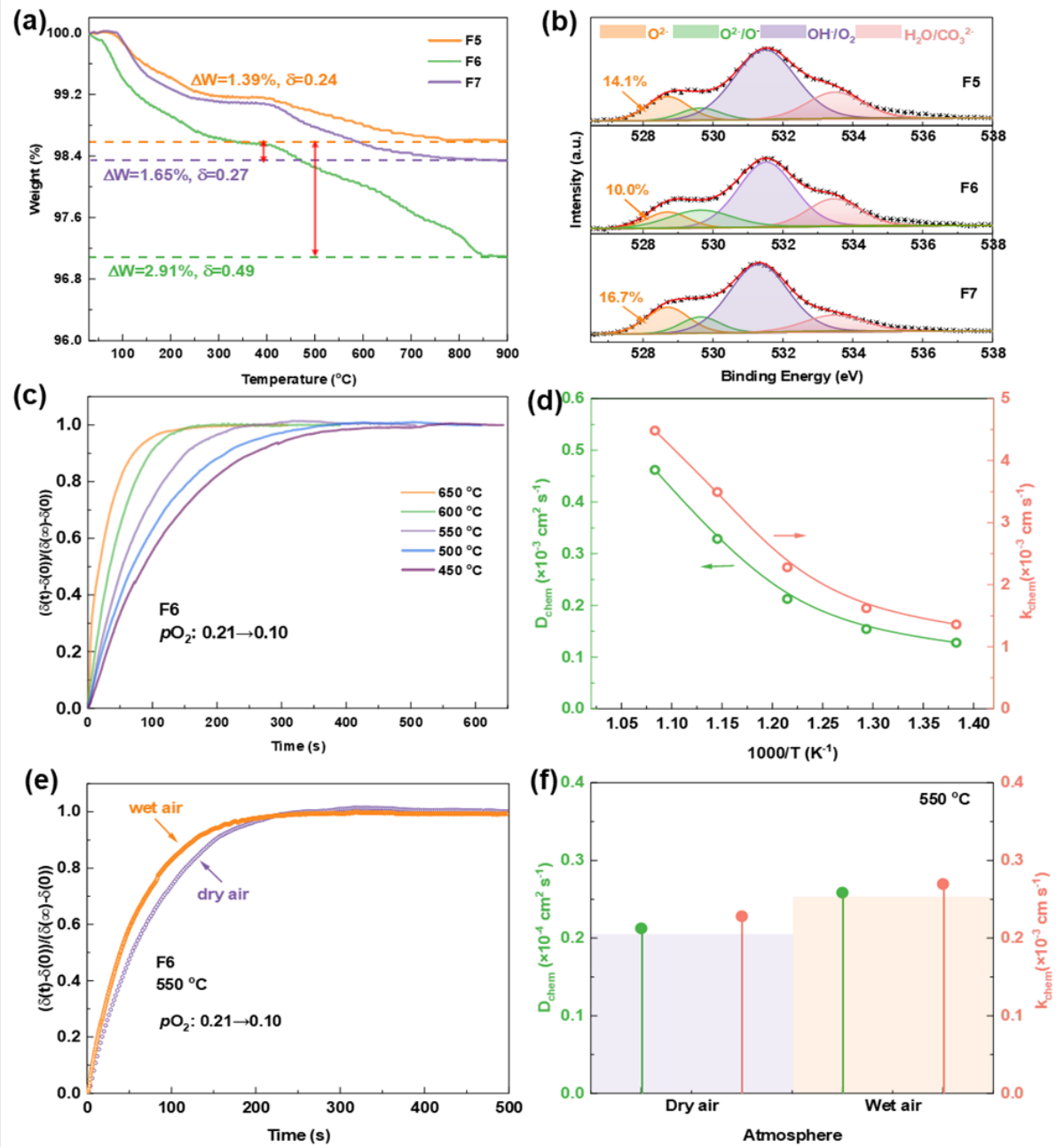

Figure 6.3 (a) TG analysis of F5-F7 powders measured over 40–900 °C in dry air; (b) XPS spectra of O-1s for F5-F7; (c) the ECR responses curves of F6 sample when switching oxygen partial pressure in dry air across 450-650 °C; (d) Temperature-dependent D_{chem} and k_{chem} values derived from the ECR transients in (c); (e) Comparative ECR kinetcs of F6 in dry versus 5%H_2O-humidifed air at 550 °C; (f) Summarized D_{chem} and k_{chem} values from the ECR process in (d).

6.2.4 Symmetrical Cell Performance

Collectively, these results validate F6 as a high-performance triple-conducting ($H^+/O^{2-}/e^-$) air electrode, combining exceptional ORR/OER activity with operational stability in both dry

and humidified environments.

To systematically evaluate the electrocatalytic activity of the air electrode materials, the electrochemical performance of symmetrical cells (configuration: Fx|BZCYYb|Fx, x=5, 6, 7) was investigated under humidified air. As shown in the EIS Nyquist plots (**Figure 6.4a**), the ASR values of the F5, F6, and F7 electrodes at 550 °C in 3% H_2O-air were 1.01, 0.33, and 0.64 $\Omega \cdot cm^2$, respectively, demonstrating the superior electrocatalytic activity of the F6 electrode. Moreover, to elucidate this enhanced reaction kinetics, DRT analysis was performed by deconvoluting the EIS data to resolve overlapping electrochemical processes (**Figure 6.4b**). The DRT profiles exhibited four characteristic peaks, categorized into three frequency domains:

Low-frequency peak (LP, $<10^0$ Hz) which is associated with gas-phase diffusion (O_2/H_2O); Medium-frequency peak (MP, 100–10^3 Hz) which is attributed to surface exchange and bulk transport of ionic species (H^+/O^{2-}). High-frequency peak (HP, $>10^3$ Hz) which corresponds to charge transfer at the triple-phase boundaries (TPB). A marked reduction in the integrated areas of the MP and LP peaks was observed for the F6 electrode compared to F5 and F7, while the HP peak remained unchanged. This indicates that the accelerated electrode kinetics of F6 primarily originate from improved proton/oxygen-ion surface exchange and bulk transport properties, consistent with its physicochemical characteristics analyzed earlier (**Figure 6.3**).

To further benchmark the electrocatalytic performance, Arrhenius plots of ASR values for the F6 electrode were compared with state-of-the-art air electrodes in humidified air (450–650 °C, **Figure 6.4c**). The F6 electrode exhibited the lowest ASR values and a minimal activation energy (E_a=1.08 eV), confirming its exceptional catalytic activity for ORR/OER.

The dependence of ASR on gas-phase composition was investigated by varying H_2O

partial pressure (pH_2O) and O_2 partial pressure (pO_2), as shown in **Figure 6.4d, e**. Increasing pH_2O from 3% to 20% induced a marginal ASR increase (0.33→0.40 $\Omega \cdot cm^2$), whereas elevating pO_2 from 10% to 80% caused a drastic ASR reduction (0.43→0.21 $\Omega \cdot cm^2$, >100% decrease). This pronounced pO_2 sensitivity underscores enhanced oxygen kinetics facilitated by abundant surface oxygen adsorption sites and bulk oxygen vacancies. The minor pH_2O effect likely stems from competitive consumption of oxygen vacancies by hydration and oxygen-ion transport processes. Notably, the dual-phase architecture (triple-conducting M-BZCYYFF and proton-conducting P-BZCYYFF) enables efficient water utilization while mitigating excessive hydration, ensuring balanced proton and oxygen-ion conduction—a critical feature for robust R-PCEC air electrodes.

Thermal cycling stability was assessed by subjecting the F6-based cell to 20 thermal cycles (500–600 °C, 10 °C/min ramp rate). The ASR values remained invariant across cycles (**Figure 6.4f**), demonstrating exceptional thermomechanical stability and compatibility with the BZCYYb electrolyte. Additionally, long-term durability testing at 550 °C in 10% H_2O-air revealed stable ASR values (~0.33 $\Omega \cdot cm^2$) over 320 hours (**Figure 6.4g**), confirming negligible performance degradation.

The synergistic integration of high electrocatalytic activity, phase stability, and thermochemical robustness positions the F6 dual-phase electrode as a promising air electrode candidate for proton-conducting electrochemical cells.

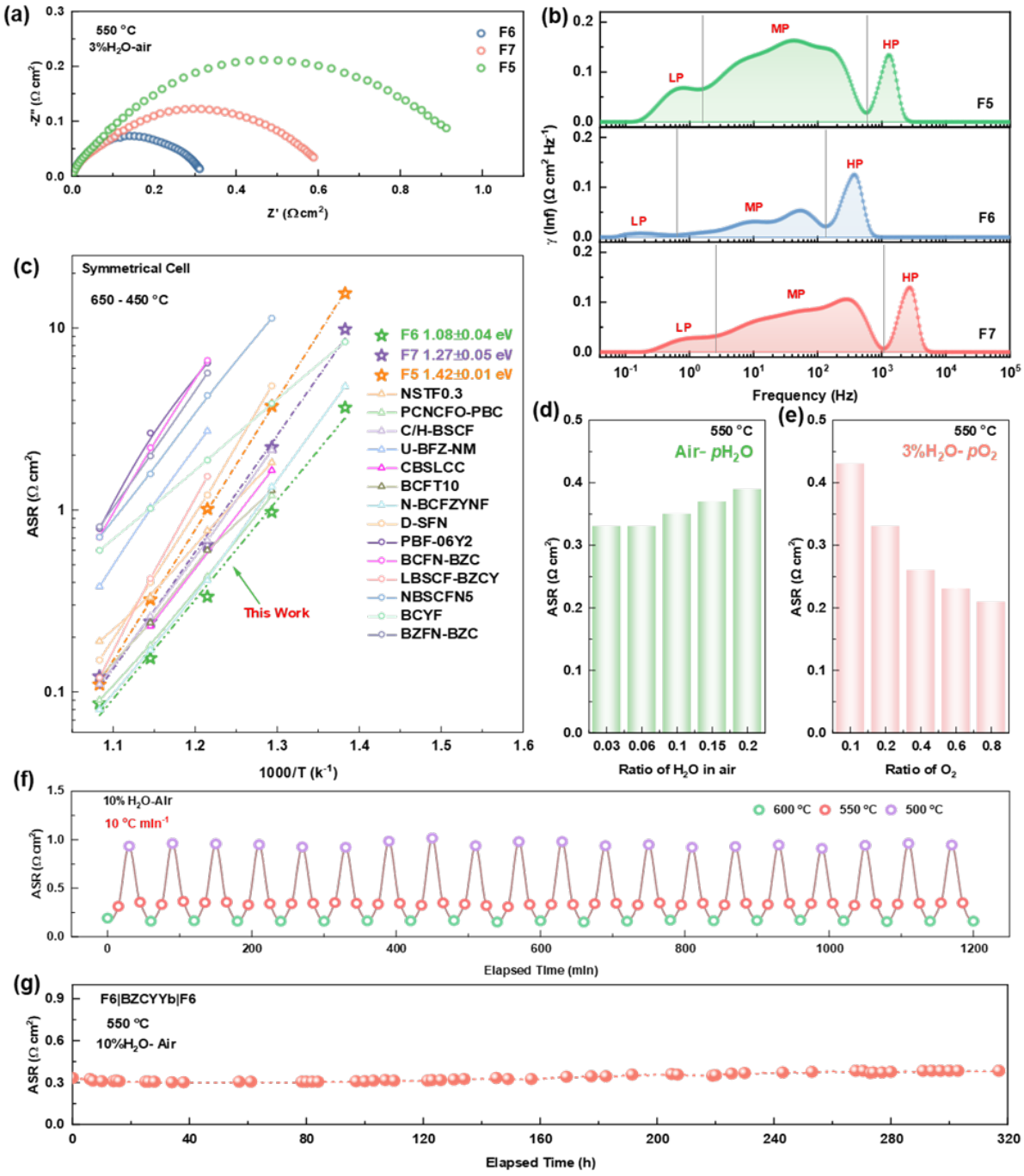

Figure 6.4 (a) The Nyquist plots and (b) corresponding DRT analyses of symmetrical cell employing F5, F6 and F7 air electrodes at 550 ℃ in humidified air; (c) Arrhenius plots of ASR for different air electrodes as a function of temperature (450-650 ℃) in wet air for; ASR dependence of F6 electrode under varying atmospheres; (d) pH_2O in air and (e) pO_2 with 3%H_2O; (f)Thermal cycling stability of the F6-based symmetrical cell subjected to repeated temperature ramping between 500 ℃ and 600 ℃; (g) Long-term ASR stability of the symmetrical cell with F6 electrode operated at 550 ℃ in 10%H_2O-air over 320h.

6.2.5 Electrochemical Performance in FC Mode

To validate the exceptional ORR/OER catalytic performance of the synthesized air

electrode under practical fuel cell operating conditions, Ni-BZCYYb fuel electrode supported single cells were fabricated and tested using F5, F6, and F7 air electrodes. **Figure 6. 5a** compares the current-voltage-power density (i-V-p) profiles of these cells under identical testing conditions (550 ℃, air). The F6-based cell demonstrated superior electrochemical performance, achieving a peak power density (PPD) of 0.494 $W \cdot cm^{-2}$, significantly outperforming the F5 (0.412 $W \cdot cm^{-2}$) and F7 (0.341 $W \cdot cm^{-2}$) counterparts. This enhanced PPD aligns with the minimized ASR of the F6 electrode shown in **Figure 6.4**, underscoring the critical role of optimized triple-phase boundaries enabled by its dual-phase architecture, which facilitates superior proton/oxygen-ion surface exchange kinetics and bulk transport properties. To further probe the temperature-dependent catalytic activity, the F6-based cell was evaluated across 500–650 ℃ (**Figure 6. 5b**). Remarkably, PPDs of 0.778, 0.614, and 0.386 $W \cdot cm^{-2}$ were achieved at 650, 600, and 500 ℃, respectively, demonstrating exceptional low-temperature performance. Comparative analysis with state-of-the-art air electrodes (**Figure 6. 5c**) confirms the competitiveness of the F6 electrode, which ranks among the highest-performing systems reported for protonic ceramic cells at 550 ℃. Crucially, this high catalytic activity is coupled with robust operational stability. As evidenced in **Figure 6. 5d**, the F6-based cell maintained a stable output voltage of ~0.80 V for 110 hours under a constant current density of 0.40 $A \cdot cm^{-2}$ at 550 ℃, with negligible degradation. These results collectively validate the F6 air electrode as a high-performance, durable catalyst for proton-conducting fuel cells, combining enhanced ORR/OER kinetics with thermochemical resilience under realistic operating conditions.

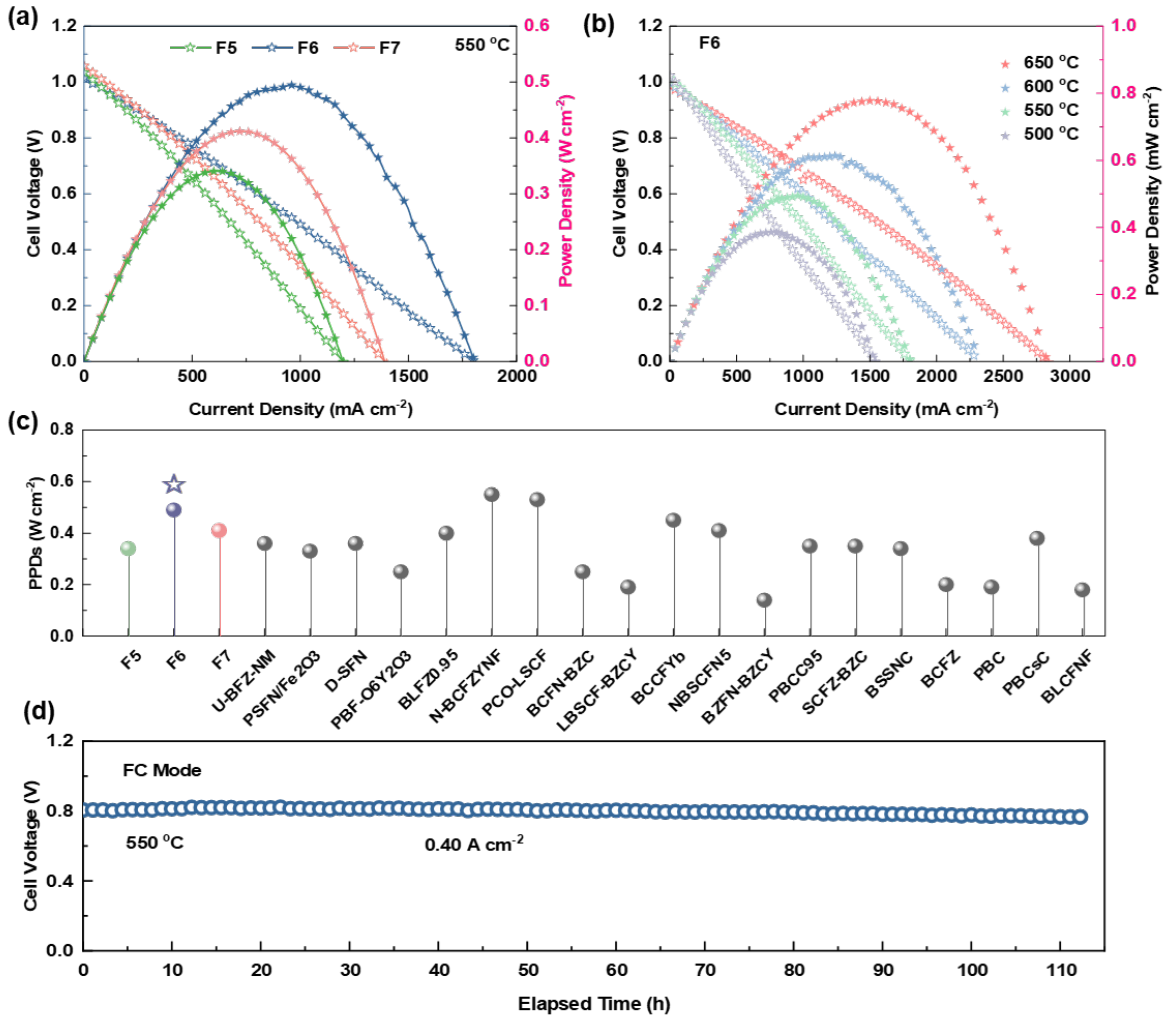

Figure 6.5 (a) i-V-p profiles of single cells employing F5, F6 and F7 air electrodes at 550 °C; (b) Temperature-dependent i-V-p characteristics of the F6-based single cell across 450-650 °C; (c) Comparative PPDs achieved by single cell with F6 air electrode (this work) against state-of-art air electrodes reported in other literatures; (d) Durability of the F6-based single cell operated at 550 °C under a constant current density of 0.40 A cm^{-2}.

6.2.6 EC Performance and Stability

To further validate the reversible ORR/OER electrocatalytic activity of the dual-phase air electrode, F6-based R-PCEC was assembled and evaluated under bidirectional operating conditions. As shown in **Figure 6.6a**, the i-V curves demonstrate exceptional reversibility between FC and EC modes at 500–600 °C, with humidified air (5% H_2O) supplied to the air electrode. Notably, under an applied voltage of 1.3 V, the EC-mode current densities reached 0.917, 0.649, and 0.448 A·cm^{-2} at 600, 550, and 500 °C respectively. Stability tests under

alternating current densities (±0.16-±0.64 $A \cdot cm^{-2}$, 2-hour intervals per step) revealed negligible voltage degradation, confirming robust operation during rapid mode transitions (**Figure 6.6b**). This operational resilience of the F6-based R-PCEC arises from synergistic interfacial robustness—evidenced by post-test SEM showing intact electrode-electrolyte adhesion without delamination (**Figure 6.6c, d**), attributable to matched TECs—and catalytic durability enabled by the dual-phase architecture, which sustains stable ORR/OER activity via hydration-resistant proton/oxygen-ion transport pathways. Moreover, the EC performance metrics are particularly remarkable when against state-of-the-art R-PCEC air electrodes (such as BCFZY, BSCFF, SCFN, PBCsC) at 550 ℃ **Figure 6.6e**. Under prolonged EC operation ($-0.40\ A \cdot cm^{-2}$, 550 ℃), the F6-based cell exhibited <3% voltage decay over 180 hours at 10%H_2O-air (**Figure 6.6f**).

Critical for practical deployment, the R-PCEC demonstrated flawless reversibility across 18 cycles (180 hours) when alternating between EC ($-0.40\ A \cdot cm^{-2}$) and FC ($0.32\ A \cdot cm^{-2}$) modes at 550°C (**Figure 6.6g**). This cyclic stability—uncharacteristic of conventional electrodes—originates from the F6 electrode's electrochemical stability, structural integrity, and exceptional electrolyte compatibility. Collectively, these results position the F6 dual-phase nanocomposite as a promising air electrode catalyst for R-PCECs, achieving unprecedented bifunctional activity (ORR/OER) and durability under realistic operating conditions.

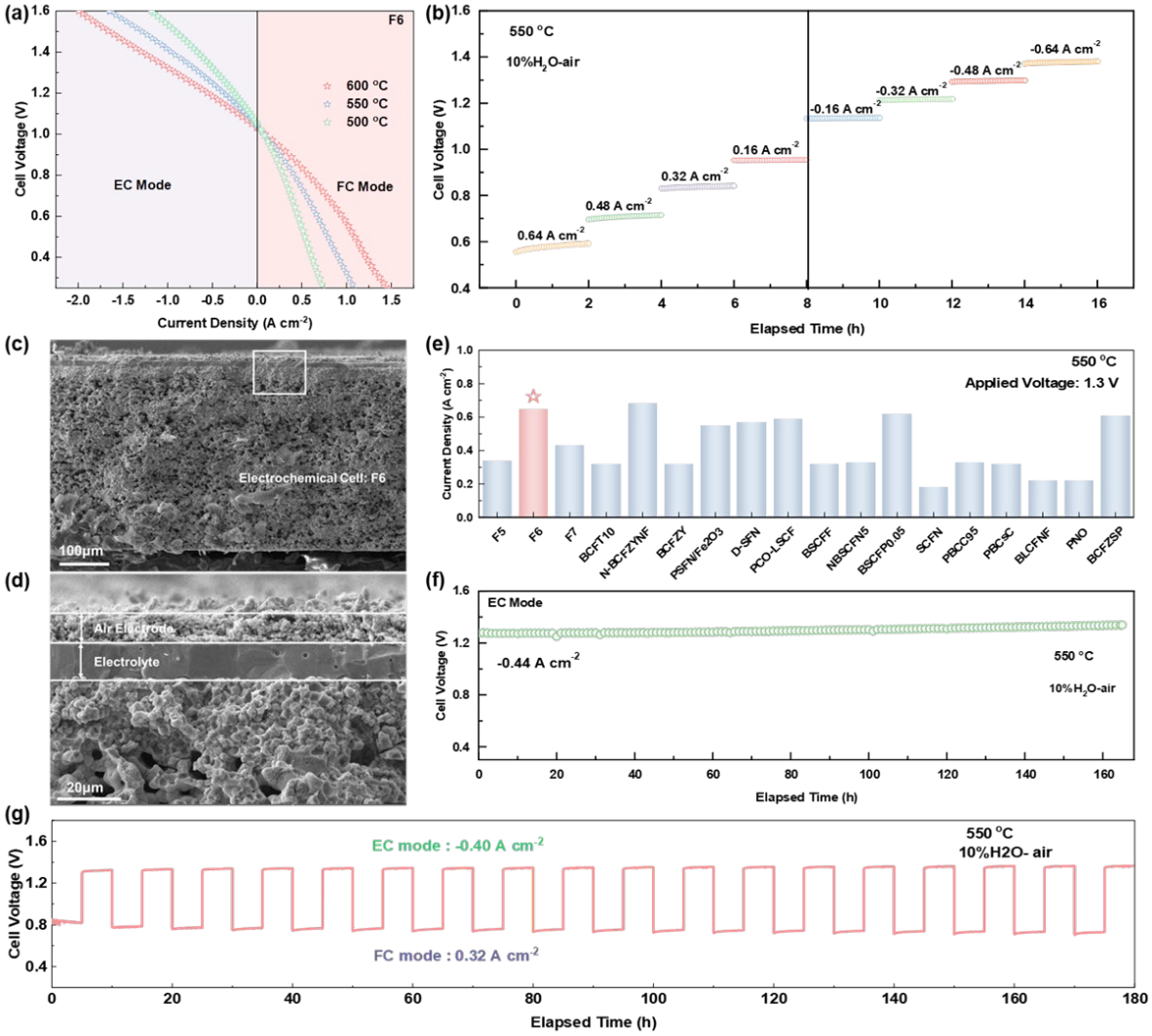

Figure 6.6 (a) i-V characteristics of the F6-based R-PCEC operating in FC and EC modes at 500-600 °C; (b) Stability tests under varying current densities (+: FC mode, −: EC mode); Cross-sectional SEM image of the R-PCEC after stability test: (c) the whole cell and (d) the electrode-electrolyte interface; (e) Comparative electrolysis current densities at 550 °C (1.3 V applied bias) for the F6 air electrode against state-of-the-art proton-conducting air electrodes; (f) Durability test under constant electrolysis current density (−0.44 A·cm^{-2}) at 550 °C; (g) Long-term durability of the R-PCEC under cyclic operation alternating between electrolysis (−0.40 A·cm^{-2}) and fuel cell (+0.32 A·cm^{-2}) modes at 550 °C.

6.3 Conclusion

This study developed a novel nanocomposite air electrode, $Ba(Zr_{0.1}Ce_{0.7}Y_{0.1}Yb_{0.1})_{0.4}Fe_{0.6}F_{0.1}O_{2.9-\delta}$ (F6), through the integration of one-pot in situ bulk-phase self-assembly and anion engineering strategies. The F6 electrode exhibits exceptional steam resistance, thermomechanical compatibility, and high ORR/OER catalytic

activity/stability. Experimental results demonstrate that in situ bulk-phase self-assembly generates a nanoscale dual-phase architecture comprising a triple-conducting primary phase and a proton-conductive secondary phase, which collectively establish continuous proton absorption/transport pathways to significantly enhance proton conductivity. Concurrently, the incorporation of electronegative F^- anions weaken metal-oxygen bonds across both phases, markedly improving surface oxygen exchange kinetics and bulk oxygen-ion transport. These attributes synergistically endow the electrode with superior triple conductivity. The exclusion of Co/Sr cations, coupled with tightly interlocked dual-phase nanostructures, confers robust hydration resistance and thermal expansion matching with proton-conducting electrolytes.

Consequently, the F6 electrode achieves remarkable catalytic performance, exhibiting an ultra-low ASR of 0.33 $\Omega \cdot cm^2$ at 550 °C—surpassing most state-of-the-art air electrodes. Notably, it delivers a PPD value of 0.494 $W \cdot cm^{-2}$ in FC mode and an exceptional electrolysis current density of 0.649 $A \cdot cm^{-2}$ at 1.3 V in EC mode. Long-term cyclic operation tests (180 hours) under alternating current densities in 10% humidified air further validate its operational durability and adaptability as an R-PCEC air electrode. These findings position F6 as a promising nanocomposite bifunctional catalyst capable of stable, reversible operation under fluctuating thermal and humidified conditions. The synergistic combination of in situ bulk-phase self-assembly and anion engineering presented herein establishes a rational design paradigm for advanced energy materials, offering transformative potential for high-performance energy storage and conversion devices.

CHAPTER 7 Conclusions and Suggestions for Future Research

7.1 Conclusions

This study focuses on developing high-performance triple-conducting air electrodes for R-PCECs, addressing critical limitations in catalytic activity and stability through three systematically engineered strategies rooted in electrode reaction mechanisms, material physicochemical properties, charge carrier kinetics, and operational demands.

First, we pioneered an anion engineering approach by substituting electronegative F^- and Cl^- anions into the oxygen sublattice of the mixed ionic-electronic conductor BSCF. This strategic modification weakened metal-oxygen bonds within the perovskite lattice, yielding the optimized BSCFF air electrode, which demonstrated markedly enhanced ORR/OER activity due to facilitated bulk triple conductivity.

Subsequently, leveraging the bond-weakening effects of anion engineering, we developed a dual-optimization strategy that synergistically tailors bulk metal-oxygen bond strength and surface catalytic activity. By in-situ exsolving metal oxide nano-catalysts (NiO) on the surface and incorporating F anions into the bulk phase, we successfully synthesized the nanocomposite electrode N-BCFZYNF. This architecture simultaneously enhanced bulk oxygen-ion mobility and surface reaction kinetics, achieving superior bifunctional catalytic performance under operational R-PCEC conditions.

Finally, recognizing the imperative for steam resistance and thermomechanical compatibility in practical applications, we innovated a one-pot in-situ bulk-phase self-assembly strategy integrated with anion engineering. This approach generated a nanoscale dual-phase architecture comprising: A triple-conducting major phase (M-BZCYYFF) ensuring rapid

$H^+/O^{2-}/e^-$ transport, and a proton-conductive secondary phase (P-BZCYYFF) which chemically akin to state-of-the-art electrolytes (BZCYYb), establishing continuous proton absorption/transport pathways. Moreover, the exclusion of Co/Sr cations eliminated phase segregation risks, while electronegative F^- doping weakened interatomic bonds across both phases, enhancing ionic mobility. Crucially, the interlocked nanostructure conferred exceptional steam resistance and thermal expansion, addressing long-term stability challenges in conventional single-phase or surface-decorated electrodes.

Collectively, these strategies establish a transformative framework for designing R-PCEC air electrodes that integrating high catalytic activity, triple conductivity, and operational durability—critical advancements toward intermediate-temperature solid oxide electrochemical cells and other energy storage and conversion devices.

7.2 Suggestions for Future Research

Despite advancements in triple-conducting bifunctional air electrodes for R-PCECs, critical challenges still persist, including (1) the competing proton and oxygen-ion transport mechanisms that hinder simultaneous optimization of both processes; (2) the trade-off between hydration capacity and structural stability under high steam pressures; (3) insufficient durability testing durations compared to practical benchmarks (>0.2% per 1000h); (4) performance compromises in iron-based systems, which reduce costs and thermal expansion but often sacrifice catalytic activity; and (5) limited electrochemical performance at low-temperature (<400 °C), thus hindering R-PCECs' commercialization process.

To address these challenges, multi-dimensional strategies integrating computational and experimental tools are necessary to be applied. Specifically, machine learning, DFT and

multiphysics modeling should be widely applied to underscore the intrinsic material properties (e.g., oxygen vacancy formation energies, proton migration barriers) and the rate-limiting steps of air electrodes reactions.

Despite these challenges, the development of air electrode materials has made significant progress over the past several decades, and their future potential is promising. In the future, synergizing advanced modification techniques (e.g., anion engineering, dual-phase architecture) with validated computational frameworks is more promising. In this way, next-generation air electrodes hold potential to achieve balanced triple conductivity, hydration resistance, and thermomechanical stability—essential for commercializing durable, low-temperature R-PCECs energy conversion and storage device.

References

[1] Ruhnau, O.; Stiewe, C.; Muessel, J.; Hirth, L., Natural gas savings in Germany during the 2022 energy crisis. *Nat. Energy* **2023,** *8* (6), 621-628.

[2] Su, C.-W.; Pang, L.-D.; Qin, M.; Lobonţ, O.-R.; Umar, M., The spillover effects among fossil fuel, renewables and carbon markets: Evidence under the dual dilemma of climate change and energy crises. *Energy* **2023,** *274*, 127304.

[3] Wei, Y.-M.; Chen, K.; Kang, J.-N.; Chen, W.; Wang, X.-Y.; Zhang, X., Policy and Management of Carbon Peaking and Carbon Neutrality: A Literature Review. *Engineering* **2022,** *14*, 52-63.

[4] Dannenberg, A.; Lumkowsky, M.; Carlton, E. K.; Victor, D. G., Naming and shaming as a strategy for enforcing the Paris Agreement: The role of political institutions and public concern. *Proc. Natl. Acad. Sci.* **2023,** *120* (40), e2305075120.

[5] Vezzoni, R., Green growth for whom, how and why? The REPowerEU Plan and the inconsistencies of European Union energy policy. *Energy Res. Social Sci.* **2023,** *101*, 103134.

[6] Bistline, J.; Blanford, G.; Brown, M.; Burtraw, D.; Domeshek, M.; Farbes, J.; Fawcett, A.; Hamilton, A.; Jenkins, J.; Jones, R.; King, B.; Kolus, H.; Larsen, J.; Levin, A.; Mahajan, M.; Marcy, C.; Mayfield, E.; McFarland, J.; McJeon, H.; Orvis, R.; Patankar, N.; Rennert, K.; Roney, C.; Roy, N.; Schivley, G.; Steinberg, D.; Victor, N.; Wenzel, S.; Weyant, J.; Wiser, R.; Yuan, M.; Zhao, A., Emissions and energy impacts of the Inflation Reduction Act. *Science* **2023,** *380* (6652), 1324-1327.

[7] Achakulwisut, P.; Erickson, P.; Guivarch, C.; Schaeffer, R.; Brutschin, E.; Pye, S., Global fossil fuel reduction pathways under different climate mitigation strategies and ambitions. *Nat. Commun.* **2023,** *14* (1), 5425.

[8] Kim, D.; Bae, K. T.; Kim, K. J.; Im, H.-N.; Jang, S.; Oh, S.; Lee, S. W.; Shin, T. H.; Lee, K. T., High-Performance Protonic Ceramic Electrochemical Cells. *ACS Energy Lett.* **2022,** *7* (7), 2393-2400.

[9] Liu, F.; Ding, D.; Duan, C., Protonic Ceramic Electrochemical Cells for Synthesizing Sustainable Chemicals and Fuels. *Adv. Sci.* **2023,** *10* (8), 2206478.

[10] Zhang, H.; Xu, K.; He, F.; Zhou, Y.; Sasaki, K.; Zhao, B.; Choi, Y.; Liu, M.; Chen, Y., Surface Regulating of a Double-Perovskite Electrode for Protonic Ceramic Fuel Cells to Enhance Oxygen Reduction Activity and Contaminants Poisoning Tolerance. *Adv. Energy Mater.* **2022,** *12* (26), 2200761.

[11] He, F.; Wu, T.; Peng, R.; Xia, C., Cathode reaction models and performance analysis of $Sm_{0.5}Sr_{0.5}CoO_{3-\delta}$–$BaCe_{0.8}Sm_{0.2}O_{3-\delta}$ composite cathode for solid oxide fuel cells with proton conducting electrolyte. *J. Power Sources* **2009,** *194* (1), 263-268.

[12] Wang, M.; Su, C.; Zhu, Z.; Wang, H.; Ge, L., Composite cathodes for protonic ceramic fuel cells: Rationales and materials. *Composites, Part B* **2022,** *238*, 109881.

[13] Papac, M.; Stevanović, V.; Zakutayev, A.; O'Hayre, R., Triple ionic–electronic conducting oxides for next-generation electrochemical devices. *Nat. Mater.* **2021,** *20* (3), 301-313.

[14] Lu, L.; Liu, Y.; Zhang, H.; Xu, Y.; Chen, H., Exploring the potential of triple conducting perovskite cathodes for high-performance solid oxide fuel cells: a comprehensive review. *J. Mater. Chem. A* **2023,** *11* (44), 23613-23639.

[15] Hanif, M. B.; Rauf, S.; ul Abadeen, Z.; Khan, K.; Tayyab, Z.; Qayyum, S.; Mosiałek, M.; Shao, Z.; Li, C.-X.; Motola, M. J. M., Proton-conducting solid oxide electrolysis cells: Relationship of composition-structure-property, their challenges, and prospects. *Matter* **2023,** *6* (6), 1782-1830.
[16] Li, S.; Irvine, J. S., Non-stoichiometry, structure and properties of proton-conducting perovskite oxides. *Solid State Ionics* **2021,** *361*, 115571.
[17] Wang, N.; Hinokuma, S.; Ina, T.; Toriumi, H.; Katayama, M.; Inada, Y.; Zhu, C.; Habazaki, H.; Aoki, Y., Incorporation of bulk proton carriers in cubic perovskite manganite driven by interplays of oxygen and manganese redox. *Chem. Mater.* **2019,** *31* (20), 8383-8393.
[18] Ueki, T.; Watanabe, M., Macromolecules in ionic liquids: progress, challenges, and opportunities. *Macromolecules* **2008,** *41* (11), 3739-3749.
[19] Jing, Y.; Aluru, N. R., The role of A-site ion on proton diffusion in perovskite oxides (ABO_3). *J. Power Sources* **2020,** *445*, 227327.
[20] Kreuer, K.-D.; Rabenau, A.; Weppner, W., Vehicle mechanism, a new model for the interpretation of the conductivity of fast proton conductors. *Angew. Chem., Int. Ed.* **1982,** *21* (3), 208-209.
[21] Kim, J.; Sengodan, S.; Kim, S.; Kwon, O.; Bu, Y.; Kim, G., Proton conducting oxides: A review of materials and applications for renewable energy conversion and storage. *Renewable Sustainable Energy Rev.* **2019,** *109*, 606-618.
[22] Wang, Z.; Yang, W.; Zhu, Z.; Peng, R.; Wu, X.; Xia, C.; Lu, Y., First-principles study of O_2 reduction on $BaZr_{1-x}Co_xO_3$ cathodes in protonic-solid oxide fuel cells. *J. Mater. Chem. A* **2014,** *2* (39), 16707-16714.
[23] Muñoz-García, A. B.; Pavone, M., First-Principles Design of New Electrodes for Proton-Conducting Solid-Oxide Electrochemical Cells: A-Site Doped $Sr_2Fe_{1.5}Mo_{0.5}O_{6-\delta}$ Perovskite. *Chem. Mater.* **2016,** *28* (2), 490-500.
[24] Lan, C.; Li, H.; Zhao, S., A first-principles study of the proton and oxygen migration behavior in the rare-earth perovskite $SmNiO_3$. *J. Comput. Electron.* **2020,** *19* (3), 905-909.
[25] Ding, H.; Wu, W.; Jiang, C.; Ding, Y.; Bian, W.; Hu, B.; Singh, P.; Orme, C. J.; Wang, L.; Zhang, Y.; Ding, D., Self-sustainable protonic ceramic electrochemical cells using a triple conducting electrode for hydrogen and power production. *Nat. Commun.* **2020,** *11* (1), 1907.
[26] Xu, X.; Wang, H.; Ma, J.; Liu, W.; Wang, X.; Fronzi, M.; Bi, L., Impressive performance of proton-conducting solid oxide fuel cells using a first-generation cathode with tailored cations. *J. Mater. Chem. A* **2019,** *7* (32), 18792-18798.
[27] Yashima, M.; Tsujiguchi, T.; Sakuda, Y.; Yasui, Y.; Zhou, Y.; Fujii, K.; Torii, S.; Kamiyama, T.; Skinner, S. J., High oxide-ion conductivity through the interstitial oxygen site in $Ba_7Nb_4MoO_{20}$-based hexagonal perovskite related oxides. *Nat. Commun.* **2021,** *12* (1), 556.
[28] Schuett, J.; Schultze, T. K.; Grieshammer, S., Oxygen Ion Migration and Conductivity in $LaSrGa_3O_7$ Melilites from First Principles. *Chem. Mater.* **2020,** *32* (11), 4442-4450.
[29] Kim, J.-H.; Manthiram, A., Layered $LnBaCo_2O_{5+\delta}$ perovskite cathodes for solid oxide fuel cells: an overview and perspective. *J. Mater. Chem. A* **2015,** *3* (48), 24195-24210.
[30] Bernuy-Lopez, C.; Rioja-Monllor, L.; Nakamura, T.; Ricote, S.; O'Hayre, R.; Amezawa, K.; Einarsrud, M.-A.; Grande, T., Effect of cation ordering on the performance and chemical stability of layered double perovskite cathodes. *Materials* **2018,** *11* (2), 196.
[31] Xu, X.; Pan, Y.; Zhong, Y.; Ran, R.; Shao, Z., Ruddlesden–Popper perovskites in

electrocatalysis. *Mater. Horiz.* **2020,** *7* (10), 2519-2565.
[32] Zhang, W.; Zhang, X.; Song, Y.; Wang, G., Recent progress on cathode materials for protonic ceramic fuel cells. *Next Sustainability* **2024,** *3*, 100028.
[33] Amow, G.; Davidson, I. J.; Skinner, S. J., A comparative study of the Ruddlesden-Popper series, $La_{n+1}Ni_nO_{3n+1}$ (n=1, 2 and 3), for solid-oxide fuel-cell cathode applications. *Solid State Ionics* **2006,** *177* (13), 1205-1210.
[34] Han, D.; Okumura, Y.; Nose, Y.; Uda, T., Synthesis of $La_{1-x}Sr_xSc_{1-y}Fe_yO_{3-\delta}$ (LSSF) and measurement of water content in LSSF, LSCF and LSC hydrated in wet artificial air at 300° C. *Solid State Ionics* **2010,** *181* (35-36), 1601-1606.
[35] Hashimoto, D.; Han, D.; Uda, T., Dependence of lattice constant of Ba, Co-contained perovskite oxides on atmosphere, and measurements of water content. *Solid State Ionics* **2014,** *262*, 687-690.
[36] Poetzsch, D.; Merkle, R.; Maier, J., Proton uptake in the H^+-SOFC cathode material $Ba_{0.5}Sr_{0.5}Fe_{0.8}Zn_{0.2}O_{3-\delta}$: transition from hydration to hydrogenation with increasing oxygen partial pressure. *Faraday Discuss.* **2015,** *182* (0), 129-143.
[37] Zohourian, R.; Merkle, R.; Raimondi, G.; Maier, J., Mixed-conducting perovskites as cathode materials for protonic ceramic fuel cells: understanding the trends in proton uptake. *Adv. Funct. Mater.* **2018,** *28* (35), 1801241.
[38] Poetzsch, D.; Merkle, R.; Maier, J., Proton conductivity in mixed-conducting BSFZ perovskite from thermogravimetric relaxation. *Phys Chem Chem Phys* **2014,** *16* (31), 16446-16453.
[39] Tong, J.; Yang, W.; Zhu, B.; Cai, R., Investigation of ideal zirconium-doped perovskite-type ceramic membrane materials for oxygen separation. *J. Membr. Sci.* **2002,** *203* (1), 175-189.
[40] Shang, M.; Tong, J.; O'Hayre, R., A promising cathode for intermediate temperature protonic ceramic fuel cells: $BaCo_{0.4}Fe_{0.4}Zr_{0.2}O_{3-\delta}$. *RSC Adv.* **2013,** *3* (36), 15769-15775.
[41] Duan, C.; Tong, J.; Shang, M.; Nikodemski, S.; Sanders, M.; Ricote, S.; Almansoori, A.; O'Hayre, R., Readily processed protonic ceramic fuel cells with high performance at low temperatures. *Science* **2015,** *349* (6254), 1321-1326.
[42] Duffy, J. H.; Abernathy, H. W.; Brinkman, K. S., Tuning proton kinetics in $BaCo_{0.4}Fe_{0.4}Zr_{0.2-X}Y_XO_{3-\delta}$ triple ionic-electronic conductors via aliovalent substitution. *J. Mater. Chem. A* **2023,** *11* (16), 8929-8938.
[43] Ren, R.; Wang, Z.; Xu, C.; Sun, W.; Qiao, J.; Rooney, D. W.; Sun, K., Tuning the defects of the triple conducting oxide $BaCo_{0.4}Fe_{0.4}Zr_{0.1}Y_{0.1}O_{3-\delta}$ perovskite toward enhanced cathode activity of protonic ceramic fuel cells. *J. Mater. Chem. A* **2019,** *7* (31), 18365-18372.
[44] Liang, M.; He, F.; Zhou, C.; Chen, Y.; Ran, R.; Yang, G.; Zhou, W.; Shao, Z., Nickel-doped $BaCo_{0.4}Fe_{0.4}Zr_{0.1}Y_{0.1}O_{3-\delta}$ as a new high-performance cathode for both oxygen-ion and proton conducting fuel cells. *Chem. Eng. J.* **2021,** *420*, 127717.
[45] Liang, M.; Song, Y.; Liu, D.; Xu, L.; Xu, M.; Yang, G.; Wang, W.; Zhou, W.; Ran, R.; Shao, Z., Magnesium tuned triple conductivity and bifunctionality of $BaCo_{0.4}Fe_{0.4}Zr_{0.1}Y_{0.1}O_{3-\delta}$ perovskite towards reversible protonic ceramic electrochemical cells. *Appl. Catal., B* **2022,** *318*, 121868.
[46] Xu, Y.; Hu, F.; Guo, Y.; Zhang, J.; Huang, Y.; Zhou, W.; Sun, J.; He, B.; Zhao, L., Probing oxygen reduction and water uptake kinetics of $BaCo_{0.4}Fe_{0.4}Zr_{0.1}Y_{0.1-x}Zn_xO_{3-\delta}$ cathodes

for protonic ceramic fuel cells. *Sep. Purif. Technol.* **2022,** *297*, 121482.
[47] Choi, S.; Yoo, S.; Kim, J.; Park, S.; Jun, A.; Sengodan, S.; Kim, J.; Shin, J.; Jeong, H. Y.; Choi, Y.; Kim, G.; Liu, M., Highly efficient and robust cathode materials for low-temperature solid oxide fuel cells: $PrBa_{0.5}Sr_{0.5}Co_{2-x}Fe_xO_{5+\delta}$. *Sci. Rep.* **2013,** *3* (1), 2426.
[48] Grimaud, A.; Mauvy, F.; Bassat, J. M.; Fourcade, S.; Rocheron, L.; Marrony, M.; Grenier, J. C., Hydration Properties and Rate Determining Steps of the Oxygen Reduction Reaction of Perovskite-Related Oxides as H^+-SOFC Cathodes. *J. Electrochem. Soc.* **2012,** *159* (6), B683.
[49] Kim, J.; Sengodan, S.; Kwon, G.; Ding, D.; Shin, J.; Liu, M.; Kim, G., Triple-Conducting Layered Perovskites as Cathode Materials for Proton-Conducting Solid Oxide Fuel Cells. *ChemSusChem* **2014,** *7* (10), 2811-2815.
[50] Choi, S.; Kucharczyk, C. J.; Liang, Y.; Zhang, X.; Takeuchi, I.; Ji, H.-I.; Haile, S. M., Exceptional power density and stability at intermediate temperatures in protonic ceramic fuel cells. *Nat. Energy* **2018,** *3* (3), 202-210.
[51] Im, S.; Berk, M. A.; Yang, S.; Kim, B.-K.; Yoon, K. J.; Son, J.-W.; Lee, J.-H.; Ji, H.-I., The proton uptake process in double perovskite triple ionic-electronic conducting oxides for protonic ceramic cells. *J. Mater. Chem. A* **2022,** *10* (30), 16127-16136.
[52] Seong, A.; Kim, J.; Jeong, D.; Sengodan, S.; Liu, M.; Choi, S.; Kim, G., Electrokinetic Proton Transport in Triple ($H^+/O^{2-}/e^-$) Conducting Oxides as a Key Descriptor for Highly Efficient Protonic Ceramic Fuel Cells. *Adv. Sci.* **2021,** *8* (11), 2004099.
[53] Yashima, M.; Enoki, M.; Wakita, T.; Ali, R.; Matsushita, Y.; Izumi, F.; Ishihara, T., Structural disorder and diffusional pathway of oxide ions in a doped Pr2NiO4-based mixed conductor. *J. Am. Chem. Soc.* **2008,** *130* (9), 2762-2763.
[54] Chroneos, A.; Parfitt, D.; Kilner, J. A.; Grimes, R. W., Anisotropic oxygen diffusion in tetragonal $La_2NiO_{4+\delta}$: Molecular dynamics calculations. *J. Mater. Chem.* **2010,** *20* (2), 266-270.
[55] Halat, D. M.; Dervişoğlu, R.; Kim, G.; Dunstan, M. T.; Blanc, F.; Middlemiss, D. S.; Grey, C. P., Probing oxide-ion mobility in the mixed ionic–electronic conductor $La_2NiO_{4+\delta}$ by solid-state 17O MAS NMR spectroscopy. *J. Am. Chem. Soc.* **2016,** *138* (36), 11958-11969.
[56] Li, X.; Benedek, N. A., Enhancement of ionic transport in complex oxides through soft lattice modes and epitaxial strain. *Chem. Mater.* **2015,** *27* (7), 2647-2652.
[57] Grimaud, A.; Mauvy, F.; Marc Bassat, J.; Fourcade, S.; Marrony, M.; Claude Grenier, J., Hydration and transport properties of the $Pr_{2-x}Sr_xNiO_{4+\delta}$ compounds as H^+-SOFC cathodes. *J. Mater. Chem.* **2012,** *22* (31), 16017-16025.
[58] An, H.; Shin, D.; Ji, H.-I., $Pr_2NiO_{4+\delta}$ for Cathode in Protonic Ceramic Fuel Cells. *J. Korean Ceram. Soc* **2018,** *55* (4), 358-363.
[59] Yang, S.; Wen, Y.; Zhang, J.; Lu, Y.; Ye, X.; Wen, Z., Electrochemical performance and stability of cobalt-free $Ln_{1.2}Sr_{0.8}NiO_4$ (Ln=La and Pr) air electrodes for proton-conducting reversible solid oxide cells. *Electrochim. Acta* **2018,** *267*, 269-277.
[60] Miao, L.; Hou, J.; Gong, Z.; Jin, Z.; Liu, W., A high-performance cobalt-free Ruddlesden-Popper phase cathode $La_{1.2}Sr_{0.8}Ni_{0.6}Fe_{0.4}O_{4+\delta}$ for low temperature proton-conducting solid oxide fuel cells. *Int. J. Hydrogen Energy* **2019,** *44* (14), 7531-7537.
[61] Beznosikov, B. V.; Aleksandrov, K. S., Perovskite-like crystals of the Ruddlesden-Popper series. *Crystallogr. Rep.* **2000,** *45* (5), 792-798.
[62] Yang, G.; Jung, W.; Ahn, S.-J.; Lee, D., Controlling the Oxygen Electrocatalysis on Perovskite and Layered Oxide Thin Films for Solid Oxide Fuel Cell Cathodes. *Appl. Sci.* **2019,**

9 (5), 1030.
[63] Zhang, L.; Yao, F.; Meng, J.; Zhang, W.; Wang, H.; Liu, X.; Meng, J.; Zhang, H., Oxygen migration and proton diffusivity in transition-metal (Mn, Fe, Co, and Cu) doped Ruddlesden–Popper oxides. *J. Mater. Chem. A* **2019,** *7* (31), 18558-18567.
[64] Wang, Q.; Hou, J.; Fan, Y.; Xi, X.; Li, J.; Lu, Y.; Huo, G.; Shao, L.; Fu, X.; Luo, J., $Pr_2BaNiMnO_{7-\delta}$ double-layered Ruddlesden–Popper perovskite oxides as efficient cathode electrocatalysts for low temperature proton conducting solid oxide fuel cells. *J. Mater. Chem. A* **2020,** *8* (16), 7704-7712.
[65] Amow, G.; Skinner, S., Recent developments in Ruddlesden–Popper nickelate systems for solid oxide fuel cell cathodes. *J. Solid State Electrochem.* **2006,** *10*, 538-546.
[66] Matvejeff, M.; Lehtimäki, M.; Hirasa, A.; Huang, Y. H.; Yamauchi, H.; Karppinen, M., New Water-Containing Phase Derived from the Sr3Fe2O7-δ Phase of the Ruddlesden−Popper Structure. *Chem. Mater.* **2005,** *17* (10), 2775-2779.
[67] Wang, Z.; Yang, W.; Shafi, S. P.; Bi, L.; Wang, Z.; Peng, R.; Xia, C.; Liu, W.; Lu, Y., A high performance cathode for proton conducting solid oxide fuel cells. *J. Mater. Chem. A* **2015,** *3* (16), 8405-8412.
[68] Huan, D.; Shi, N.; Zhang, L.; Tan, W.; Xie, Y.; Wang, W.; Xia, C.; Peng, R.; Lu, Y., New, Efficient, and Reliable Air Electrode Material for Proton-Conducting Reversible Solid Oxide Cells. *ACS Appl. Mater. Interfaces* **2018,** *10* (2), 1761-1770.
[69] Yu, N.; Bello, I. T.; Chen, X.; Liu, T.; Li, Z.; Song, Y.; Ni, M., Rational Design of Ruddlesden–Popper Perovskite Ferrites as Air Electrode for Highly Active and Durable Reversible Protonic Ceramic Cells. *Nano-Micro Lett.* **2024,** *16* (1), 177.
[70] Huan, D.; Zhang, L.; Li, X.; Xie, Y.; Shi, N.; Xue, S.; Xia, C.; Peng, R.; Lu, Y., A durable ruddlesden-popper cathode for protonic ceramic fuel cells. *ChemSusChem* **2020,** *13* (18), 4994-5003.
[71] Wu, T.; Peng, R.; Xia, C., $Sm_{0.5}Sr_{0.5}CoO_{3-\delta}$–$BaCe_{0.8}Sm_{0.2}O_{3-\delta}$ composite cathodes for proton-conducting solid oxide fuel cells. *Solid State Ionics* **2008,** *179* (27-32), 1505-1508.
[72] Ding, H.; Lin, B.; Liu, X.; Meng, G., High performance protonic ceramic membrane fuel cells (PCMFCs) with $Ba_{0.5}Sr_{0.5}Zn_{0.2}Fe_{0.8}O_{3-\delta}$ perovskite cathode. *Electrochem. Commun.* **2008,** *10* (9), 1388-1391.
[73] Dai, H.; Da'as, E. H.; Shafi, S. P.; Wang, H.; Bi, L., Tailoring cathode composite boosts the performance of proton-conducting SOFCs fabricated by a one-step co-firing method. *J. Eur. Ceram. Soc.* **2018,** *38* (7), 2903-2908.
[74] Yang, L.; Zuo, C.; Wang, S.; Cheng, Z.; Liu, M., A novel composite cathode for low-temperature SOFCs based on oxide proton conductors. *Adv. Mater.* **2008,** *20* (17), 3280-3283.
[75] Cui, J.; Wang, J.; Zhang, X.; Li, G.; Wu, K.; Cheng, Y.; Zhou, J., Enhanced oxygen reduction reaction through Ca and Co Co-doped $YFeO_3$ as cathode for protonic ceramic fuel cells. *J. Power Sources* **2019,** *413*, 148-157.
[76] Fabbri, E.; Licoccia, S.; Traversa, E.; Wachsman, E. D., Composite Cathodes for Proton Conducting Electrolytes. *Fuel Cells* **2009,** *9* (2), 128-138.
[77] Yoo, C.-Y.; Yun, D. S.; Park, S.-Y.; Park, J.; Joo, J. H.; Park, H.; Kwak, M.; Yu, J. H., Investigation of Electrochemical Properties of Model Lanthanum Strontium Cobalt Ferrite-Based Cathodes for Proton Ceramic Fuel Cells. *Electrocatalysis* **2016,** *7* (4), 280-286.

[78] Yang, L.; Liu, Z.; Wang, S.; Choi, Y.; Zuo, C.; Liu, M., A mixed proton, oxygen ion, and electron conducting cathode for SOFCs based on oxide proton conductors. *J. Power Sources* **2010,** *195* (2), 471-474.
[79] Watanabe, K.; Yamaguchi, Y.; Nomura, K.; Sumi, H.; Mori, M.; Mizutani, Y.; Shimada, H., Effect of cobalt content on electrochemical performance for $La_{0.6}Sr_{0.4}Co_xFe_{1-x}O_{3-\delta}$ and $BaZr_{0.8}Yb_{0.2}O_{3-\delta}$ composite cathodes in protonic ceramic fuel cells. *Ceram. Int.* **2023,** *49* (12), 21085-21090.
[80] Zhou, W.; Ran, R.; Shao, Z., Progress in understanding and development of $Ba_{0.5}Sr_{0.5}Co_{0.8}Fe_{0.2}O_{3-\delta}$-based cathodes for intermediate-temperature solid-oxide fuel cells: a review. *J. Power Sources* **2009,** *192* (2), 231-246.
[81] Taillades, G.; Pers, P.; Mao, V.; Taillades, M., High performance anode-supported proton ceramic fuel cell elaborated by wet powder spraying. *Int. J. Hydrogen Energy* **2016,** *41* (28), 12330-12336.
[82] Seo, J.; Kim, H.-W.; Yu, J. H.; Park, H. J., Electrochemical properties of $Ba_{0.5}Sr_{0.5}Co_{0.8}Fe_{0.2}O_3$ and $BaZr_{0.65}Ce_{0.20}Y_{0.15}O_3$ composite cathodes on Y-doped barium–cerium–zirconium oxide solid electrolyte. *J. Korean Ceram. Soc.* **2022,** *59* (2), 217-223.
[83] Liu, B.; Yang, J.; Yan, D.; Jia, L.; Chi, B.; Pu, J.; Li, J., Novel $PrBa_{0.9}Ca_{0.1}Co_{2-x}Zn_xO_{5+\delta}$ double-perovskite as an active cathode material for high-performance proton-conducting solid oxide fuel cells. *Int. J. Hydrogen Energy* **2020,** *45* (55), 31009-31016.
[84] Chen, J.; Li, J.; Jia, L.; Moussa, I.; Chi, B.; Pu, J.; Li, J., A novel layered perovskite $Nd(Ba_{0.4}Sr_{0.4}Ca_{0.2})Co_{1.6}Fe_{0.4}O_{5+\delta}$ as cathode for proton-conducting solid oxide fuel cells. *J. Power Sources* **2019,** *428*, 13-19.
[85] Li, M.; Ni, M.; Su, F.; Xia, C., Proton conducting intermediate-temperature solid oxide fuel cells using new perovskite type cathodes. *J. Power Sources* **2014,** *260*, 197-204.
[86] Li, W.; Guan, B.; Ma, L.; Hu, S.; Zhang, N.; Liu, X., High performing triple-conductive $Pr_2NiO_{4+\delta}$ anode for proton-conducting steam solid oxide electrolysis cell. *J. Mater. Chem. A* **2018,** *6* (37), 18057-18066.
[87] Tarutin, A. P.; Lyagaeva, J. G.; Farlenkov, A. S.; Vylkov, A. I.; Medvedev, D. M., Cu-substituted $La_2NiO_{4+\delta}$ as oxygen electrodes for protonic ceramic electrochemical cells. *Ceram. Int.* **2019,** *45* (13), 16105-16112.
[88] Bu, Y.; Joo, S.; Zhang, Y.; Wang, Y.; Meng, D.; Ge, X.; Kim, G., A highly efficient composite cathode for proton-conducting solid oxide fuel cells. *J. Power Sources* **2020,** *451*, 227812.
[89] Zhou, H.; Yi, X.; Hui, Y.; Wang, L.; Chen, W.; Qin, Y.; Wang, M.; Ma, J.; Chu, X.; Wang, Y.; Hong, X.; Chen, Z.; Meng, X.; Wang, H.; Zhu, Q.; Song, L.; Zheng, A.; Xiao, F.-S., Isolated boron in zeolite for oxidative dehydrogenation of propane. *Science* **2021,** *372* (6537), 76-80.
[90] Li, X.; Chen, Z.; Huan, D.; Qiu, B.; Zhu, K.; Qi, Z.; Liu, H.; Xia, C.; Peng, R.; Lu, Y., Highly active cathode achieved by constructing surface proton acid sites through electronic regulation of heteroatoms. *ACS Mater. Lett.* **2023,** *5* (11), 2896-2905.
[91] Ding, D.; Li, X.; Lai, S. Y.; Gerdes, K.; Liu, M., Enhancing SOFC cathode performance by surface modification through infiltration. *Energy Environ. Sci.* **2014,** *7* (2), 552-575.
[92] Wang, Q.; Ricote, S.; Chen, M., Oxygen electrodes for protonic ceramic cells. *Electrochim. Acta* **2023,** *446*, 142101.

[93] Connor, P.; Yue, X.; Savaniu, C.; Price, R.; Triantafyllou, G.; Cassidy, M.; Kerherve, G.; Payne, D.; Maher, R.; Cohen, L.; Tomov, R.; Glowacki, B. A.; Kumar, R.; Irvine, J. S., Tailoring SOFC electrode microstructures for improved performance. *Adv. Energy Mater.* **2018,** *8* (23), 1800120.
[94] Bausá, N.; Serra, J. M., Robust catalytically-activated LSM-BCZY-based composite steam electrodes for proton ceramic electrolysis cells. *RSC Adv.* **2019,** *9* (36), 20677-20686.
[95] Pei, K.; Zhou, Y.; Ding, Y.; Xu, K.; Zhang, H.; Yuan, W.; Sasaki, K.; Choi, Y.; Liu, M.; Chen, Y., An improved oxygen reduction reaction activity and CO_2-tolerance of $La_{0.6}Sr_{0.4}Co_{0.2}Fe_{0.8}O_{3-\delta}$ achieved by a surface modification with barium cobaltite coatings. *J. Power Sources* **2021,** *514*, 230573.
[96] Pei, K.; Zhou, Y.; Xu, K.; He, Z.; Chen, Y.; Zhang, W.; Yoo, S.; Zhao, B.; Yuan, W.; Liu, M.; Chen, Y., Enhanced Cr-tolerance of an SOFC cathode by an efficient electro-catalyst coating. *Nano Energy* **2020,** *72*, 104704.
[97] Jing, J.; Lei, Z.; Wang, C.; Zheng, Z.; Wang, H.; Zhang, P.; Yang, Z.; Peng, S., Boosting performance of a protonic ceramic fuel cell by the incorporation of active nano-structured layers. *ACS Sustainable Chem. Eng.* **2023,** *11* (28), 10303-10310.
[98] Li, G.; Jin, H.; Cui, Y.; Gui, L.; He, B.; Zhao, L., Application of a novel $(Pr_{0.9}La_{0.1})_2(Ni_{0.74}Cu_{0.21}Nb_{0.05})O_{4+\delta}$-infiltrated $BaZr_{0.1}Ce_{0.7}Y_{0.2}O_{3-\delta}$ cathode for high performance protonic ceramic fuel cells. *J. Power Sources* **2017,** *341*, 192-198.
[99] Wang, Q.; Ricote, S.; Hendriksen, P. V.; Wang, Y.; Wang, J.; Chen, M., $Ba_{0.5}Gd_{0.8}La_{0.7}Co_2O_{6-\delta}$ Infiltrated $BaZr_{0.8}Y_{0.2}O_{3-\delta}$ composite oxygen electrodes for protonic ceramic electrolysis cells. *ECS Trans.* **2021,** *102* (5), 3.
[100] Wang, Q.; Tong, X.; Ricote, S.; Sažinas, R.; Hendriksen, P. V.; Chen, M., Nano-$LaCoO_3$ infiltrated $BaZr_{0.8}Y_{0.2}O_{3-\delta}$ electrodes for steam splitting in protonic ceramic electrolysis cells. *Adv. Powder Mater.* **2022,** *1* (1), 100003.
[101] Zhou, Y.; Zhang, W.; Kane, N.; Luo, Z.; Pei, K.; Sasaki, K.; Choi, Y.; Chen, Y.; Ding, D.; Liu, M., An efficient bifunctional air electrode for reversible protonic ceramic electrochemical cells. *Adv. Funct. Mater.* **2021,** *31* (40), 2105386.
[102] Niu, Y.; Zhou, Y.; Zhang, W.; Zhang, Y.; Evans, C.; Luo, Z.; Kane, N.; Ding, Y.; Chen, Y.; Guo, X.; Lv, W.; Liu, M., Highly active and durable air electrodes for reversible protonic ceramic electrochemical cells enabled by an efficient bifunctional catalyst. *Adv. Energy Mater.* **2022,** *12* (12), 2103783.
[103] Pei, K.; Luo, S.; He, F.; Arbiol, J.; Xu, Y.; Zhu, F.; Wang, Y.; Chen, Y., Constructing an active and stable oxygen electrode surface for reversible protonic ceramic electrochemical cells. *Appl. Catal., B* **2023,** *330*, 122601.
[104] Kim, Y.-M.; Chen, X.; Jiang, S. P.; Bae, J., Chromium Deposition and Poisoning at $Ba_{0.5}Sr_{0.5}Co_{0.8}Fe_{0.2}O_{3-\delta}$ Cathode of Solid Oxide Fuel Cells. *Electrochem. Solid-State Lett.* **2011,** *14* (4), B41.
[105] Zhang, W.; Muroyama, H.; Mikami, Y.; Matsui, T.; Eguchi, K., Surface manipulation of a triple-conducting cathode for protonic ceramic fuel cells to enhance oxygen reduction activity and CO_2 tolerance. *J. Energy Chem.* **2023,** *87*, 450-459.
[106] Qiu, P.; Yang, X.; Zhu, T.; Sun, S.; Jia, L.; Li, J., Review on core-shell structured cathode for intermediate temperature solid oxide fuel cells. *Int. J. Hydrogen Energy* **2020,** *45* (43), 23160-23173.

[107] Gao, Y.; Zhang, M.; Fu, M.; Hu, W.; Tong, H.; Tao, Z., A comprehensive review of recent progresses in cathode materials for Proton-conducting SOFCs. *Energy Reviews* **2023,** *2* (3), 100038.
[108] Ai, N.; Chen, K., A La0. 8Sr0. 2MnO3/La0. 6Sr0. 4Co0. 2Fe0. 8O3− δ core–shell structured cathode by a rapid sintering process for solid oxide fuel cells. *Int. J. Hydrog. Energy* **2017,** *42* (10), 7246-7251.
[109] Zhang, Z.; Wang, J.; Chen, Y.; Tan, S.; Shao, Z.; Chen, D., In situ formation of a 3D core-shell and triple-conducting oxygen reduction reaction electrode for proton-conducting SOFCs. *J. Power Sources* **2018,** *385*, 76-83.
[110] Li, J.; Liu, B.; Jia, L.; Chi, B.; Pu, J.; Li, J.; Wang, S., Investigation on the oxygen reduction reaction mechanism of PrBa0. 5Sr0. 5Co1. 5Fe0. 5O5+ δ@ La2NiO4+ δ core-shell structure cathode for solid oxide fuel cells. *Int. J. Hydrog. Energy* **2019,** *44* (48), 26489-26497.
[111] Zhang, W.; Hu, Y. H., Recent progress in design and fabrication of SOFC cathodes for efficient catalytic oxygen reduction. *Catal. Today* **2023,** *409*, 71-86.
[112] Geng, C.; Wu, H.; Yang, Y.; Wei, B.; Hong, T.; Cheng, J., A New In Situ Synthetic Triple-Conducting Core–Shell Electrode for Protonic Ceramic Fuel Cells. *ACS Sustainable Chem. Eng.* **2021,** *9* (33), 11070-11079.
[113] Lu, Y.; Yousaf Shah, M. A. K.; Almutairi, B. S.; Mushtaq, N.; Yousaf, M.; Akbar, N.; Arshad, N.; Irshad, M. S.; Dong, Y., Designing highly active core/shell cathode materials for low-temperature PCFCs. *J. Alloys Compd.* **2023,** *960*, 170861.
[114] Hou, J.; Gong, J.; Luo, J.-L., Constructing highly active surface-nanostructured core/bi-shell $La_{1.2}Sr_{0.8}Ni_{0.5}Mn_{0.5}O_{4+\delta}$ cathode for protonic ceramic fuel cells. *Chem. Eng. J.* **2023,** *459*, 141459.
[115] Lee, W.; Han, J. W.; Chen, Y.; Cai, Z.; Yildiz, B., Cation Size Mismatch and Charge Interactions Drive Dopant Segregation at the Surfaces of Manganite Perovskites. *J. Am. Chem. Soc.* **2013,** *135* (21), 7909-7925.
[116] Koo, B.; Kim, K.; Kim, J. K.; Kwon, H.; Han, J. W.; Jung, W., Sr Segregation in Perovskite Oxides: Why It Happens and How It Exists. *Joule* **2018,** *2* (8), 1476-1499.
[117] Chen, Y.; Téllez, H.; Burriel, M.; Yang, F.; Tsvetkov, N.; Cai, Z.; McComb, D. W.; Kilner, J. A.; Yildiz, B., Segregated Chemistry and Structure on (001) and (100) Surfaces of $(La_{1-x}Sr_x)_2CoO_4$ Override the Crystal Anisotropy in Oxygen Exchange Kinetics. *Chem. Mater.* **2015,** *27* (15), 5436-5450.
[118] Quill, T. J.; LeCroy, G.; Halat, D. M.; Sheelamanthula, R.; Marks, A.; Grundy, L. S.; McCulloch, I.; Reimer, J. A.; Balsara, N. P.; Giovannitti, A.; Salleo, A.; Takacs, C. J., An ordered, self-assembled nanocomposite with efficient electronic and ionic transport. *Nat. Mater.* **2023,** *22* (3), 362-368.
[119] Song, Y.; Song, Y.; Wang, Y.; Tian, Y.; Li, J.; Xu, M.; Shao, Z.; Ciucci, F., Advances in Advanced In Situ Assembled Composite Electrode Materials for Enhanced Solid Oxide Cell Performance. *Adv. Funct. Mater.* **2024,** *34* (46), 2405851.
[120] Kim, J. H.; Jang, K.; Lim, D.-K.; Ahn, S.; Oh, D.; Kim, H.; Seo, J.; Choi, P.-P.; Jung, W., Self-assembled nano-composite perovskites as highly efficient and robust hybrid cathodes for solid oxide fuel cells. *J. Mater. Chem. A* **2022,** *10* (5), 2496-2508.
[121] Song, Y.; Chen, Y.; Wang, W.; Zhou, C.; Zhong, Y.; Yang, G.; Zhou, W.; Liu, M.; Shao, Z., Self-Assembled triple-conducting nanocomposite as a superior protonic ceramic fuel

cell cathode. *Joule* **2019,** *3* (11), 2842-2853.
[122] Zhang, W.; Muroyama, H.; Mikami, Y.; Liu, Q.; Liu, X.; Matsui, T.; Eguchi, K., Effectively enhanced oxygen reduction activity and stability of triple-conducting composite cathodes by strongly interacting interfaces for protonic ceramic fuel cells. *Chem. Eng. J.* **2023,** *461*, 142056.
[123] Tong, H.; Fu, M.; Yang, Y.; Chen, F.; Tao, Z., A Novel Self-Assembled Cobalt-Free Perovskite Composite Cathode with Triple-Conduction for Intermediate Proton-Conducting Solid Oxide Fuel Cells. *Adv. Funct. Mater.* **2022,** *32* (48), 2209695.
[124] Berger, C.; Bucher, E.; Merkle, R.; Nader, C.; Lammer, J.; Grogger, W.; Maier, J.; Sitte, W., Influence of Y-substitution on phase composition and proton uptake of self-generated $Ba(Ce,Fe)O_{3-\delta}$–$Ba(Fe,Ce)O_{3-\delta}$ composites. *J. Mater. Chem. A* **2022,** *10* (5), 2474-2482.
[125] Zou, D.; Yi, Y.; Song, Y.; Guan, D.; Xu, M.; Ran, R.; Wang, W.; Zhou, W.; Shao, Z., The $BaCe_{0.16}Y_{0.04}Fe_{0.8}O_{3-\delta}$ nanocomposite: a new high-performance cobalt-free triple-conducting cathode for protonic ceramic fuel cells operating at reduced temperatures. *J. Mater. Chem. A* **2022,** *10* (10), 5381-5390.
[126] Bello, I. T.; Yu, N.; Song, Y.; Wang, J.; Chan, T.-S.; Zhao, S.; Li, Z.; Dai, Y.; Yu, J.; Ni, M., Electrokinetic Insights into the Triple Ionic and Electronic Conductivity of a Novel Nanocomposite Functional Material for Protonic Ceramic Fuel Cells. *Small* **2022,** *18* (40), 2203207.
[127] Yu, N.; Liu, T.; Chen, X.; Miao, M.; Ni, M.; Wang, Y., Co-generation of liquid chemicals and electricity over Co-Fe alloy/perovskite anode catalyst in a propane fueled solid oxide fuel cell. *Sep. Purif. Technol.* **2022,** *291*, 120890.
[128] Zhang, B.-W.; Zhu, M.-N.; Gao, M.; Chen, J.; Xi, X.; Shen, J.; Feng, R.-F.; Semagina, N.; Duan, N.; Zeng, H.; Luo, J., Phase Transition Engineering of Host Perovskite toward Optimal Exsolution-facilitated Catalysts for Carbon Dioxide Electrolysis. *Angew. Chem., Int. Ed.* **2023,** *62* (29), e202305552.
[129] Yu, N.; Jiang, G.; Liu, T.; Chen, X.; Miao, M.; Zhang, Y.; Wang, Y., Understanding the A-site non-stoichiometry in perovskites: promotion of exsolution of metallic nanoparticles and the hydrogen oxidation reaction in solid oxide fuel cells. *Sustainable Energy Fuels* **2021,** *5* (2), 401-411.
[130] Xu, M.; Jeon, Y.; Naden, A.; Kim, H.; Kerherve, G.; Payne, D. J.; Shul, Y.-g.; Irvine, J. T. S., Synergistic growth of nickel and platinum nanoparticles via exsolution and surface reaction. *Nat. Commun.* **2024,** *15* (1), 4007.
[131] Kim, J. H.; Yoo, S.; Murphy, R.; Chen, Y.; Ding, Y.; Pei, K.; Zhao, B.; Kim, G.; Choi, Y.; Liu, M., Promotion of oxygen reduction reaction on a double perovskite electrode by a water-induced surface modification. *Energy Environ. Sci.* **2021,** *14* (3), 1506-1516.
[132] Zhou, Y.; Liu, E.; Chen, Y.; Liu, Y.; Zhang, L.; Zhang, W.; Luo, Z.; Kane, N.; Zhao, B.; Soule, L.; Niu, Y.; Ding, Y.; Ding, H.; Ding, D.; Liu, M., An active and robust air electrode for reversible protonic ceramic electrochemical cells. *ACS Energy Lett.* **2021,** *6* (4), 1511-1520.
[133] Xu, K.; Zhang, H.; Xu, Y.; He, F.; Zhou, Y.; Pan, Y.; Ma, J.; Zhao, B.; Yuan, W.; Chen, Y.; Liu, M., An efficient steam-induced heterostructured air electrode for protonic ceramic electrochemical cells. *Adv. Funct. Mater.* **2022,** *32* (23), 2110998.
[134] Pei, K.; Zhou, Y.; Xu, K.; Zhang, H.; Ding, Y.; Zhao, B.; Yuan, W.; Sasaki, K.;

Choi, Y.; Chen, Y.; Liu, M., Surface restructuring of a perovskite-type air electrode for reversible protonic ceramic electrochemical cells. *Nat. Commun.* **2022,** *13* (1), 2207.
[135] Vøllestad, E.; Strandbakke, R.; Tarach, M.; Catalán-Martínez, D.; Fontaine, M.-L.; Beeaff, D.; Clark, D. R.; Serra, J. M.; Norby, T., Mixed proton and electron conducting double perovskite anodes for stable and efficient tubular proton ceramic electrolysers. *Nat. Mater.* **2019,** *18* (7), 752-759.
[136] Park, K.; Saqib, M.; Lee, H.; Shin, D.; Jo, M.; Park, K. M.; Hamayun, M.; Kim, S. H.; Kim, S.; Lee, K.-S.; O'Hayre, R.; Choi, M.; Song, S.-J.; Park, J.-Y., Water-mediated exsolution of nanoparticles in alkali metal-doped perovskite structured triple-conducting oxygen electrocatalysts for reversible cells. *Energy Environ. Sci.* **2024,** *17* (3), 1175-1188.
[137] Kim, J. H.; Hong, J.; Lim, D.-K.; Ahn, S.; Kim, J.; Kim, J. K.; Oh, D.; Jeon, S.; Song, S.-J.; Jung, W., Water as a hole-predatory instrument to create metal nanoparticles on triple-conducting oxides. *Energy Environ. Sci.* **2022,** *15* (3), 1097-1105.
[138] Shao, Z.; Haile, S. M., A high-performance cathode for the next generation of solid-oxide fuel cells. *Nature* **2004,** *431* (7005), 170-173.
[139] Duan, C.; Kee, R.; Zhu, H.; Sullivan, N.; Zhu, L.; Bian, L.; Jennings, D.; O'Hayre, R., Highly efficient reversible protonic ceramic electrochemical cells for power generation and fuel production. *Nat. Energy* **2019,** *4* (3), 230-240.
[140] Zhu, F.; He, F.; Liu, D.; Zhang, H.; Xu, Y.; Xu, K.; Chen, Y., A surface reconfiguration of a perovskite air electrode enables an active and durable reversible protonic ceramic electrochemical cell. *Energy Storage Mater.* **2022,** *53*, 754-762.
[141] Hu, D.; Kim, J.; Niu, H.; Daniels, L. M.; Manning, T. D.; Chen, R.; Liu, B.; Feetham, R.; Claridge, J. B.; Rosseinsky, M. J., High-performance protonic ceramic fuel cell cathode using protophilic mixed ion and electron conducting material. *J. Mater. Chem. A* **2022,** *10* (5), 2559-2566.
[142] Xu, X.; Wang, H.; Fronzi, M.; Wang, X.; Bi, L.; Traversa, E., Tailoring cations in a perovskite cathode for proton-conducting solid oxide fuel cells with high performance. *J. Mater. Chem. A* **2019,** *7* (36), 20624-20632.
[143] Liu, Z.; Cheng, D.; Zhu, Y.; Liang, M.; Yang, M.; Yang, G.; Ran, R.; Wang, W.; Zhou, W.; Shao, Z., Robust bifunctional phosphorus-doped perovskite oxygen electrode for reversible proton ceramic electrochemical cells. *Chem. Eng. J.* **2022,** *450*, 137787.
[144] Ren, R.; Wang, Z.; Meng, X.; Wang, X.; Xu, C.; Qiao, J.; Sun, W.; Sun, K., Tailoring the oxygen vacancy to achieve fast intrinsic proton transport in a perovskite cathode for protonic ceramic fuel cells. *ACS Appl. Energy Mater.* **2020,** *3* (5), 4914-4922.
[145] Wang, N.; Toriumi, H.; Sato, Y.; Tang, C.; Nakamura, T.; Amezawa, K.; Kitano, S.; Habazaki, H.; Aoki, Y., $La_{0.8}Sr_{0.2}Co_{1-x}Ni_xO_{3-\delta}$ as the efficient triple conductor air electrode for protonic ceramic cells. *ACS Appl. Energy Mater.* **2021,** *4* (1), 554-563.
[146] Li, Y.; Li, Y.; Wan, Y.; Xie, Y.; Zhu, J.; Pan, H.; Zheng, X.; Xia, C., Perovskite oxyfluoride electrode enabling direct electrolyzing carbon dioxide with excellent electrochemical performances. *Adv. Energy Mater.* **2019,** *9* (3), 1803156.
[147] Xiong, J.; Zhong, H.; Li, J.; Zhang, X.; Shi, J.; Cai, W.; Qu, K.; Zhu, C.; Yang, Z.; Beckman, S. P.; Cheng, H., Engineering highly active oxygen sites in perovskite oxides for stable and efficient oxygen evolution. *Appl. Catal., B* **2019,** *256*, 117817.
[148] Gao, J.; Liu, Y.; Gao, Y.; Yuan, M.; Wang, Z.; Lü, Z.; Li, Q.; Wei, B., Cobalt-free

fluorine doped $Bi_{0.7}Sr_{0.3}FeO_{3-\delta}$ oxides for energetic cathodes of low-temperature solid oxide fuel cells. *Chem. Eng. J.* **2023,** *452*, 139584.
[149] Bello, I. T.; Yu, N.; Zhai, S.; Song, Y.; Zhao, S.; Cheng, C.; Zhang, Z.; Ni, M., Effect of engineered lattice contraction and expansion on the performance and CO_2 tolerance of $Ba_{0.5}Sr_{0.5}Co_{0.7}Fe_{0.3}O_{3-\delta}$ functional material for intermediate temperature solid oxide fuel cells. *Ceram. Int.* **2022,** *48* (15), 21416-21427.
[150] Xue, J.; Li, J.; Zhuang, L.; Chen, L.; Feldhoff, A.; Wang, H., Anion doping CO_2-stable oxygen permeable membranes for syngas production. *Chem. Eng. J.* **2018,** *347*, 84-90.
[151] Zhang, Y.; Zhu, Z.; Gu, Y.; Chen, H.; Zheng, Y.; Ge, L., Effect of Cl doping on the electrochemical performance of $Sr_2Fe_{1.5}Mo_{0.5}O_{6-\delta}$ cathode material for solid oxide fuel cells. *Ceram. Int.* **2020,** *46* (14), 22787-22796.
[152] Zhang, Z.; Zhu, Y.; Zhong, Y.; Zhou, W.; Shao, Z., Anion doping: a new strategy for developing high-performance perovskite-type cathode materials of solid oxide fuel cells. *Adv. Energy Mater.* **2017,** *7* (17), 1700242.
[153] Anitha Sukkurji, P.; Molinari, A.; Reitz, C.; Witte, R.; Kübel, C.; Chakravadhanula, V. S. K.; Kruk, R.; Clemens, O., Anion doping of ferromagnetic thin films of $La_{0.74}Sr_{0.26}MnO_{3-\delta}$ via topochemical fluorination. *Materials* **2018,** *11* (7), 1204.
[154] Xie, Y.; Shi, N.; Huan, D.; Tan, W.; Zhu, J.; Zheng, X.; Pan, H.; Peng, R.; Xia, C., A stable and efficient cathode for fluorine-containing proton-conducting solid oxide fuel cells. *ChemSusChem* **2018,** *11* (19), 3423-3430.
[155] Zhu, J.; Liu, G.; Liu, Z.; Chu, Z.; Jin, W.; Xu, N., Unprecedented perovskite oxyfluoride membranes with high-efficiency oxygen ion transport paths for low-temperature oxygen permeation. *Adv. Mater.* **2016,** *28* (18), 3511-3515.
[156] Wan, Y.; Xing, Y.; Li, Y.; Huan, D.; Xia, C., Thermal cycling durability improved by doping fluorine to $PrBaCo_2O_{5+\delta}$ as oxygen reduction reaction electrocatalyst in intermediate-temperature solid oxide fuel cells. *J. Power Sources* **2018,** *402*, 363-372.
[157] Ma, Z.; Ye, Q.; Zhang, B.; Yang, W.; Dong, F.; Ni, M.; Lin, Z., A highly efficient and robust bifunctional perovskite-type air electrode with triple-conducting behavior for low-temperature solid oxide fuel cells. *Adv. Funct. Mater.* **2022,** *32* (47), 2209054.
[158] Zhang, L.; Sun, W.; Xu, C.; Ren, R.; Yang, X.; Qiao, J.; Wang, Z.; Sun, K., Attenuating a metal–oxygen bond of a double perovskite oxide via anion doping to enhance its catalytic activity for the oxygen reduction reaction. *J. Mater. Chem. A* **2020,** *8* (28), 14091-14098.
[159] Wang, W.; Zhang, X.; Zhang, D.; Zeng, Q.; Jiang, Y.; Lin, B., Highly promoted performance of triple-conducting cathode for YSZ-based SOFC via fluorine anion doping. *Ceram. Int.* **2020,** *46* (15), 23964-23971.
[160] Chen, Y.; Hong, T.; Wang, P.; Brinkman, K.; Tong, J.; Cheng, J., Investigate the proton uptake process of proton/oxygen ion/hole triple conductor $BaCo_{0.4}Fe_{0.4}Zr_{0.1}Y_{0.1}O_{3-\delta}$ by electrical conductivity relaxation. *J. Power Sources* **2019,** *440*, 227122.
[161] Poetzsch, D.; Merkle, R.; Maier, J., Stoichiometry variation in materials with three mobile carriers—thermodynamics and transport kinetics exemplified for protons, oxygen vacancies, and holes. *Adv. Funct. Mater.* **2015,** *25* (10), 1542-1557.
[162] Ren, R.; Yu, X.; Wang, Z.; Xu, C.; Song, T.; Sun, W.; Qiao, J.; Sun, K., Fluorination inductive effect enables rapid bulk proton diffusion in $BaCo_{0.4}Fe_{0.4}Zr_{0.1}Y_{0.1}O_{3-\delta}$ perovskite

oxide for high-activity protonic ceramic fuel cell cathode. *Appl. Catal., B* **2022,** *317*, 121759.
[163] Belova, K.; Baskakova, S.; Argirusis, C.; Animitsa, I., The effect of F^--doping on the conductivity of proton conductor $Ba_4Ca_2Nb_2O_{11}$. *Electrochim. Acta* **2016,** *193*, 63-71.
[164] Wang, N.; Tang, C.; Du, L.; Zhu, R.; Xing, L.; Song, Z.; Yuan, B.; Zhao, L.; Aoki, Y.; Ye, S., Advanced cathode materials for protonic ceramic fuel cells: recent progress and future perspectives. *Adv. Energy Mater.* **2022,** *12* (34), 2201882.
[165] Hu, T.; Zhu, F.; Xia, J.; He, F.; Du, Z.; Zhou, Y.; Liu, Y.; Wang, H.; Chen, Y., In situ engineering of a cobalt-free perovskite air electrode enabling efficient reversible oxygen reduction/evolution reactions. *Adv. Funct. Mater.* **2023,** *33* (43), 2305567.
[166] Zhang, Y.; Chen, B.; Guan, D.; Xu, M.; Ran, R.; Ni, M.; Zhou, W.; O'Hayre, R.; Shao, Z., Thermal-expansion offset for high-performance fuel cell cathodes. *Nature* **2021,** *591* (7849), 246-251.
[167] Song, Y.; Liu, J.; Wang, Y.; Guan, D.; Seong, A.; Liang, M.; Robson, M. J.; Xiong, X.; Zhang, Z.; Kim, G.; Shao, Z.; Ciucci, F., Nanocomposites: a new opportunity for developing highly active and durable bifunctional air electrodes for reversible protonic ceramic cells. *Adv. Energy Mater.* **2021,** *11* (36), 2101899.
[168] Zhou, C.; Liu, D.; Fei, M.; Wang, X.; Ran, R.; Xu, M.; Wang, W.; Zhou, W.; O'Hayre, R.; Shao, Z., Cathode water management towards improved performance of protonic ceramic fuel cells. *J. Power Sources* **2023,** *556*, 232403.
[169] Wang, X.; Li, W.; Zhou, C.; Xu, M.; Hu, Z.; Pao, C.-W.; Zhou, W.; Shao, Z., Enhanced proton conduction with low oxygen vacancy concentration and favorable hydration for protonic ceramic fuel cells cathode. *ACS Appl. Mater. Interfaces* **2023,** *15* (1), 1339-1347.
[170] Qiu, P.; Liu, B.; Wu, L.; Qi, H.; Tu, B.; Li, J.; Jia, L., K-doped $BaCo_{0.4}Fe_{0.4}Zr_{0.2}O_{3-\delta}$ as a promising cathode material for protonic ceramic fuel cells. *J. Adv. Ceram.* **2022,** *11* (12), 1988-2000.
[171] Zhang, Y.; Hao, X.; Liu, J.; Yang, X.; Xu, H.; Wang, Z.; Luo, Y.; Wang, F.; He, T., Effectively boosting hydration capacity and oxygen reduction activity of cobalt-free perovskite cathode by K^+ doping strategy for protonic ceramic fuel cells. *Ceram. Int.* **2024,** *50* (3, Part A), 4746-4755.
[172] Cho, I.; Yun, J.; Seong, B.; Kim, J.; Choi, S. H.; Ji, H.-I.; Choi, S., Correlation between hydration properties and electrochemical performances on Ln cation size effect in layered perovskite for protonic ceramic fuel cells. *J. Energy Chem.* **2024,** *88*, 1-9.
[173] Kim, J. H.; Kim, D.; Ahn, S.; Kim, K. J.; Jeon, S.; Lim, D.-K.; Kim, J. K.; Kim, U.; Im, H.-N.; Koo, B.; Lee, K. T.; Jung, W., An universal oxygen electrode for reversible solid oxide electrochemical cells at reduced temperatures. *Energy Environ. Sci.* **2023,** *16* (9), 3803-3814.
[174] Xu, Y.; Xu, K.; Zhu, F.; He, F.; Zhang, H.; Fang, C.; Liu, Y.; Zhou, Y.; Choi, Y.; Chen, Y., A low-lewis-acid-strength cation Cs^+-doped double perovskite for fast and durable oxygen reduction/evolutions on protonic ceramic cells. *ACS Energy Lett.* **2023,** *8* (10), 4145-4155.
[175] Wang, Z.; Wang, Y.; Wang, J.; Song, Y.; Robson, M. J.; Seong, A.; Yang, M.; Zhang, Z.; Belotti, A.; Liu, J.; Kim, G.; Lim, J.; Shao, Z.; Ciucci, F., Rational design of perovskite ferrites as high-performance proton-conducting fuel cell cathodes. *Nat. Catal.* **2022,** *5* (9), 777-787.

[176] Hu, T.; He, F.; Liu, M.; Chen, Y., In situ/operando regulation of the reaction activities on hetero-structured electrodes for solid oxide cells. *Prog. Mater Sci.* **2023,** *133*, 101050.
[177] Zhou, C.; Wang, X.; Liu, D.; Fei, M.; Dai, J.; Guan, D.; Hu, Z.; Zhang, L.; Wang, Y.; Wang, W.; O'Hayre, R.; Jiang, S. P.; Zhou, W.; Liu, M.; Shao, Z., New strategy for boosting cathodic performance of protonic ceramic fuel cells through incorporating a superior hydronation second phase. *Energy Environ. Mater.* **2023,** *0*, e12660.
[178] Liang, M.; Wang, Y.; Song, Y.; Guan, D.; Wu, J.; Chen, P.; Maradesa, A.; Xu, M.; Yang, G.; Zhou, W.; Wang, W.; Ran, R.; Ciucci, F.; Shao, Z., High-temperature water oxidation activity of a perovskite-based nanocomposite towards application as air electrode in reversible protonic ceramic cells. *Appl. Catal., B* **2023,** *331*, 122682.
[179] Liang, M.; Zhu, Y.; Song, Y.; Guan, D.; Luo, Z.; Yang, G.; Jiang, S. P.; Zhou, W.; Ran, R.; Shao, Z., A new durable surface nanoparticles-modified perovskite cathode for protonic ceramic fuel cells from selective cation exsolution under oxidizing atmosphere. *Adv. Mater.* **2022,** *34* (10), 2106379.
[180] Joo, S.; Seong, A.; Kwon, O.; Kim, K.; Lee, J. H.; Gorte, R. J.; Vohs, J. M.; Han, J. W.; Kim, G. J. S. a., Highly active dry methane reforming catalysts with boosted in situ grown Ni-Fe nanoparticles on perovskite via atomic layer deposition. *Sci. Adv.* **2020,** *6* (35), eabb1573.
[181] Joo, S.; Kwon, O.; Kim, K.; Kim, S.; Kim, H.; Shin, J.; Jeong, H. Y.; Sengodan, S.; Han, J. W.; Kim, G., Cation-swapped homogeneous nanoparticles in perovskite oxides for high power density. *Nat. Commun.* **2019,** *10* (1), 697.
[182] Ding, X.; Gao, Z.; Ding, D.; Zhao, X.; Hou, H.; Zhang, S.; Yuan, G., Cation deficiency enabled fast oxygen reduction reaction for a novel SOFC cathode with promoted CO_2 tolerance. *Appl. Catal., B* **2019,** *243*, 546-555.
[183] Shin, Y.; Doh, K.-Y.; Kim, S. H.; Lee, J. H.; Bae, H.; Song, S.-J.; Lee, D., Effect of oxygen vacancies on electrical conductivity of $La_{0.5}Sr_{0.5}FeO_{3-\delta}$ from first-principles calculations. *J. Mater. Chem. A* **2020,** *8* (9), 4784-4789.
[184] Chen, X.; Yu, N.; Bello, I. T.; Guan, D.; Li, Z.; Liu, T.; Liu, T.; Shao, Z.; Ni, M., Facile anion engineering: A pathway to realizing enhanced triple conductivity in oxygen electrodes for reversible protonic ceramic electrochemical cells. *Energy Storage Mater.* **2023,** *63*, 103056.
[185] Muñoz-García, A. B.; Ritzmann, A. M.; Pavone, M.; Keith, J. A.; Carter, E. A., Oxygen transport in perovskite-type solid oxide fuel cell materials: insights from quantum mechanics. *Acc. Chem. Res.* **2014,** *47* (11), 3340-3348.
[186] Hou, J.; Qian, J.; Bi, L.; Gong, Z.; Peng, R.; Liu, W., The effect of oxygen transfer mechanism on the cathode performance based on proton-conducting solid oxide fuel cells. *J. Mater. Chem. A* **2015,** *3* (5), 2207-2215.
[187] Jing, J.; Lei, Z.; Xue, Y.; Zheng, Z.; Wang, H.; Zhang, P.; Ge, B.; Yang, Z., Constructing highly active and durable oxygen electrode by nanoengineering for reversible protonic ceramic cell. *Energy Storage Mater.* **2024,** *72*, 103694.
[188] Gao, Y.; Liu, K.; Zhang, X.; Li, Q.; Chang, Y.; Fu, M.; Tao, Z., Cs-Doped BCCF perovskite with enhanced surface proton acid sites for high-performance R-PCECs. *Chem. Eng. J.* **2025,** *504*, 158984.
[189] Xie, Y.; Shi, N.; Ricote, S.; Chen, M., Zinc triggers favorable hydrogenation reaction

in double perovskite $PrBaCo_2O_{6-\delta}$: Applications in protonic ceramic cells. *Chem. Eng. J.* **2024,** *492*, 151939.
[190] Miranda, J. L.; Ribeiro, C.; Tkach, A.; Senos, A. M. O. R.; Vilarinho, P. M., Ultrafast high-temperature sintering of potassium-sodium niobate: Processing and properties. *J. Eur. Ceram. Soc.* **2024,** *44* (15), 116701.
[191] Deng, W.; Xu, Y.; Zhang, X.; Xu, K.; Liao, Y.; Yang, X.; Chen, Y., A perovskite-type air electrode with in situ formed $BaCoO_{3-\delta}$ nanoparticles for reversible protonic ceramic electrochemical cells. *Chem. Eng. J.* **2025**, 162037.
[192] Hu, A.; Yang, C.; Li, Y.; Xia, K.; Tian, Y.; Pu, J.; Chi, B., High-Entropy Driven Self-Assembled Dual-phase Composite Air Electrodes with Enhanced Performance and Stability for Reversible Protonic Ceramic Cells. *Adv. Energy Mater.* **2025**, 2405466.
[193] Du, Z.; Xu, K.; Zhu, F.; Xu, Y.; He, F.; Gao, H.; Gong, W.; Choi, Y.; Chen, Y., Indium-Doping-Induced Nanocomposites with Improved Oxygen Reaction Activity and Durability for Reversible Protonic Ceramic Electrochemical Cell Air Electrodes. *Adv. Funct. Mater.* **2024,** *34* (49), 2409188.
[194] He, F.; Hou, M.; Liu, D.; Ding, Y.; Sasaki, K.; Choi, Y.; Guo, S.; Han, D.; Liu, Y.; Liu, M.; Chen, Y., Phase segregation of a composite air electrode unlocks the high performance of reversible protonic ceramic electrochemical cells. *Energy Environ. Sci.* **2024,** *17* (11), 3898-3907.
[195] Shi, N.; Xie, Y.; Tadé, M. O.; Shao, Z., Evolution and Reconstruction of Air-Electrode Surface Composition in Reversible Protonic Ceramic Cells: Mechanisms, Impacts on Catalytic Performance, and Optimization Strategies – A Review. *Adv. Mater.* **2025,** *37* (11), 2416528.
[196] Huang, Y.; He, F.; Xu, K.; Gao, H.; Zhang, X.; Xu, Y.; Du, Z.; Zhu, F.; Gong, W.; Jian, C.; Chen, Y., Efficient and Stable In Situ Self-Assembled Air Electrodes for Reversible Protonic Ceramic Electrochemical Cells. *Adv. Funct. Mater.* **2024,** *34* (49), 2409598.
[197] Liu, Z.; Bai, Y.; Sun, H.; Guan, D.; Li, W.; Huang, W.-H.; Pao, C.-W.; Hu, Z.; Yang, G.; Zhu, Y.; Ran, R.; Zhou, W.; Shao, Z., Synergistic dual-phase air electrode enables high and durable performance of reversible proton ceramic electrochemical cells. *Nat. Commun.* **2024,** *15* (1), 472.
[198] Lei, S.; Ma, J.; Li, W.; Hanif, M. B.; Li, C.-X.; Wang, D.; Wang, S., A self-assembled composite cathode with enhanced activity and stability for protonic ceramic fuel cells. *J. Power Sources* **2025,** *631*, 236257.
[199] Li, Y.; Yang, C.; Liu, X.; Yang, C.; Xia, K.; Tian, Y.; He, S.; Chi, B., Structurally Stable Perovskite Cathode with Extended Lifetime for Protonic Ceramic Fuel Cells. *ACS Sustainable Chem. Eng.* **2025,** *13* (12), 4740-4749.
[200] Zhang, X.; Xu, Y.; Xu, K.; Chen, L.; Zhu, F.; He, F.; Du, Z.; Yuan, W.; Chen, Y., An Active and Durable Misfit-Layered Air Electrode for Reversible Protonic Ceramic Electrochemical Cells. *ACS Energy Lett.* **2025**, 1874-1883.
[201] Li, M.; Liu, F.; Ding, D., Critical insights into the steam electrolysis electrode in protonic ceramic cells for hydrogen production. *Nat. Catal.* **2025**.
[202] Li, M.; Liu, F.; Ding, D., Critical insights into the steam electrolysis electrode in protonic ceramic cells for hydrogen production. *Nat. Catal.* **2025,** *8* (4), 293-300.
[203] Wei, B.; Schroeder, M.; Martin, M., Surface Cation Segregation and Chromium Deposition on the Double-Perovskite Oxide $PrBaCo_2O_{5+\delta}$. *ACS Appl. Mater. Interfaces* **2018,**

10 (10), 8621-8629.
[204] Choi, M.; Kim, D.; Lee, T. K.; Lee, J.; Yoo, H. S.; Lee, W., Interface Engineering to Operate Reversible Protonic Ceramic Electrochemical Cells Below 500 °C. *Adv. Energy Mater.* **2025,** *15* (2), 2400124.
[205] Zhang, X.; Tang, C.; Yang, Y.; Zheng, F.; Su, Q.; Xiang, H.; Meng, L.; Du, L.; Aoki, Y.; Luo, D.; Wang, N.; Ye, S., Novel High-Entropy Air Electrodes Enhancing Electrochemical Performances of Reversible Protonic Ceramic Cells. *Adv. Funct. Mater.* **2025,** *35* (20), 2421083.
[206] Guo, S.; Wang, L.; Xue, C.; Lin, S.; Yi, T.; Zhu, Y.; Han, D., High-performance Co-free dual-phase perovskite positrodes for protonic ceramic cells: Zn and Ni-doped $BaCe_{0.2}Fe_{0.8}O_{3-\delta}$ system. *J. Power Sources* **2024,** *623*, 235419.
[207] Seong, B.; Yun, J.; Choi, S., High-performance and excellent thermal cycling stability of reversible protonic ceramic cells enabled by a promising Sr/Co-free $PrNi_{0.5}Fe_{0.5}O_{3-\delta}$ air electrode. *J. Mater. Chem. A* **2024,** *12* (46), 32084-32094.
[208] Zhang, S.; Yang, C.; Jiang, Y.; Li, P.; Xia, C., A robust fluorine-containing ceramic cathode for direct CO_2 electrolysis in solid oxide electrolysis cells. *J. Energy Chem.* **2023,** *77*, 300-309.
[209] Yao, C.; Xia, B.; Zhang, H.; Wang, H.; Zhang, W.; Guo, Q.; Jiang, Y.; Lang, X.; Cai, K., Fluoride-driven modulation of oxygen vacancies and surface stability in cobalt-based perovskite as a high-performance cathode for solid oxide fuel cells. *Chem. Eng. J.* **2025,** *505*, 159359.
[210] Gao, Y.; Fu, M.; Zhao, S.; Hou, Z.; Liu, K.; Deng, X.; Tao, Z., Self-Assembled Composite Cathodes with TEC Gradient for Proton-Conducting Solid Oxide Fuel Cells. *Adv. Funct. Mater.* **2025,** *35* (10), 2416625.
[211] Zhou, Q.; Wang, F.; Shen, Y.; He, T., Performances of $LnBaCo_2O_{5+x}$–$Ce_{0.8}Sm_{0.2}O_{1.9}$ composite cathodes for intermediate-temperature solid oxide fuel cells. *J. Power Sources* **2010,** *195* (8), 2174-2181.
[212] Zhu, W.; Wang, H.; Xu, L.; Yuan, J.; Gong, J.; Liu, X., $Pr_{0.7}Ba_{0.3}Co_{0.8-x}Fe_{0.2}Ni_xO_{3-\delta}$ perovskite: High activity and durable cathode for intermediate-to-low-temperature proton-conducting solid oxide fuel cells. *Int. J. Hydrogen Energy* **2023,** *48* (86), 33633-33643.
[213] Yin, Y.; Xiao, D.; Wu, S.; Da'as, E. H.; Gu, Y.; Bi, L., A real proton-conductive, robust, and cobalt-free cathode for proton-conducting solid oxide fuel cells with exceptional performance. *SusMat* **2023,** *3* (5), 697-708.
[214] Zhu, Z.; Zhou, M.; Tan, K.; Fan, Z.; Cao, D.; Liu, Z.; Chen, M.; Chen, Y.; Chen, M.; Liu, J., High Performance and Stability Enabled by Tuning the Component Thermal Expansion Coefficients of a Proton-Conducting Solid Oxide Cell Operating at High Steam Concentration. *ACS Appl. Mater. Interfaces* **2023,** *15* (11), 14457-14469.
[215] Wang, K.; Cui, Y.; Ni, J.; Ni, C., Cu doping enhanced the performance of $BaFe_{0.8}Zr_{0.1}Y_{0.1}O_{3-\delta}$ cathode for a proton-conducting solid oxide fuel cell at low temperature. *Int. J. Hydrogen Energy* **2024,** *57*, 1316-1324.
[216] Yin, Y.; Yu, S.; Dai, H.; Bi, L., Triggering interfacial activity of the traditional $La_{0.5}Sr_{0.5}MnO_3$ cathode with Co-doping for proton-conducting solid oxide fuel cells. *J. Mater. Chem. A* **2022,** *10* (4), 1726-1734.
[217] Wei, Z.; Wang, J.; Yu, X.; Li, Z.; Zhao, Y.; Chai, J., Study on Ce and Y co-doped

$BaFeO_{3-\delta}$ cubic perovskite as free-cobalt cathode for proton-conducting solid oxide fuel cells. *Int. J. Hydrogen Energy* **2021,** *46* (46), 23868-23878.
[218] Wang, D.; Xia, Y.; Lv, H.; Miao, L.; Bi, L.; Liu, W., $PrBaCo_{2-x}Ta_xO_{5+\delta}$ based composite materials as cathodes for proton-conducting solid oxide fuel cells with high CO_2 resistance. *Int. J. Hydrogen Energy* **2020,** *45* (55), 31017-31026.
[219] Xia, Y.; Xu, X.; Teng, Y.; Lv, H.; Jin, Z.; Wang, D.; Peng, R.; Liu, W., A novel $BaFe_{0.8}Zn_{0.1}Bi_{0.1}O_{3-\delta}$ cathode for proton conducting solid oxide fuel cells. *Ceram. Int.* **2020,** *46* (16, Part A), 25453-25459.
[220] Liu, B.; Li, Z.; Yang, X.; Yan, D.; Li, J.; Jia, L., Novel mixed $H^+/e^-/O^{2-}$ conducting cathode material $PrBa_{0.9}K_{0.1}Fe_{1.9}Zn_{0.1}O_{5+\delta}$ for proton-conducting solid oxide fuel cells. *J. Mater. Chem. A* **2022,** *10* (34), 17425-17433.
[221] Li, Y.; Li, Y.; Jiang, S.; Chen, Y.; Xu, J.; Qiu, H.; Su, C.; Ge, L., La-doped $Sr_4Fe_4Co_2O_{13-\delta}$ as a promising in-situ self-assembled composite cathode for protonic ceramic fuel cells. *Composites, Part B* **2024,** *280*, 111517.
[222] Ding, Y.; chen, Y.; Lu, X.; Lin, B., Preparation and characterization of $Ba_{0.5}Sr_{0.5}Fe_{0.9}Ni_{0.1}O_{3-\delta}$–$Sm_{0.2}Ce_{0.8}O_{1.9}$ compose cathode for proton-conducting solid oxide fuel cells. *Int. J. Hydrogen Energy* **2012,** *37* (12), 9830-9835.
[223] Lv, X.; Chen, H.; Zhou, W.; Li, S.-D.; Cheng, F.; Shao, Z., $SrCo_{0.4}Fe_{0.4}Zr_{0.1}Y_{0.1}O_{3-\delta}$, A new CO_2 tolerant cathode for proton-conducting solid oxide fuel cells. *Renewable Energy* **2022,** *185*, 8-16.
[224] Wu, Y.; Hou, J.; Gong, Z.; Miao, L.; Tang, H.; Liu, W., High performance $BaCe_{0.5}Fe_{0.5-x}Bi_xO_{3-\delta}$ as cobalt-free cathode for proton-conducting solid oxide fuel cells. *J. Alloys Compd.* **2019,** *790*, 551-557.